IDŐJÁRÁS

QUARTERLY JOURNAL
OF THE HUNGARIAN METEOROLOGICAL SERVICE

CONTENTS

****

http://www.met.hu/Journal-Idojaras.php

VOL. 118 * NO. 3 * JULY – SEPTEMBER 2014

IDŐJÁRÁS

Quarterly Journal of the Hungarian Meteorological Service

Editorial Office: Kitaibel P.u. 1, H-1024 Budapest, Hungary
P.O. Box 38, H-1525 Budapest, Hungary
E-mail: journal.idojaras@met.hu
Fax: (36-1) 346-4669

Indexed and abstracted in Science Citation Index Expanded™ and Journal Citation Reports/Science Edition
Covered in the abstract and citation database SCOPUS®

Subscription by mail:
IDŐJÁRÁS, P.O. Box 38, H-1525 Budapest, Hungary
E-mail: journal.idojaras@met.hu

IDŐJÁRÁS

Quarterly Journal of the Hungarian Meteorological Service
Vol. 118, No. 3, July – September, 2014, pp. 193–206

The effects of climate change on grape production in Hungary

Ildikó Mesterházy*, **Róbert Mészáros**, and **Rita Pongrácz**

Department of Meteorology, Eötvös Loránd University,
Pázmány P. sétány 1/A, H-1117 Budapest, Hungary

**Corresponding author; E-mail: mesildiko@caesar.elte.hu*

(Manuscript received in final form November 3, 2013)

Abstract—Spatial distribution of several indices characterizing wine production in Hungary are analyzed in this paper using the bias-corrected outputs of three different regional climate models: RegCM, ALADIN, and PRECIS. For this purpose, the daily minimum, maximum, and mean temperature, and daily precipitation time series were used. The indices include the active degree days, Huglin's heliothermal index, length of vegetation period according to thermal conditions, hydrothermal coefficient, and frequencies of extreme temperature events. In the study, first, the past changes of these indices are evaluated, and then, the main focus is on the projected changes until the end of the 21st century. Our results suggest that white wine grapes are very likely to lose their dominance over red wine grapes in Hungary in the next few decades. Furthermore, the ripening of late-ripening and very-late-ripening grape varieties will become more likely. Extreme high summer temperatures will become more frequent, while the risk of frost damage in the reproductive cycle is projected to decrease.

Key-words: Vitis vinifera, RegCM, ALADIN, PRECIS, regional climate change, Hungarian wine regions

1. Introduction

Wine grape production is a segment of major importance in Hungarian agriculture. The life cycle of the grape is influenced by climatic, edaphic, and biotic factors, from which climatic factors are the most dominant and dynamically changing ones (*Kozma*, 2002). As vineyards in Hungary produce grapes for 25–30 years, predicting these climatic factors for the next decades has a great importance.

In this work, we analyze the temporal trends of selected climatic factors, and use several indices to identify grape varieties in Hungary that are more

suitable for the projected climatic changes. Additionally, we predict the trend of change in the probability of desease development for the next decades. Although there has been a recent work studying the future changes of ecological factors affecting Hungarian grape fields (*Szenteleki*, 2012), our work is the first climatic study of the entire Hungarian region focusing specifically on grape and wine production.

2. Studied regions and applied methods

2.1. Studied regions

The wine subregions of Hungary belong to the northern territorries of grape production. Grape production is made possible primarily by the diverse microregions of the country and their specific meso- and microclimate. Based on microclimatic similarities, the 22 Hungarian wine subregions are categorized to 7 regions (127/2009. (IX. 29.) FVM regulation, appendix 1), covering Danube (Duna), Balaton, Eger, North-Transdanubia (Észak-Dunántúl), Pannon, Sopron, and Tokaj. On these wine regions, the wine grape production is dominated by white wine grapes, however, in some regions (e.g., in Sopron region), red grape production is also important. From the grape varieties, both early-, medium-, and late-ripening ones are produced in the different regions (*Hajdú*, 2003).

2.2. Applied regional climate models

Results provided by global climate models (GCMs) cannot be applied to small regions like the Carpathian Basin and Hungary. Therefore, in our analysis we applied regional climate models (RCMs) nested in GCMs. The RCMs have finer spatial resolution than GCMs, thus they can take into account local scale landscape features and topography.

We used the outputs of the following model simulations carried out in the framework of the European ENSEMBLES project (*van der Linden* and *Mitchell*, 2009): the RegCM (*Giorgi et al.*, 1993), the ALADIN (*Déqué et al.*, 1998) regional climate models, and the PRECIS regional climate model developed by the UK Met Office Hadley Centre for Climate Prediction and Research (*Wilson et al.*, 2007) applied specifically to the Carpathian Basin (*Pieczka*, 2012). The raw RCM outputs generally overestimate the temperature in summer and the precipitation throughout the entire year (*Pongrácz et al.*, 2011; *Pieczka et al.*, 2011). Therefore, they were corrected using a percentile-based bias correction technique (*Formayer* and *Haas*, 2009) consisting of correcting the simulated daily outputs on the basis of the monthly distributions of observed meteorological data. Observations are available from the gridded E-OBS database (*Haylock et al.*, 2008). The RCM simulations use the A1B emission scenario (*Nakicenovic* and *Swart*, 2000) for the 21st century. This scenario

assumes a slowly growing trend of atmospheric carbon-dioxide concentration, which is likely to exceed 700 ppm by the end of the century.

All RCMs applied a horizontal resolution of 25 kilometers. This resolution is still too coarse for detailed studies on the changing microclimatic conditions of vineyards, but it enables us to estimate some general tendencies. The simulated model datasets used in this study cover the geographic region between latitudes 44°–50° N and longitudes 14°–26° E, and contain the time interval 1951–2100 (except for the PRECIS simulation, where the time interval was 1951–2098). The applied RCM outputs include the daily minimum, maximum, and mean temperature, as well as the daily precipitation, which are used to calculate past and future time series of various indices described in Section 2.3, and derive conclusion on their effect on wine grape production in Hungary in the *middle of the 21st century* (for the period 2021–2050) and in the *end of the 21st century* (for the period 2071–2100; or between 2069–2098 for the PRECIS model due to shorter simulation time range). The years 1961–1990 is defined as the *reference period.*

2.3. The applied indices

The indices that we analyze in this paper are the following.

Active degree days (ADD). This can be easily calculated from the daily mean temperatures and can be used to determine the grape varieties that the given region is suitable for (see *Table 1*). The calculation is carried out by summing the residual above 10 °C of the daily mean temperatures throughout the growing season (*Davitaja*, 1959; *Kozma*, 2002). Note, that in all our calculations we defined the growing season as the period of a year when the daily mean temperature is above 10 °C for at least three consecutive days (*Kozma*, 2002). This practically corresponds to the time beginning with budburst and ending with leaf-fall, and thus, covers a longer interval of the year than the one discussed in *Table 1*.

Table 1. Grouping of grape varieties based on the active degree days (*Davitaja*, 1959; *Kozma*, 2002)

Ripening categories	**Active degree days**	**Number of days**
	(from budburst to full ripening of berries)	
very-early-ripening varieties	690–850 °C	110–120 days
early-ripening varieties	850–1150 °C	120–130 days
medium-ripening varieties	1150–1350 °C	130–145 days
late- & very-late-ripening varieties	>1350 °C	>145 days

Huglin's heliothermal index (HI) (*Huglin,* 1978). This gives a measure on the suitability of a region for different grape varieties based on the daily mean and maximum temperatures of the region, and on a factor denoted as d, which depends on the geographic latitude of the region (and thus the average length of the days during the growing season). Huglin's heliothermal index can be written as:

$$HI = d\sum \frac{[(T - 10°\mathrm{C}) + (T_x - 10°\mathrm{C})]}{2}, \quad (1)$$

where d is the latitude coefficient increasing monotonically from d_{40}=1.02 at latitude 40° N to d_{50}=1.06 at latitude 50° N; T is the daily mean temperature, and T_x is the daily maximum temperature, both given in °C. In Eq. (1), each term of the sum corresponds to one day in the growing season, and thus, the sum goes through all the days of the growing season. The optimal values of *HI* for selected grape varieties are shown in *Table 2.*

Table 2. The optimal values for Huglin's heliothermal index (HI) for selected white (normal fonts) and red (italic fonts) wine grape varieties. (*Huglin*, 1978; *Kozma*, 2002)

Huglin's Heliotermal Index (HI; in °C)	Grape varieties
2300	*Aramon*
2200	*Carignan, Zinfandel*
2100	*Cinsaut, Grenache, Syrah, Sangiovese*
2000	Ugni blanc
1900	Chenin blanc, Welschriesling, *Merlot, Cabernet Sauvignon*
1800	*Cabernet franc, Blaufränkisch*
1700	Chardonnay, Rhine Riesling, Silvaner, Sauvignon blanc, *Pinot noir*
1600	Pinot blanc, Gewürztraminer, *Gamay*
1500	Müller-Thurgau
1400	Irsai Olivér

Occurrences of extreme temperature episodes. Thermal susceptibility of wine grapes depends on many biotic and climatic factors, and it is variety and site specific according to different levels of risk severity at different extreme temperature values. Therefore, several thermal indices can be defined. To give examples, we used the following measures in studying the occurrences of extreme temperatures (*Dunkel* and *Kozma,* 1981; *Kozma*, 2002):

◇ daily minimum temperature is below −17 °C in the reproductive cycle,

◇ daily minimum temperature is below −21 °C in the reproductive cycle,

◇ daily maximum temperature is above 35 °C in the vegetative cycle.

Hydrothermal coefficient (HTC). We can characterize the combined effect of precipitation and temperature on grapes using the hydrothermal coefficient (*HTC*). This characteristic number, which measures the water supply of a vegetation, is calculated as:

$$HTC = 10P / T_0, \tag{2}$$

where P is the precipitation during the growing season in mm and T_0 is the effective degree days in °C (which is the sum of daily mean temperatures for days of the growing season when this temperature is above 10 °C). In areas, where the *HTC* is below 0.5 mm/°C, grape production is only possible if the humidity is high or if irrigation is applied. The maximum value of the *HTC* is in the range of 1.5–2.5 mm/°C, while its optimal value is around 1.0 mm/°C (*Szeljanyinov*, 1928; *Kozma*, 2002).

3. Results and discussion

According to the RCM simulations, the ADD values were in the range of 1200–1400 °C* in the Hungarian wine regions during the 1961–1990 reference period (*Fig. 1*). These results suggest that climatic conditions were in favor of early- and medium-ripening grape varieties at the end of the 20th century. However, there are certain regions where late-ripening varieties are also produced (*Hajdú*, 2003). The reason for this controversy is that RCMs do not take into account the extra heat the grapes are subjected to when they are grown on hill- and mountainsides and are being exposed to sunlight at lower incoming angles. Thus, maps of heat distribution are biased to lower-than-actual heat supply conditions at hilly terrains (such as the Sopron regions), and consequently, they falsely suggest that these regions are only suitable for low heat demanding grape varieties. As it can be seen in *Fig. 2*, based on *HI*, we could think that heat conditions in Sopron wine regions can only support less heat demanding varieties, and only the Danube regions are optimal for more heat demanding ones. In practice, the Sopron regions are known to be optimal for more heat demanding varieties, which can be explained by taking into account the extra heat the regions are obtaining from sunlight arriving at lower incoming angles.

* These values are only averages, i.e., in some years the *ADD* can be lower or higher. Negative deviations from these averages can lead to an insufficient amount of heat for the ripening of grape varieties that require a longer growing season.

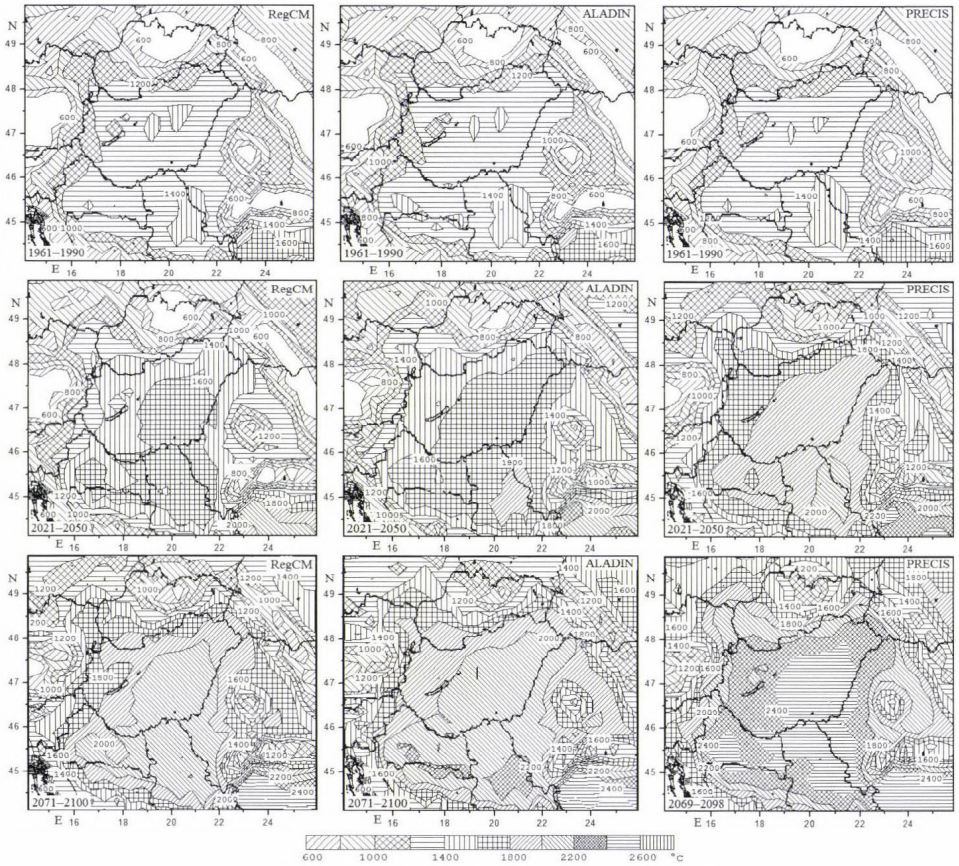

Fig. 1. The values of active degree days (*ADD*) in the Carpathian Basin. The upper row corresponds to the reference period, while the middle and lower rows correspond to the predicted middle and end of the 21st century, respectively. The three columns show our results using the RegCM (left), ALADIN (middle), and PRECIS (right) regional climate models' outputs.

The length of the growing season allowed by the thermal conditions in Hungary is between 160–190 days within the reference period of the RCM simulations. This is about 1 month longer than that is necessary for early- and medium-ripening varieties (see *Table 1* and *Fig. 3*). Thus, we can conclude that the projected thermal conditions by the end of the 21st century are optimal for late-ripening and very-late-ripening grape varieties.

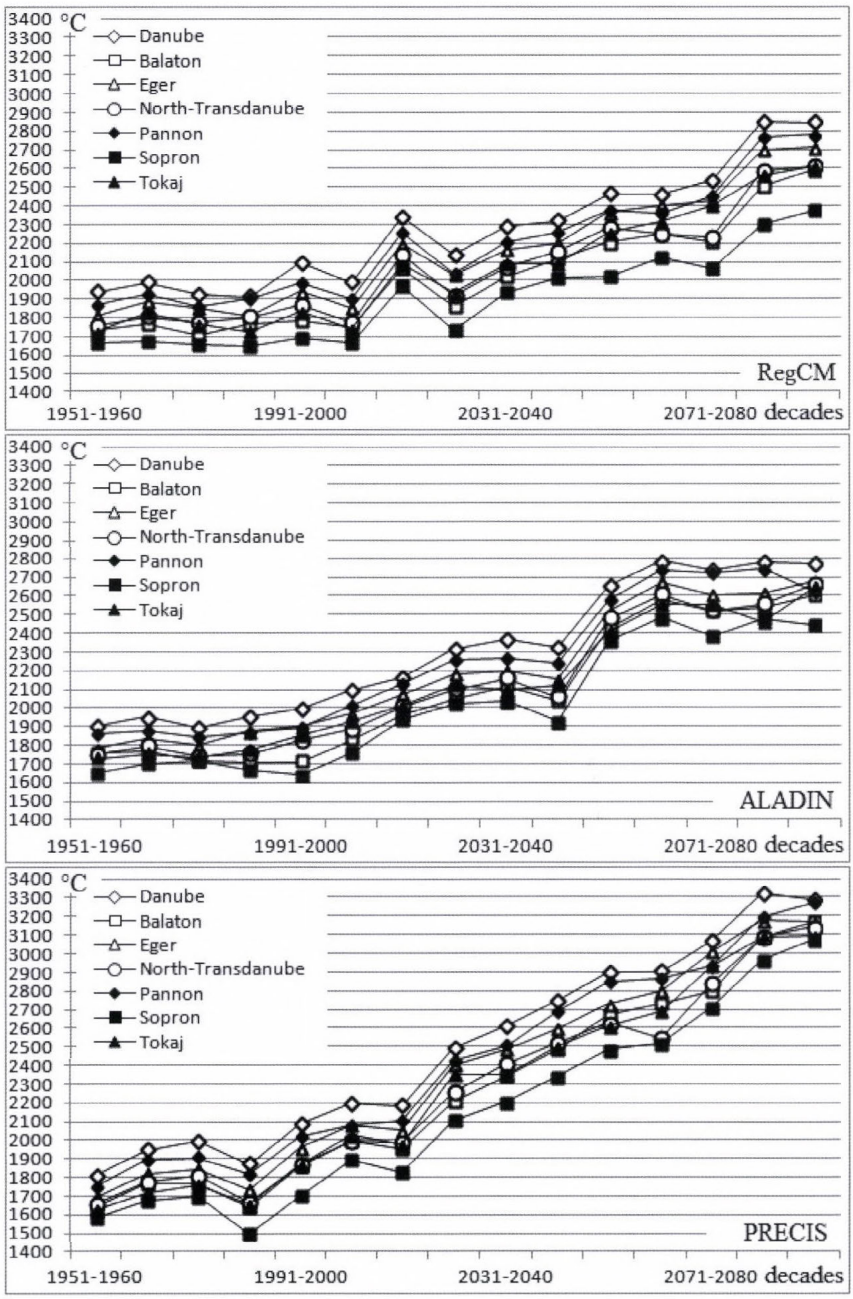

Fig. 2. The temporal evolution of Huglin's heliothermal index (*HI*) in the Carpathian Basin based on the RegCM (upper), ALADIN (middle), and PRECIS (lower) regional climate models' outputs.

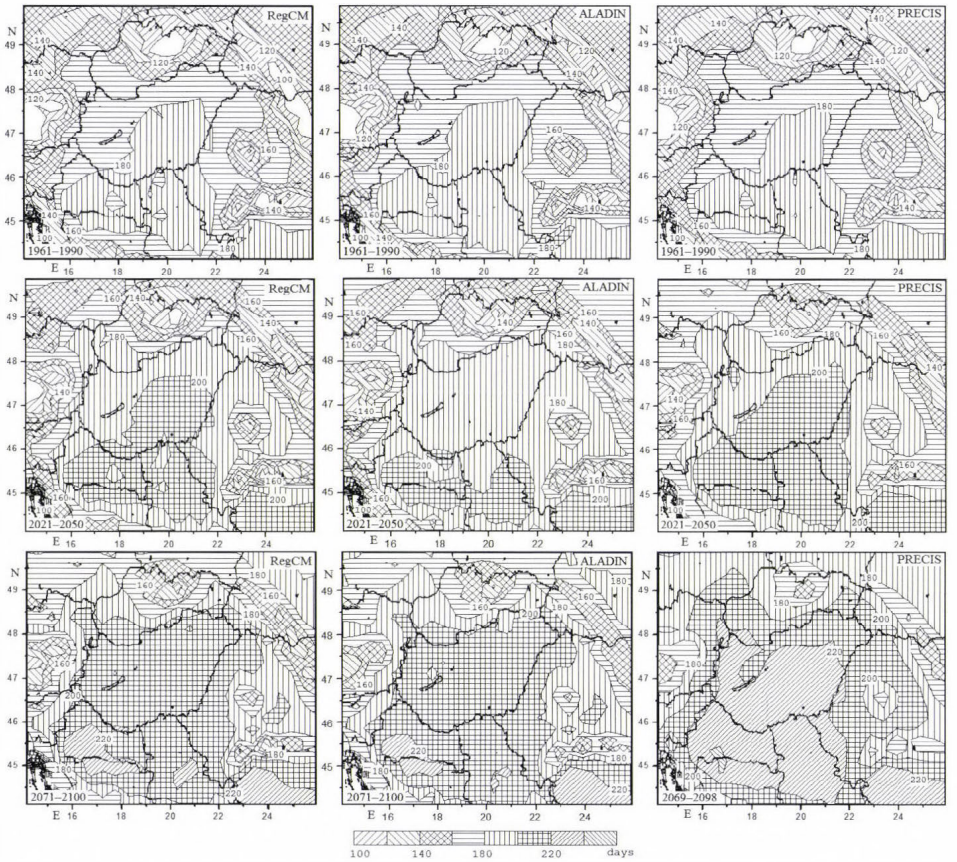

Fig. 3. The length of the growing season in days allowed by thermal conditions. The upper row corresponds to the reference period, while the middle and lower rows correspond to the predicted middle and end of the 21st century, respectively. The three columns show our results using the RegCM (left), ALADIN (middle), and PRECIS (right) regional climate models' outputs.

Results obtained from the ALADIN and RegCM data show a correlation with each other in the middle of the 21st century. Based on these, the *ADD* will increase up to 1400–1700 °C in this period. The value of *HI* is projected to increase to 1800 °C, however, in the Danube region values above 2300 °C will also be possible. The values of *HI* increase with an increased rate from the 1980s in every wine region, as shown in *Fig. 2*.

The PRECIS model simulation suggests a much more significant rise in the index values. The *ADD* can increase up to 1600–2000 °C in the middle of the 21st century. *HI* will reach 2300 °C in the whole country. In *Fig. 2*, curves corresponding to the PRECIS model increase with the highest rate, which shows that this model predicts the greatest change in the local climate by the middle of the 21st century.

All three models predict longer growing season in the immediate future (see *Fig. 3*) compared to the reference period. By the middle of the 21st century, the vegetation cycle length allowed by thermal conditions can be as long as 180–210 days, however, the change will be slightly smaller (180–200 days) according to the ALADIN model.

Similar tendencies are expected to occur in the end of the 21st century. Based on the ALADIN and RegCM models, the *ADD* can be as high as 1700–2200 °C. Similar to the results for the end of the 21st century, PRECIS predicts a more remarkable change: according to this model, *ADD* can be between 2000–2500 °C. In this period, all three models predict *HI* to be above 2300 °C throughout the whole country.

The vegetation cycle length allowed by thermal conditions can be even longer in the far future (see *Fig. 3*). Its duration can reach 200–220 days, or 210–230 days according to the PRECIS model.

All these suggest that certain regions will allow the ripening of late-ripening grape varieties by the middle of the 21st century. As the increased heat allows the development of color- and aroma essences, growing a higher ratio of red wine grapes will be feasible in several wine regions. According to results corresponding to the end of the 21st century, the thermal conditions of the Hungarian wine regions will allow the growing of Mediterranean red wine grapes.

In addition to the average conditions, the occurrences of extreme temperatures in the reproductive and vegetation cycles also have important roles. Since PRECIS simulation does not include any occurrence of daily minimum temperature below −17 °C, we only analyze the extremes based on the other two RCMs simulations.

The regional distribution of the number of days with minimum temperatures below −17 °C (as obtained from the RegCM and ALADIN simulations) is in a good agreement with the results presented in *Dunkel* and *Kozma* (1981) (see *Fig. 4*). However, note, that the time interval investigated in *Dunkel* and *Kozma* (1981) is slightly different from our reference period.

We found that less frost-tolerant grape varieties suffered frost damage in every 2–3 years within the reference period (see *Table 3*). This occurrence is projected to decrease by the middle of the 21st century to only one major frost damage in the winter season in every 4–10 years. The risk of frost damage will almost disappear in the end of the 21st century.

The RCM simulations underestimate the number of days with a minimum temperature below −21 °C compared to the findings of *Dunkel* and *Kozma* (1981). This difference can be related to the slightly different periods applied. Independently from this fact, the occurrence of extreme cold temperatures will decrease in the middle of the 21st century, and almost completely disappear in the end of the 21st century.

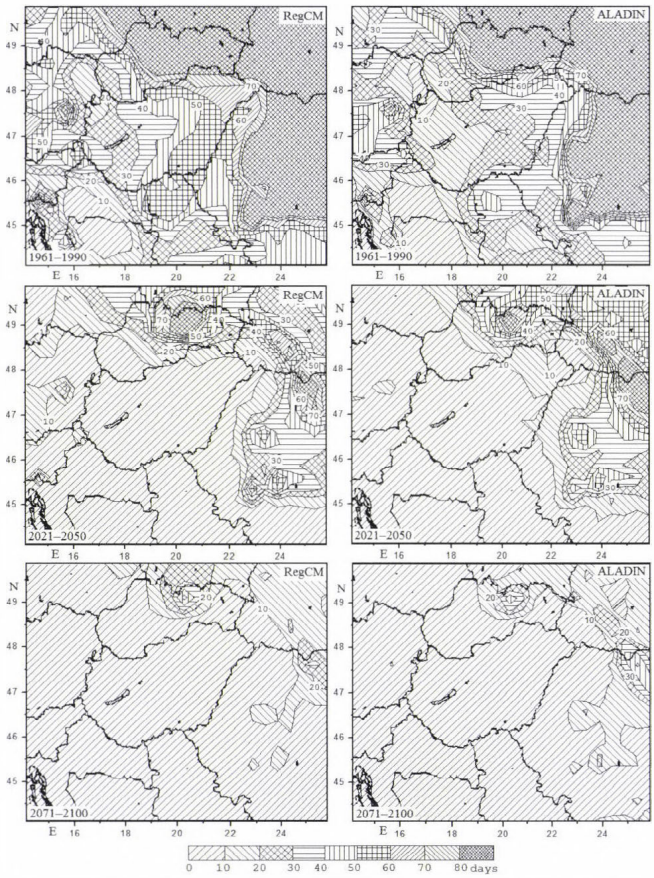

Fig. 4. The number of days in the reproductive cycle with minimum temperature below –17 °C. The two columns correspond to the RegCM (left) and ALADIN (right) simulations' results. The rows of the figure show the model results for the reference period (upper), and the predictions for the middle (middle) and the end (lower) of the 21st century.

The plants can be damaged due to extreme hot days in the growing season, too. In the reference period, the occurrence of days with maximum temperature above 35 °C was one per 2–10 years according to the RCM results (see *Fig. 5*). The most of such years are simulated by the RegCM model, and the least by the ALADIN model. On yearly average, about 1–4 days occurred when the maximum temperature exceeded 35 °C.

Table 3. The number of years having at least one day in the reproductive cycle with minimum temperature below –17 °C. The numbers are given for the different Hungarian wine regions, and using the RegCM (Re) and ALADIN (AL) simulations outputs.

	Danube		**Balaton**		**Eger**		**North-Transdanubia**		**Pannon**		**Sopron**		**Tokaj**	
	Re	AL	Re	AL	Re	AL	Re	AL	Re	AL	Re	AL	Re	AL
Reference period	19	17	14	15	21	19	16	16	15	12	11	10	21	18
Middle of the 21st cenrury	5	8	6	2	8	8	5	3	5	2	2	1	7	7
End of the 21st century	1	2	2	3	2	4	2	1	1	1	0	2	1	2

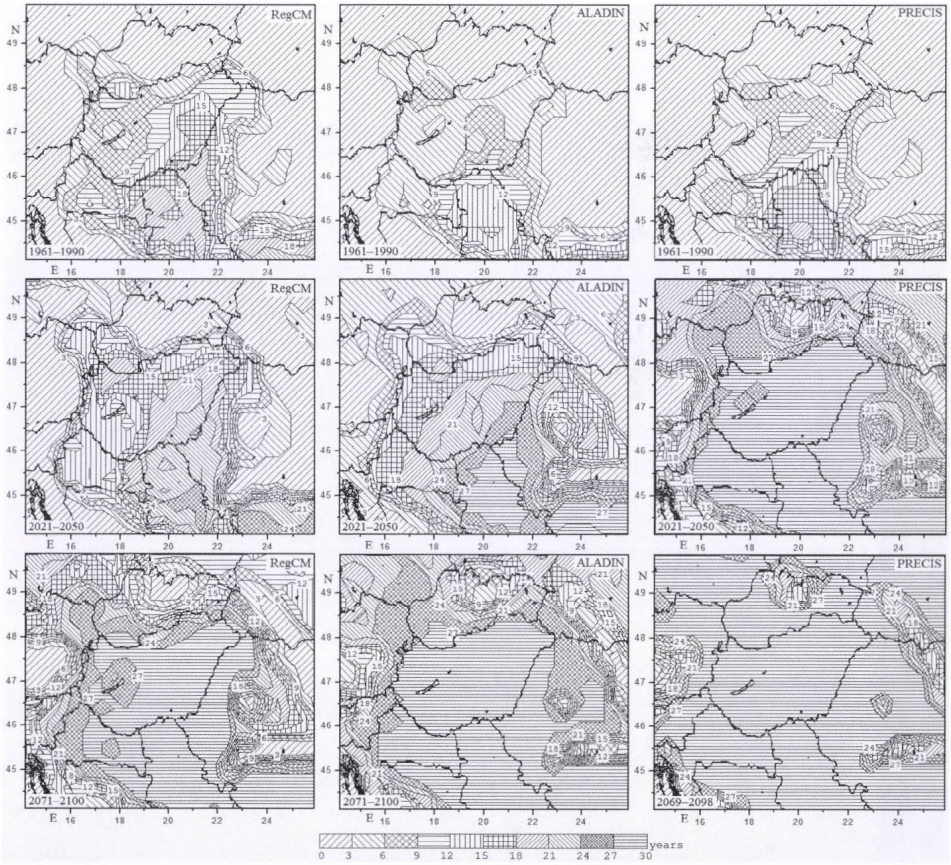

Fig. 5. The number of days in the vegetation cycle with maximum temperature above 35 °C. The two columns correspond to the RegCM (left), ALADIN (middle), and PRECIS (right) simulations' results. The rows of the figure show the model results for the reference period (upper), and the predictions for the middle (middle) and the end (lower) of the 21st century.

There will be a drastic rise in the number of years with extreme high temperature both in the middle and the end of the 21st century. All three models predict such days to occur in every two years in the middle of the 21st century, and in every year in the end of this century. In years, when there is at least one day with a maximum temperature above 35 °C, there will be a rise in the number of such days both in the middle and the end of the 21st century. The highest occurrence of such days is projected in Duna region. According to the RegCM predictions, there will be 2–4 days yearly with extreme hot temperatures in the middle of the 21st century, and can be as many as 5–13 such days per year in the end of this century. The rise in the number of extreme hot days is even greater when using the ALADIN and PRECIS simulations' outputs. Based on these models, we can expect 8–16 extreme hot days per year in the middle of the 21st century and 27–40 such days per year in the the end of this century.

Our results based on the three RCMs' simulations show (see *Table 4*) that the *HTC* will not reach the critical threshold value of 0.5 mm/°C neither in the immediate, nor in the far future. This means that the climatic conditions will be suitable for wine production in the Hungarian wine regions. It depends on the deviation of the *HTC* from 1 mm/°C whether these conditions move closer to or away from the optimum in particular regions.

Table 4. The values of the hydrothermal coefficient (*HTC*, in mm/°C) in the different Hungarian wine regions based on RegCM (Re), ALADIN (AL), and PRECIS (PR) model predictions.

	Danube			**Balaton**			**Eger**			**North-Transdanubia**		
	Re	AL	PR	Re	AL	PR	Re	AL	PR	Re	AL	PR
Reference period	0.90	0.92	0.89	1.12	1.21	1.15	1.05	1.07	1.03	0.99	1.03	1.00
Middle of the 21st cenrury	0.90	0.83	0.71	1.18	1.14	0.95	1.02	0.95	0.72	1.01	0.98	0.78
End of the 21st century	0.75	0.71	0.59	1.01	0.88	0.75	0.85	0.78	0.60	0.87	0.78	0.67

	Pannon			**Sopron**			**Tokaj**		
	Re	AL	PR	Re	AL	PR	Re	AL	PR
Reference period	0.92	0.98	0.94	1.24	1.32	1.32	1.15	1.19	1.14
Middle of the 21st cenrury	0.96	0.89	0.79	1.28	1.29	1.04	1.13	1.02	0.79
End of the 21st century	0.82	0.75	0.68	1.14	1.00	0.82	0.93	0.81	0.63

In the reference period, all three models showed excess heat in Danube and Pannon regions, and excess precipitation in Balaton, Eger, Sopron, and Tokaj regions. All three models resulted in North-Transdanubia region being climatic optimal.

The changes in the middle of the 21st century are not unambiguous. RegCM simulation does not show any change for Danube region, while for Balaton and Pannon regions it predicts an increase in excess precipitation. The climatic conditions are projected to become more suitable for grape production in Eger, Pannon, and Tokaj regions. ALADIN simulation predicts a decrease in excess precipitation or an increase in excess heat for all regions. This could lead to more favorable conditions in Balaton, Eger, Sopron, and Tokaj. Similarly to ALADIN, PRECIS simulation shows either a decrease in excess precipitation or an increase in excess heat for all wine regions, which results in an improvement in Balaton and Sopron regions.

All three models project similar conditions for the end of the 21st century, which means that we expect a decrease in excess precipitation or an increase in excess heat in all regions compared to the reference period. According to all three models, this again means better conditions for Sopron region and worse for Danube, Eger, North-Transdanubia, and Pannon regions compared to the conditions in the reference period. This change lead to more favorable conditions in Balaton (according to RegCM and ALADIN) and Tokaj (according to RegCM) regions.

4. Conclusions

Our investigations showed that in terms of modeled heat conditions, the 21st century will favor red wine grape and late-ripening varieties. We can derive this conclusion from the estimated increasing tendency of active degree days and of Huglin's heliothermal index. At the same time, we expect longer growing season allowed by the climatic conditions.

Frost-damages in the dormancy periods would become more rare due to the warming climate. However, the number of days with maximum temperature above 35 °C may increase, which could lead to serious heat damages. There should be more care spent on preventing and mitigating damages due to increased heat stress using adequate horticultural practices.

We expect a decrease in the hydrothermal coefficient in all regions by the end of the 21st century, which can lead to non-optimal climatic conditions, because heat as its denominator will likely be dominant.

Acknowledgments—Simulation of the PRECIS regional climate model was supported by grant OTKA K-78125. The authors are grateful for Ildikó Pieczka for providing bias-corrected model outputs. The RegCM and ALADIN simulations were developed within the ENSEMBLES project (505539) which was funded by the EU FP6 integrated program. The E-OBS database was provided by the

ENSEMBLES and ECA&D projects. This work has been supported by OTKA grants K81933 and K81975, also, by the projects KMR_12-1-2012-0206 and GOP-1.1.1.-11-2012-0164. The project was supported by the European Union and the European Social Fund (TÁMOP-4.2.1/B-09/1/KMR-2010-0003, FuturICT.hu grant no.: TÁMOP-4.2.2.C-11/1/KONV-2012-0013). We would also like to thank Peter Raffai for his valuable help with the English translation.

References

Davitaja, F.F. (*Давитая*, Ф.Ф.), 1959: Климатические показатели сырьевой базы виноградо-винодельческой промышленности. *Труды ВНИИВИВ „Магарач", 6(1)* 12–32. (in Russian)

Déqué, M., *Marquet*, P., and *Jones*, R.G., 1998: Simulation of climate change over Europe using a global variable resolution general circulation model. *Clim. Dynam. 14*, 173–189.

Dunkel, Z. and *Kozma*, F., 1981: A szőlő téli kritikus hőmérsékleti értékeinek területi eloszlása és gyakorisága Magyarországon. *Légkör 26. 2*, 13–15. (in Hungarian)

Formayer, H. and *Haas*, P., 2009: Correction of RegCM3 model output data using a rank matching approach applied on various meteorological parameters. Deliverable D3.2 RCM output localization methods (BOKU-contribution of the FP6 CECILIA project)

Giorgi, F., *Marinucci*, M.R., *Bates*, G.T., and *DeCanio*, G., 1993: Development of a second generation regional climate model (RegCM2). Part II: Convective processes and assimilation of lateral boundary conditions. *Mon. Weather Rev. 121*, 2814–2832.

Hajdú, E., 2003: Magyar szőlőfajták. Mezőgazda Kiadó, 11–223. (in Hungarian)

Haylock, M.R., *Hofstra*, N., *Klein Tank*, A.M.G., *Klok*, E.J., *Jones*, P.D., and *New*, M., 2008: A European daily highresolution gridded data set of surface temperature and precipitation for 1950-2006., *J. Geophys. Res. 113*, 1–12.

Huglin, P., 1978: Nouveau mode d'évaluluation des possibilites héliothermiques d'un milieo viticole. In: *Proceedings of the Symposium International sur l'ecologie de la Vigne. Ministére de l'Agriculture et de l'Industrie Alimentaire, Contanca,* 89–98. (in French)

Kozma, P., 2002: A szőlő és termesztése I. Akadémiai Kiadó, 13–19., 213–272. (in Hungarian)

van der Linden, P. and *Mitchell*, J.F.B., 2009: Summary of research and results from the ENSEMBLES project. Met Office Hadley Centre, Exeter, UK. 164.

Nakicenovic, N. and *Swart*, R.J., 2000: Emissions Scenarios 2000 – Special Report of the Intergovernmental Panel on Climate Change. Cambridge University Press, Cambridge. 570p.

Pieczka, I., *Pongrácz*, R., *Bartholy*, J., *Kis*, A., and *Miklós*, E., 2011: A szélsőségek várható alakulása a Kárpát-medence térségében az ENSEMBLES projekt eredményei alapján. In (Szerk.*: Lakatos M.)* 36. Meteorológiai Tudományos Napok - Változó éghajlat és következményei a Kárpát-medencében. Országos Meteorológiai Szolgálat, Budapest. 77–87. (in Hungarian)

Pieczka, I., 2012: A Kárpát-medence térségére vonatkozó éghajlati szcenáriók elemzése a PRECIS finom felbontású regionális klímamodell felhasználásával. PhD értekezés. ELTE Meteorológiai Tanszék, Budapest. 1–95. (in Hungarian)

Pongrácz, R., *Bartholy*, J., *Miklós*, E., 2011: Analysis of projected climate change for Hungary using ENSEMBLES simulations. *Appl. Ecol. Environ. Res. 9*, 387–398.

Szeljanyinov, G., T., 1928: On agricultural climate valuation. *Proc.of Agricul. Meteorol. 20,* 165–177.

Szenteleki, K., *Ladányi*, M., *Gaál*, M., *Zanathy*, G., and *Bisztray*, Gy. D., 2012: Climatic risk factors of Central Hungarian grape growing regions. *Appl. Ecol. Environ. Res 1*, 87–105.

Wilson, S., *Hassell*, D., *Hein*, D., *Jones*, R., and *Taylor*, R., 2007: Installing and using the Hadley Centre regional climate modelling system, PRECIS. Version 1.5.1. UK Met Office Hadley Centre, Exeter.

IDŐJÁRÁS

Quarterly Journal of the Hungarian Meteorological Service
Vol. 118, No. 3, July – September, 2014, pp. 207–216

Positive bias caused by residual water in reference PM_{10} measurements

Kornélia Imre[1]*, Ágnes Molnár[1], Viktor Dézsi[2], and András Gelencsér[3]

[1]*MTA-PE Air Chemistry Research Group, Egyetem u. 10, H-8200 Veszprém, Hungary*

[2]*Hungarian Meteorological Service, Air Quality Reference Centre, Gilice tér 39, H-1181 Budapest, Hungary*

[3]*Department of Earth and Environmental Sciences, University of Pannonia, Egyetem u. 10, H-8200 Veszprém, Hungary*

**Corresponding author: kornelia@almos.uni-pannon.hu*

(Manuscript received in final form March 4, 2014)

Abstract—Dry aerosol mass concentrations (PM_{10}, $PM_{2.5}$) are determined after conditioning of the filter at t=20±1 °C and RH=50±5% for 48 hours according to the standard protocol EN 12341. The main result of this work is that applying the standard pre-conditioning step, complete removal of adsorbed water cannot be attained. In our experiment, aerosol samples collected in Budapest between November 2008 and March 2010 using a CEN (European Committee for Standardization) gravimetric sampler (Digitel, DHA-80) were studied. Following PM_{10} mass concentration measurements according to the EN 12341 protocol, we repeated the gravimetric aerosol mass measurements in the laboratory using a glove box after in-situ pre-conditioning for 48 h at t=20±1 °C and RH<30%. We assumed that at this low relative humidity all the adsorbed residual water was removed, and the absolute dry mass concentrations of PM_{10} could be determined (referred in the following as dry PM_{10} concentration). The mass concentration of adsorbed residual water, defined as the difference between the results of the standard and dry PM_{10} measurements, varied greatly in the range of 0.05–16.9 $\mu g\ m^{-3}$. Expressed relative to the absolute dry PM_{10} mass concentrations, the residual water content in the standard measurement procedure amounted to 4.2±1.5% and 7.9±0.8% in summer and winter, respectively. In winter, relative contributions of adsorbed water as high as 33.2 m/m% was found. The significant seasonal differences as well as the large variations between individual samples may depend on various factors such as the chemical composition of the samples, particle load, and the RH history of the particles before and after sample collection. This last factor is expected to exert rather significant influence on the amount of adsorbed residual water, yet it is impossible to reconstruct. These findings have severe implications on reported dry PM_{10} mass concentrations using the EN 12341 protocol, especially in the winter period when most limit exceedances occur.

Key-words: urban PM_{10}, standard protocol, adsorbed residual water, dry mass concentration, low relative humidity

1. Introduction

Liquid water is a highly variable, but very often overlooked constituent of atmospheric particulate matter (PM_{10} or $PM_{2.5}$). The interaction between ambient aerosol particles and water vapor plays a crucial role in many fundamental atmospheric processes. Adsorbed water may significantly increase the size of the particles, which, in turn, enhances the extinction (mainly scattering) of visible light in the atmosphere. This is manifested in strongly reduced standard visibility at high relative humidity (RH) (*Cheng et al.,* 2011, *Deng et al.,* 2011). Liquid water on aerosol particles can serve as a medium for multiphase reactions (e.g., sulfur conversion in sea-salt aerosol particles, *Sievering et al.* (1991)), or secondary organic aerosol formation *Strollo* and *Ziemann* (2013); *Ervens* and *Volkamer* (2010). In supersaturated air, particles called cloud condensation nuclei can grow into cloud or fog droplets. The interaction between particles and water vapor depends on the relative humidity as well as the size, chemical composition, and wettability of the particles. Based on differences in their chemical compositions, particles of various origins can behave quite differently with changing humidity, from being purely hydrophobic to strongly hygroscopic. Hygroscopic particles take up water continuously with increasing RH, whereas deliquescent particles do not adsorb water up to a certain RH limit called the deliquescence point (DRH). At this point, however, a sudden phase change occurs with a steep increase in the mass of the particles. Increasing the RH further above the DRH, the liquid particle will continue to grow. However, once such a particle is turned into liquid, decreasing the RH will not make the particle recrystallize at the DRH. Below the DRH, the liquid particle becomes supersaturated resulting in a metastable state until the RH decreases below a critical value at which recrystallization occurs (*Hansson et al.,* 1998). This RH is called efflorescence relative humidity (ERH). For example, aqueous ammonium sulfate is saturated with respect to its crystalline phase at 82.6% RH at 260 K (*Clegg et al.,* 1998; *Onasch et al.,* 1999; *Cziczo* and *Abbatt,* 1999), whereas laboratory studies show that homogeneous crystallization of droplets does not occur before RH drops to 32.7% (*Onasch et al.,* 1999). Conversely, solid ammonium sulfate does not deliquesce at RH lower than 82.6%. Therefore, in the range 32.7% < RH < 82.6% the physical state of such a particle in the atmosphere depends on its RH history (*Colberg et al.,* 2003), the particles exist as a metastable droplet when the particles had not been exposed to relative humidity greater than their deliquescence RH.

There is often a discrepancy in chemical mass closures of atmospheric aerosol samples when they are normalized to gravimetrically measured mass of particulates. In other words, after all identified components are quantified, a part of PM mass remains unidentified. One possible source for the observed discrepancy between gravimetric PM mass and the total mass of all identified

components is particle-bound water. The amount of water in PM samples varies for different samples and measurement sites, depending on the particle composition and the ambient relative humidity and temperature (e.g., *Warneck,* 2000). According to *Kajino et al.* (2006), in winter when the relative humidity is high and the concentration of hygroscopic compounds is also high, approximately 70% of unidentified non-carbonaceous fraction of urban $PM_{2.5}$ (or about 10% of $PM_{2.5}$ mass) was assumed to be water. The authors also found that the aerosol water content in winter was 6–7 times higher in winter than in summer.

In spite the fact that *Saxena et al.* (1995) pointed out the importance of atmospheric water-soluble organic carbon (WSOC) for the observed hygroscopic behavior of atmospheric aerosols, the water uptake of aerosol particles has been largely associated with their inorganic constituents. Depending on the ambient conditions during and prior to sampling, particles can either adsorb or lose water under post-equilibration (*Tsyro,* 2005). The relationship among particle mass and composition and particle water content is rather complicated due to hysteresis in the behavior of particle-bound water. In many cases the atmospheric aerosol particles show strong RH-hysteresis behavior and retain substantial particle-bound water (*Santarpia et al.,* 2004; *Randriamiarisoa et al.,* 2006). This means that potentially a significant fraction of strongly hygroscopic particles exist as supersaturated droplets even at RH as low as 50%. One possible explanation for the significant amount of retained water is the acidity of the particles. This was observed in several places, e.g., in Pittsburgh, USA (*Khlystov et al.,* 2005) and in Switzerland (*Fisseha et al.,* 2006). According to *Tsyro* (2005), pure ammonium sulfate particles can still retain as much as 30% (m/m) of water at 50% relative humidity. *Ansari* and *Pandis* (1999) investigated the hysteresis of equimolar model aerosol mixtures (Na_2SO_4-NaCl and Na_2SO_4-NaCl-$NaNO_3$) and found that the residual mass of retained water at RH=50% was 83% and 71%, respectively. On the other hand, beside particle acidity, a number of organic components are shown to inhibit the aerosol deliquescence and efflorescence behavior (*Marcolli* and *Krieger,* 2006). *Zardini et al.* (2008) showed that the retained mass of water in the case of ammonium sulfate: adipic acid (2:1.1) model mixture was 30% at RH=50% following equilibrium dehumidification.

In recognition of the water-retaining characteristics of atmospheric particulate matter, standard off-line gravimetric measurement protocols all require the relative humidity to be set at a relatively low value and the filter samples be equilibrated before weighing. In Europe, the reference method developed by the European Committee for Standardization (CEN) prescribes that the filters should be equilibrated for 48 h prior to weighting at RH=50±5% and t=20±2 °C before and after sampling. This standard reference method is used to validate the readings of automatic beta-gauge

monitors (FH 62-IN, Thermo Andersen) that are in use in hourly PM concentration measurements.

Several studies indicated that there were deviations between automatic and standard off-line PM mass concentration measurements (*Shin et al.,* 2011, *Takahashi et al.,* 2008, *Salminen* and *Karlsson,* 2003), with higher differences at high ambient RHs (*Chang* and *Tsai,* 2003). These results also imply the significance of retained water of particles under the standard reference methods.

The objective of this study is to determine the residual water content of PM filter samples collected in winter and summer in the city of Budapest, Hungary, which are equilibrated according to the standard analysis protocol. This is done to determine the potential bias of standard gravimetric measurements due to the incomplete removal of particle-bound water upon equilibration.

2. Methodology

2.1. Aerosol sampling

The aerosol sampling was carried out in Budapest (Marczell György Observatory, Hungarian Meteorological Service) at a suburban sampling site. The aerosol sampling were carried out in 57 consecutive days in winter of 2008–2009, 22 days in summer of 2009, and further 75 days in winter of 2009–2010.

PM_{10} aerosol samples were collected on glass fiber filters (Munktell MG 160, d=150 mm) at a flow rate of 30 $m^3 h^{-1}$ by using a Digitel-DH 80 reference sampler (CEN, 1998) at a height of 2 m.

2.2. Gravimetric measurements

Before and after the sampling, glass fiber filters were placed for 48 hours into an isolated chamber at a temperature of 20±1 °C and RH of 50±5%, as required by the EN 12341 standard protocol (CEN, 1998). Then PM_{10} mass was determined by weighing with an electrical micro-balance (Sartorius, BP 211 D) of 10 μg accuracy.

Filter blanks were treated in the same way. The relative humidity was measured by a hygrograph, which was calibrated in the climate chamber of the Hungarian Meteorological Service. The detailed measurement conditions can be found in *Imre* and *Molnár* (2008). In order to determine the residual water content of aerosol mass measured according to the EN 12341 protocol, the filter sample was equilibrated for another 48 h at t=20±1 °C and RH<20% prior to the following gravimetric measurement. The relative humidity in the measurement chamber was set by DRIERIT (calcium sulfate, W.A. Hammond Drierite Co. Ltd.) heated at 230 °C for 2 hours.

3. Results and discussions

The PM_{10} dry mass concentrations measured from the collected filter samples according to EN 12341 standard protocol are shown *Fig. 1.* The 24-hour health threshold limit for PM_{10} concentration in Hungary (and EU) is 50 $\mu g\ m^{-3}$, while the air quality public warning "Information" and "Alert" threshold limits are 75 and 100 $\mu\ gm^{-3}$, respectively, as regulated by the Ministry of Rural Development (4/2011) are also indicated in the figure.

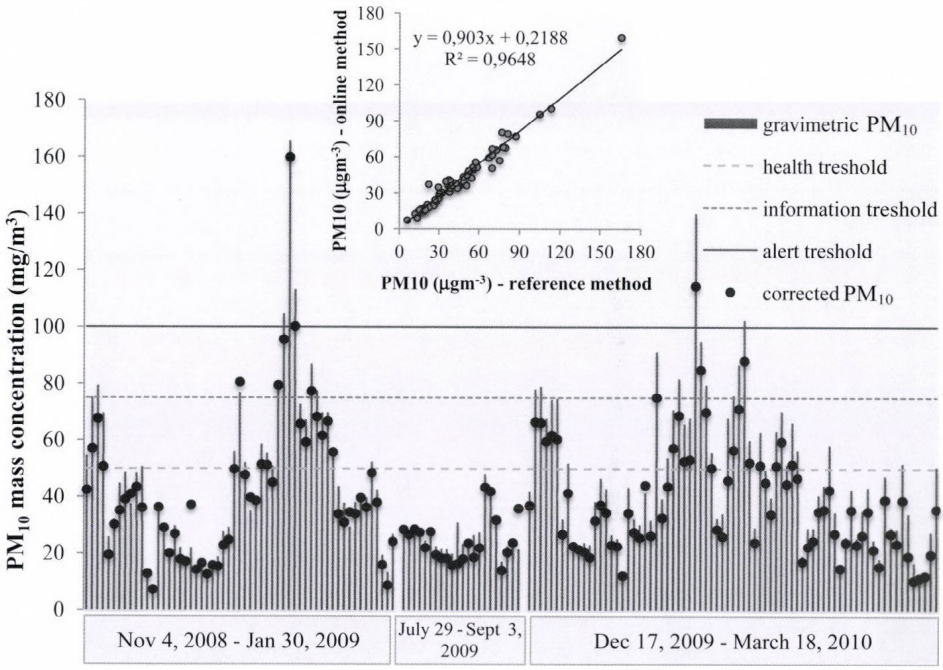

Fig. 1. Gravimetrically determined dry mass concentration at 50% RH according to EN 12341 (CEN 1998) and the relationship between the online and gravimetric PM_{10} concentrations (inserted picture).

According to the regulations, the evaluation of the limit exceedances should be based on the 24 h PM_{10} mass concentrations measured by an automatic beta-gauge monitor FH 62-IN (Thermo Andersen) and not on those measured by the reference method. For this reason these data are also shown in *Fig. 1.* (It should be noted that this instrument was located adjacent to the Digitel-DH 80 reference sampler and the data of beta-gauge monitor are averaged for the time period of sample collection.) Adding this constraint (to the

calculation) the measured PM_{10} reference dry mass concentrations exceeded the alert threshold for 34 days, for additional 14 days the information, threshold and for another 5 days the health limits.

In the following we considered that under the equilibrium conditions required by the reference method (20±1°C and RH of 50±5% for 48 h), residual water was retained in the particles. In order to determine the residual water content of the aerosol, further gravimetric measurements were necessary that is specified by equilibration at t=20±1 °C and RH<30% lasting for 48 h. The mass concentration of water retained under the conditions of the standard protocol was determined as a difference between the mass concentrations measured according the EN 12341 protocol and the dry mass concentration specified above. The mass fraction of residual water expressed in percentage of the PM_{10} mass concentrations measured by the reference method is shown in *Fig. 2*. It is interesting to note, that despite the fact, that the aerosol water content was higher in winter than in summer, no significant relationship between the ambient RH (during the sampling) and the measured water content was found.

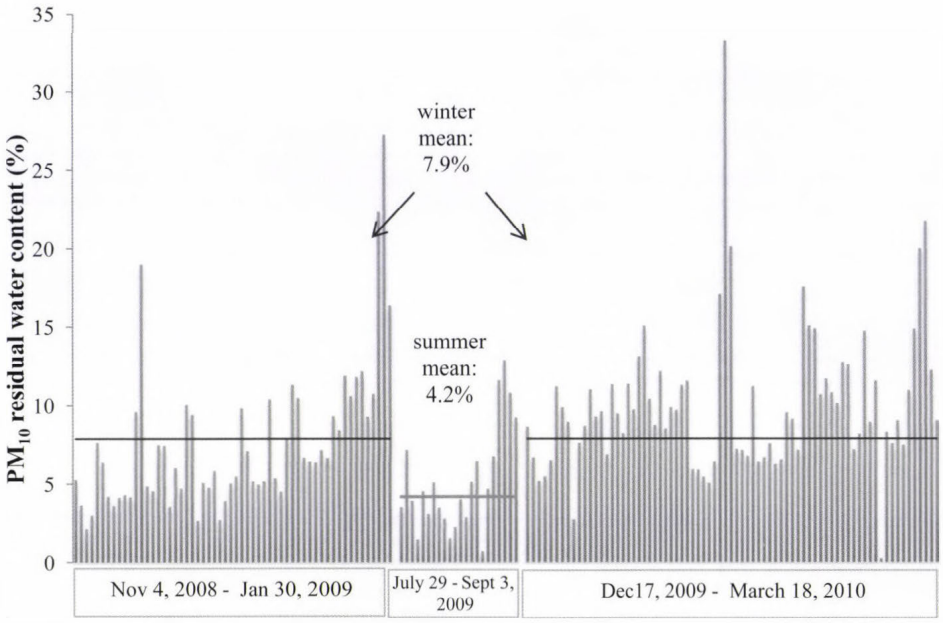

Fig. 2. Experimentally determined residual water content of PM_{10} under the conditions on EN 12341 protocol.

It follows that the mass fraction of residual water quantity reflects the share of particle-bound water to the mass of particles measured at 30% RH. The mass concentrations of residual water varied between 0.05 and 16.9 $\mu g\ m^{-3}$. The histograms of the relative contributions of residual water are depicted in *Fig. 3* both for summer and winter.

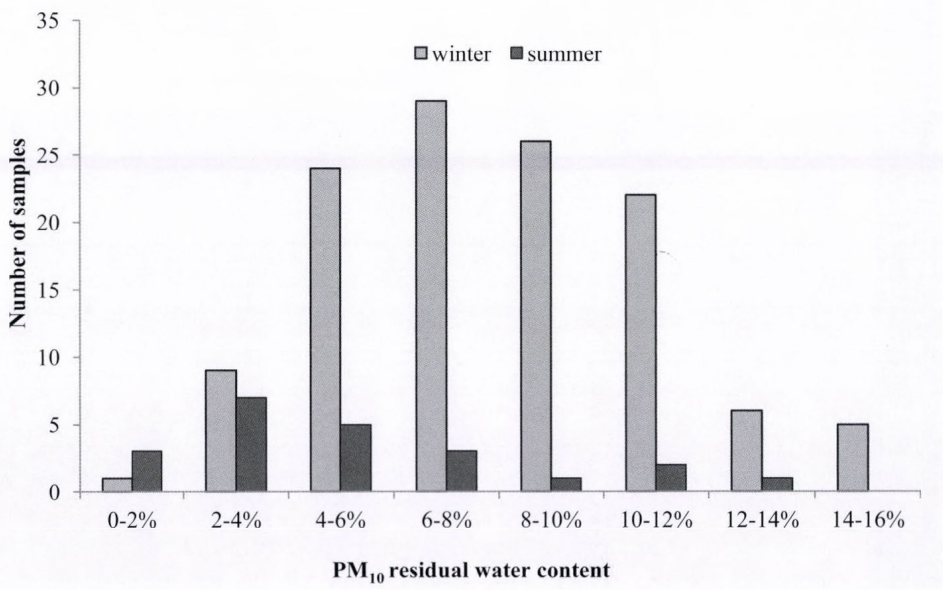

Fig. 3. Frequency distributions of residual water content of PM_{10} mass measured according to EN 12341 protocol.

The frequency of the contribution of residual water can be well described by a log-normal distribution in both seasons. In summer the mean water content is 4.2±1.5% (p=95% (Student-probe), while in winter the peaks are significantly shifted towards higher values (mean: 7.9±0.8%, p=95%) indicating that in winter the aerosol has lower DRH values and more hygroscopic than in summer.

After determination of the water content of the aerosol particles, the PM_{10} mass concentrations were corrected with these water content values. An important consequence of replacing the measured PM_{10} reference with the absolute dry mass concentrations is that the number of total exceedances of the health, information, and alert limits could be reduced by 9 (26%), 7 (50%), and 2 (40%) days, respectively (*Fig. 4*).

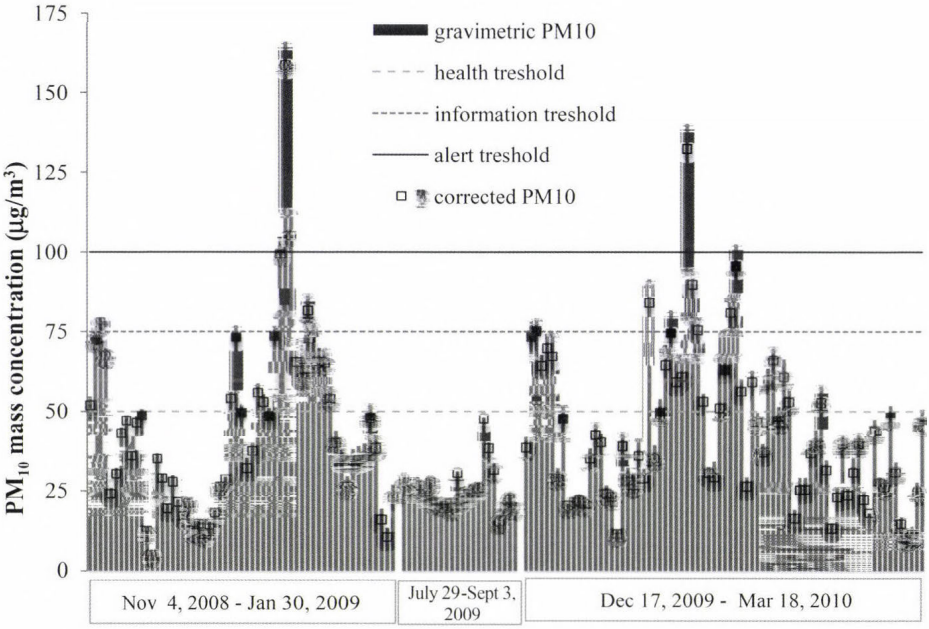

Fig. 4. Gravimetrically determined and calculated dry mass concentrations.
(Full squares indicate when the corrected PM_{10} concentration falls below the threshold limits.)

The results of our experiments suggest that PM_{10} filters measured gravimetrically according to the EN 12341 protocol do retain variable but sometimes significant amount of residual water at RH of 50±5% and at temperature of 20±1 °C after equilibration for 48 h. This finding questions that the reference measurements yield dry PM_{10} mass concentrations as intended to be according to the EN 12341 protocol. These results are not necessarily surprising based on previous laboratory and theoretical studies that showed that many abundant aerosol constituents exhibit hysteresis in their hygroscopic behavior and retain water down to their efflorescence RH well below 50% (*Weingartner et al.,* 1995; *Zhou et al.,* 2000; *Gao et al.,* 2008). Since adsorbed water does not pose any health risk but contributes quite significantly to measured PM_{10} mass concentration, the justification of environmental legislation based on EN 12341 protocol is questionable. Given the complexity of the issue and for lack of feasible methodological solutions, we suggest that the uncertainties of measured PM_{10} concentration values should be extended with a statistically derived seasonal factor that may account for the residual water content that causes positive bias in the reference measurements. Since the scope of our study is limited, extension of this research to biases caused by residual water in the readings of automatic beta-gauge monitors is clearly warranted.

Acknowledgements–Present article was published in the frame of the project TÁMOP-4.2.2.A-11/1/KONV-2012-0064: „Regional effects of weather extremes resulting from climate change and potential mitigation measures in the coming decades". The project is realized with the support of the European Union, with the co-funding of the European Social Fund.

References

Ansari, A.S. and *Pandis, S.N.*, 1999: Prediction of multicomponent inorganic atmospheric aerosol behaviour. *Atmos Environ 33,* 745–757.

CEN, 1998: Air Quality—Determination of the fraction of suspended particulate matter—Reference method and field test procedure to demonstrate reference equivalence of measurement methods. EN 12341.

Cheng, S., Yang, L., Zhou, X., Xue, L., Gao, X., Zhou, Y., and *Wang, W.*, 2011: Size-fractionated water-soluble ions, situ pH and water content in aerosol on hazy days and the influences on visibility impairment in Jinan, China. *Atmos Environ 45,* 4631–4640.

Chang, C.T. and *Tsai, C.J.*, 2003: A model for the relative humidity effect on the readings of the beta-gauge monitor. *Aerosol Sci 34,* 1685–1697.

Clegg, S.L., Brimblecombe, P., and *Wexler, A.S.*, 1998: A thermodynamic model of the system H^+-NH_4^+-SO_4^{2-}-NO_3^--H_2O at tropospheric temperatures. *J. Phys. Chem. A102*, 2137–2154.

Cziczo, D.J. and *Abbatt, J.P.D.*, 1999: Deliquescence, efflorescence, and supercooling of ammonium sulfate aerosols at low temperature: Implications for cirrus cloud formation and aerosol phase in the atmosphere. *J. Geophys. Res. 104,* 13781–13790.

Colberg, C.A., Luo, B.P., Wernli, H., Koop, T., and *Peter Th.*, 2003: A novel model to predict the physical state of atmospheric H2SO4/NH3/H2O aerosol particles. *Atmos. Chem. Phys. 3,* 909–924.

Deng, J., Wang, T., Jiang, Z., Xie, M., Zhang, R., Huang, X., and *Zhu, J.*, 2011: Characterization of visibility and its affecting factors over Nanjing, China. *Atmos. Res. 101,* 681–691.

Ervens, B. and *Volkamer, R.*, 2010: Glyoxal processing by aerosol multiphase chemistry: towards a kinetic modeling framework of secondary organic aerosol formation in aqueous particles, *Atmos. Chem. Phys. 10,* 8219–8244.

Fisseha, R., Dommen, J., Gaeggeler, K., Weingartner, E., Samburova, V., Kalberer, M., and *Baltensperger U.*, 2006: On line gas and aerosol measurement of water soluble carboxylicacids in Zurich. *J. Geophys. Res. 111,* 12316. doi:10.1029/2005JD006782.

Gao, Y., Yu, L.E., and *Chen, S.B.*, 2008: Effects of organics on efflorescence relative humidity of ammonium sulfate or sodium chloride particles. *Atmos. Environ. 42,* 4433–4445

Hansson, H.C., Rood, M.J., Koloutsou-Vakakis, S., Hämeri, K., Orisini, D., and *Wiedensohler A.*, 1998: NaCl aerosol particle hygroscopicity dependence on mixing with organic compounds. *J. Atmos. Chem. 31,* 312–346.

Imre, K. and *Molnár, A.*, 2008: Hygroscopic behavior of Central European atmospheric background aerosol particles in summer. *Időjárás 112,* 63–82.

Kajino M., Winiwarter W., and *Ueda H.*, 2006: Modeling retained water content in measured aerosol mass. *Atmos. Environ. 40,* 5202–5213.

Khlystov, A., Stanier, C.O., Takahama, S. and *Pandis, S.*, 2005: Water content of ambient aerosol during the Pittsburgh Air Quality Study. *J. Geophys. Res. 110,* D07S10, doi:10.1029/2004JD004651.

Marcolli, C. and *Krieger, U.K.*, 2006: Phase changes during hygroscopic cycles of mixed organic/inorganic model systems of tropospheric aerosols. *J. Phys. Chem. A110,* 1881–1893

Ministry of Rural Development 4/2011. (2011). (I.14.) VM rendelet a levegőterheltségi szint határértékeiről és a helyhez kötött légszennyező pontforrások kibocsátási határértékeiről. (in Hungarian)

Onasch, T.B., Siefert, R.L., Brooks, S.D., Prenni, A., Murray, B., Wilson, M., and *Tolbert, M.A.*, 1999: Infrared spectroscopic study of the deliquescence and efflorescence of ammonium sulfate aerosol as a function of temperature. *J. Geophys. Res.104,* 21317–21326.

Randriamiarisoa, H., Chazette, P., Couvert, P., Sanak, J., and *Megie, G.*, 2006: Relative humidity

impact on aerosol parameters in a Paris suburban area. *Atmos. Chem. Phys.6,* 1389–1407.

Salminen, K. and *Karlsson, V.,* 2003: Comparability of low-volume PM_{10} sampler with β-attenuation monitor in background air. *Atmos. Environ. 37,* 3707–3712.

Santarpia, J.L., Li, R., and *Collins, D.R.,* 2004: Direct measurement of the hydration state of ambient aerosol populations. *J. Geophys. Res. 109,* D18209, doi:10.1029/2004JD004653.

Saxena, P., Hildemann, L.M., McMurry, P.H. and *Seinfeld, J.H.,* 1995: Organics alter hygroscopic behavior of atmospheric particles, *J. Geophys. Res. 100,* D9, 18755–18770.

Shin, S., Jung, C., and *Kim, Y.,* 2011: Analysis of the Measurement Difference for the PM_{10} Concentrations between Beta-ray Absorption and Gravimetric Methods at Gosan. *Aeros. Air Qual. Res. 11,* 846–853.

Sievering H., Boatman J., Galloway J., Keene W., Kim Y., Luria M., Ray J., 1991: Heterogeneous sulfur conversion in sea-salt aerosol particles: the role of aerosol water content and size distribution *Atmos. Environ. Part A. General Topics 25,* 1479–1487.

Strollo, C. and *Ziemann, P.,* 2013: Products and mechanism of secondary organic aerosol formation from the reaction of 3-methylfuran with OH radicals in the presence of NOx. *Atmos. Environ. 77,* 534–543.

Takahashi, K., Minoura, H., and *Sakamoto, K.,* 2008: Examination of discrepancies between beta-attenuation and gravimetric methods for the monitoring of particulate matter. *Atmos. Environ. 42,* 5232–5240.

Tsyro, G., 2005: To what extent can aerosol water explain the discrepancy between model calculated and gravimetric and PM2.5? *Atmos. Chem. Phys. 5,* 515–532.

Warneck, P., 2000: Chemistry of the natural atmosphere, Academic Press, USA.

Weingartner E., Baltensperger, U., and *Burtscher, H.,* 1995: Growth and structural changes of combustion aerosols at high relative humidity. *J. Aeros.Sci. 26,* 667–668.

Zardini, A.A., Sjogren, S., Marcolli, C., Krieger, U.K., Gysel, M., Weingartner, E., Baltensperger, U., and *Peter, T.,* 2008: A combined particle trap/HTDMA hygroscopicity study of mixed inorganic/organic aerosol particles. *Atmos. Chem. Phys. 8,* 5589–5601.

Zhou, J., Swietlicki, E., Martinsson, B.G., Frank, G., and *Karlsson, M.N.A.,* 2000: Hygroscopic properties of aerosol particles during the Holme Moss hill cap cloud experiment. *J.f Aeros. Sci. 11,* 299–300.

IDŐJÁRÁS

Quarterly Journal of the Hungarian Meteorological Service
Vol. 118, No. 3, July – September, 2014, pp. 217–241

Comparison of the BMA and EMOS statistical methods in calibrating temperature and wind speed forecast ensembles

Sándor Baran[1]*, **András Horányi**[2], and **Dóra Nemoda**[1]

[1]*Faculty of Informatics, University of Debrecen*
Kassai út 26, H-4028 Debrecen, Hungary

[2]*Hungarian Meteorological Service*
Kitaibel pál u. 1, H-1024 Budapest, Hungary

**Corresponding author E-mail: baran.sandor@inf.unideb.hu*

(Manuscript received in final form June 6, 2014)

Abstract—The evolution of the weather can be described by deterministic numerical weather forecasting models. Multiple runs of these models with different initial conditions and/or model physics result in forecast ensembles which are used for estimating the distribution of future atmospheric states. However, these ensembles are usually under-dispersive and uncalibrated, so post-processing is required. In the present work we compare different versions of Bayesian model averaging (BMA) and ensemble model output statistics (EMOS) post-processing methods in order to calibrate 2m temperature and 10m wind speed forecasts of the operational ALADIN limited area model ensemble prediction system of the Hungarian Meteorological Service. We show that compared to the raw ensemble, both post-processing methods improve the calibration of probabilistic and accuracy of point forecasts. In case of temperature, the BMA method with linear bias correction slightly outperforms the corresponding EMOS technique, while the EMOS model shows the best performance for calibrating ensemble forecasts of wind speed.

Key-words: Bayesian model averaging, ensemble model output statistics, ensemble calibration

1. Introduction

The evolution of the weather can be described by numerical weather prediction (NWP) models, which are capable to simulate the atmospheric motions taking into account the physical governing laws of the atmosphere and the connected spheres (typically sea or land surface). Without any doubts, these models

provide primary support for weather forecasting and decision making. As a matter of fact, the NWP models and consequently the weather forecasts cannot be fully precise, and on top of that, their accuracy might change with the meteorological situation as well (due to the chaotic character of the atmosphere, which manifests in being very sensitive to its initial conditions). Therefore, it is a relevant request from the users to provide uncertainty estimations attached to the weather forecasts. The information related to the intrinsic uncertainty of the weather situation and the model itself is very valuable additional information, which is generally provided by the use of ensemble technique. The ensemble method is based on the accounting of all uncertainties exist in the NWP modeling process and its expression in terms of forecast probabilities. In this process first, all the uncertainties (possible error sources) of the NWP model are listed and then these error sources are quantified. The quantified errors are used to determine such perturbations, which are used for the creation of the forecast ensemble. In practice, the ensemble method is realized by the exploitation of an ensemble prediction system (EPS). An EPS exploits several NWP model runs (and these ensemble model members differ within the known uncertainties of the initial and boundary conditions, model formulation, etc.) and then evaluates the ensemble of forecasts statistically. Ensemble prediction systems are widely used by the meteorological community especially for medium-range weather forecasts (*Buizza et al.,* 2005), and this tool is becoming more and more popular for short range (*Iversen et al.,* 2011) and even ultra-short range (*Bouallègue et al.,* 2013) weather prediction.

One possible improvement area of the ensemble forecasts is the calibration of the ensemble in order to transform the original ensemble member-based probability density function (PDF) into a more reliable and realistic one. The main disadvantage of the method is that it is based on statistics of model outputs, and therefore unable to consider the physical aspects of the underlying processes. The latter issues should be addressed by the improvements of the reality of the model descriptions and particularly the better uncertainty descriptions used by the different model realizations.

From the various modern post-processing techniques (for an overview see, e.g., *Williams et al.,* 2014), probably the most widely used methods are the Bayesian model averaging (BMA, see, e.g., *Raftery et al.,* 2005; *Sloughter et al.,* 2007, 2010; *Soltanzadeh et al.,* 2011) and the ensemble model output statistics (EMOS, see, e.g., *Gneiting et al.,* 2005*; Wilks* and *Hamil,* 2007; *Thorarinsdottir* and *Gneiting,* 2010) which are implemented in ensembleBMA (*Fraley et al.,* 2009, 2011) and ensembleMOS packages of R. Both approaches provide estimates of the densities of the predictable weather quantities and once a predictive density is given, a point forecast can be easily determined (e.g., mean or median value).

The BMA method for calibrating forecast ensembles was introduced by *Raftery et al.* (2005). The BMA predictive PDF of a future weather quantity is

the weighted sum of individual PDFs corresponding to the ensemble members. An individual PDF can be interpreted as the conditional PDF of the future weather quantity, provided that the considered forecast is the best one and the weights are based on the relative performance of the ensemble members during a given training period.

The EMOS approach, proposed by *Gneiting et al. (*2005), uses a single parametric distribution as a predictive PDF with parameters depending on the ensemble members.

In both post-processing techniques, the unknown parameters are estimated using forecasts and validating observations from a rolling training period, which allows automatic adjustments of the statistical model to any changes of the EPS system (for instance seasonal variations or EPS model updates). EMOS method is usually more parsimonious and computationally more effective than BMA, but shows less flexibility. E.g., in case of a weather quantity following normal or truncated normal distribution the EMOS predictive PDF is by definition unimodal, while BMA approach allows multimodality.

The aim of the present paper is to compare the performance of BMA and EMOS calibration on the ensemble forecasts of temperature and wind speed produced by the operational limited area model ensemble prediction system of the Hungarian Meteorological Service (HMS) called ALADIN-HUNEPS (*Hágel*, 2010; *Horányi et al.,* 2011).

2. ALADIN-HUNEPS ensemble

The ALADIN-HUNEPS system of the HMS covers a large part of continental Europe with a horizontal resolution of 12 km, and it is obtained with dynamical downscaling (by the ALADIN limited area model) of the global ARPEGE based PEARP system of Météo France (*Horányi et al.*, 2006; *Descamps et al.,* 2009). The ensemble consists of 11 members, 10 initialized from perturbed initial conditions and one control member from the unperturbed analysis, implying that the ensemble contains groups of exchangeable forecasts.

The initial perturbations for PEARP are generated with the combination of singular vector-based and EDA-based perturbations (*Labadie et al.*, 2012). The singular vectors are optimized for 7 subdomains and then combined into perturbations. The EDA perturbations are computed as differences between the EDA members and the EDA mean (there is a 6-member EDA system running in France). These two sets of perturbations are combined into 17 perturbations, which are added to and subtracted from the control initial condition. Random sets of physical parameterizations (there are 10 sets of different physical parameterization packages) are attributed to the forecasts run from the differently perturbed initial conditions. All these combinations result in a 35-member (one control without perturbation and 34 perturbed members) global ensemble. The

ALADIN-HUNEPS system simply takes into account (and dynamically downscales) the control and the first 10 members of the PEARP system. These members contain the first 5 global perturbations added to and subtracted from the control.

The database contains 11 member ensembles of 42-hour forecasts for 2-meter temperature (given in K) and 10-meter wind speed (given in m/s) for 10 major cities in Hungary (Miskolc, Szombathely, Győr, Budapest, Debrecen, Nyíregyháza, Nagykanizsa, Pécs, Kecskemét, Szeged) produced by the ALADIN-HUNEPS system of the HMS, together with the corresponding validating observations for the one-year period between April 1, 2012 and March 31, 2013. The forecasts are initialized at 18 UTC. The data set is fairly complete, since there are only six days when no forecasts are available. These dates were excluded from the analysis.

Fig. 1 shows the verification rank histograms of the ensemble forecasts of temperature and wind speed. These are the histograms of ranks of validating observations with respect to the corresponding ensemble forecasts computed from the ranks at all locations and over the whole verification period (see, e.g., *Wilks*, 2011, Section 8.7.2). Both histograms are far from the desired uniform distribution, as in many cases the ensemble members either underestimate or overestimate the validating observations. The ensemble ranges contain the observed temperature and wind speed only in 60.61% and 68.52% of the cases, respectively (while their nominal values equal 10/12, i.e., 83.33%). Hence, both ensembles are under-dispersive and, in this way, they are uncalibrated. This supports the need of statistical post-processing in order to improve the forecasted probability density functions.

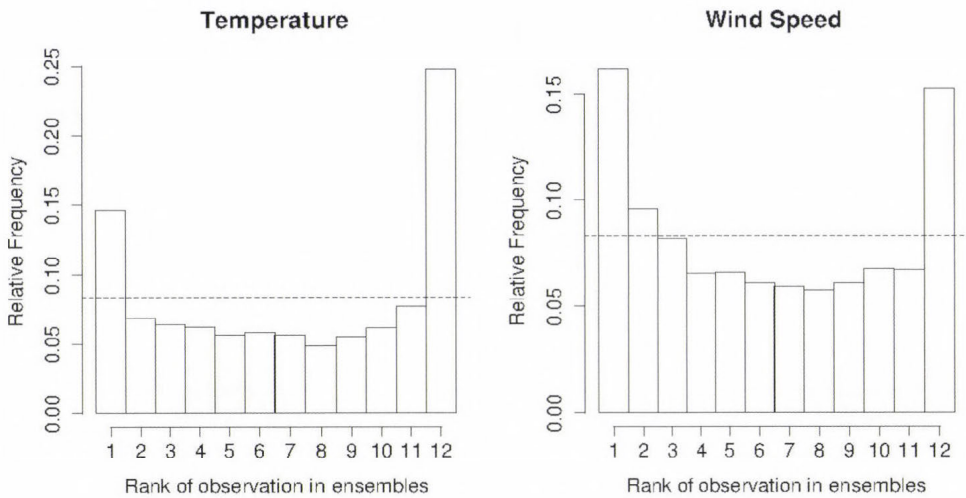

Fig. 1. Verification rank histograms of the 11-member ALADIN-HUNEPS ensemble forecasts of 2 m temperature and 10 m wind speed. Period: April 1, 2012 – March 31, 2013.

Note that BMA calibration of wind speed (*Baran et al.*, 2013; *Baran*, 2014) and temperature (*Baran et al.*, 2014) forecasts of the ALADIN-HUNEPS system have already been investigated by the authors using smaller data sets covering the period from October 1, 2010 to March 25, 2011. These investigations showed that significant improvements can be gained with the use of BMA post-processing. Nevertheless, it is interesting to see what enhancement can be obtained by BMA with respect to an improved raw EPS system and particularly in comparison to the EMOS calibration technique.

3. *Methods and verification scores*

As it has been mentioned in the Introduction, our study is concentrating on BMA and EMOS approaches. By $f_1, f_2, \ldots, f_M$ we denote the ensemble forecast of a certain weather quantity X for a given location and time. The ensemble members are either distinguishable (we can clearly identify each member or at least some of them) or indistinguishable (when the origin of the given member cannot be identified). Usually, the distinguishable EPS systems are the multi-model, multi-analyses ensemble systems, where each ensemble member can be identified and tracked. This property holds, e.g., for the University of Washington mesoscale ensemble (*Eckel* and *Mass,* 2005) or for the COSMO-DE ensemble of the German Meteorological Service (*Gebhardt et al.,* 2011).

However, most of the currently used ensemble prediction systems incorporate ensembles where at least some members are statistically indistinguishable. Such ensemble systems are usually producing initial conditions based on algorithms, which are able to find the fastest growing perturbations indicating the directions of the largest uncertainties (for instance, singular vector computations (*Buizza et al.*, 1993) or search for breeding vectors (*Toth* and *Kalnay*, 1997)). In most cases, these initial perturbations are further enriched by perturbations simulating model uncertainties as well. It is typically the case for the 51-member European Centre for Medium-Range Weather Forecasts ensemble (*Leutbecher* and *Palmer*, 2008) or for the PEARP and ALADIN-HUNEPS ensemble (*Hágel*, 2010; *Horányi et al.*, 2011) described in Section 2. In such cases, one usually has a control member (the one without any perturbation) and the remaining ensemble members are forming one or two exchangeable groups.

In what follows, if we have M ensemble members divided into m exchangeable groups, where the kth group contains $M_k > 1$ ensemble members ($\sum_{k=1}^{M} M_k = M$), notation $f_{k,\ell}$ is used for the ℓth member of the kth group.

3.1. Bayesian model averaging

In the BMA model proposed by *Raftery et al.* (2005), to each ensemble member f_k corresponds a component PDF $g_k(x|f_k, \theta_k)$, where θ_k is a parameter to be estimated. The BMA predictive PDF of X is

$$p(x|f_1, \dots, f_M) := \sum_{k=1}^{M} \omega_k g_k(x|f_k; \theta_k),$$

where the weight ω_k is connected to the relative performance of the ensemble member f_k during the training period. Obviously, these weights form a probability distribution, that is $\omega_k \geq 0, k = 1,2,..,M$, and $\sum_{k=1}^{M} \omega_k = 1$.

For the situation when M ensemble members are divided into m exchangeable groups, *Fraley et al.* (2010) suggested to use the following model

$$p(x|f_{1,1}, \dots, f_{1,M_1}, \dots, f_{m,1}, \dots, f_{m,M_m}) := \sum_{k=1}^{m} \sum_{\ell=1}^{M_k} \omega_k \, g_k(x|f_{k,\ell}; \theta_k), \quad (1)$$

where ensemble members within a given group have the same weights and parameters. Since this is the case for the ALADIN-HUNEPS ensemble (i.e., it consists of groups of exchangeable members), in what follows, we present only the weather variable specific versions of Eq. (1).

Temperature

For modeling temperature (and pressure) *Raftery et al.* (2005) and *Fraley et al.* (2010) use normal component PDFs, and Eq. (1) takes the form

$$p(x|f_{1,1}, \dots, f_{1,M_1}, \dots, f_{m,1}, \dots, f_{m,M_m}) := \sum_{k=1}^{m} \sum_{\ell=1}^{M_k} \omega_k \, g(x|f_{k,\ell}; \beta_{0,k}, \beta_{1,k}, \sigma^2), \quad (2)$$

where $g(x|f; \beta_0, \beta_1, \sigma^2)$ is a normal PDF with mean $\beta_0 + \beta_1 f$ (linear bias correction) and variance σ^2. Mean parameters $\beta_{0,k}$ and $\beta_{1,k}$ are usually estimated with linear regression of the validating observation on the corresponding ensemble members, while weights ω_k and variance σ^2, by maximum likelihood (ML) method using training data consisting of ensemble members and verifying observations from the preceding n days (training period). For example, taking $n = 30$, the predictive PDF, e.g., for 12 UTC March 31, 2013 at a given place can be obtained from the ensemble forecast for this particular day, time, and location (initialized at 18 UTC, March 29, 2013) with model parameters estimated from forecasts and verifying observations for all 10 locations from the period February 28 – March 29, 2013 (30 days, 300 forecast cases).

Another method for estimating model parameters is to minimize an appropriate verification score (see Section 3.3) using the same rolling training data as before.

As special cases of the model given by Eq. (2), one can also consider the situations when only additive bias correction present, that is $b_{1,k} = 1$, and when bias correction is not applied at all, i.e., $b_{0,k} = 0$ and $b_{1,k} = 1, k = 1,2, \dots, m$.

Wind speed

Since wind speed can take only non-negative values, for modeling this weather quantity a skewed distribution is required. A popular candidate is the Weibull distribution (see, e.g., *Justus et al.,* 1978), however, *Tuller* and *Brett* (1984) pointed out that the necessary conditions for fitting this distribution are not always met. *Sloughter et al.* (2010) proposes the BMA model

$$p(x|f_{1,1}, \dots, f_{1,M_1}, \dots, f_{m,1}, \dots, f_{m,M_m}) := \sum_{k=1}^{m} \sum_{\ell=1}^{M_k} \omega_k h(x|f_{k,\ell}; b_{0,k}, b_{1,k}, c_0, c_1), \quad (3)$$

for power transformations of the observed wind speed, where by $h(x|\mathrm{f}; b_0, b_1, c_0, c_1)$ we denote the PDF of gamma distribution with mean $b_0 + b_1 f$ and standard deviation $c_0 + c_1 f$. Parameters can be estimated in the same way as before, that is either mean parameters by regression and weights and standard deviation parameters by ML method or by minimizing a verification score. It is worth mentioning that in the ensembleBMA package of R, a more parsimonious model is implemented, where the mean parameters are constant across all ensemble members. In what follows, we will use this simplification, too. Further, preliminary studies (*Baran*, 2014) showed that for the ALADIN-HUNEPS ensemble, untransformed gamma BMA model gives the best fit, so no power transformations are needed.

As an alternative to the gamma BMA approach, *Baran* (2014) suggests to model wind speed with a mixture of truncated normal distributions with a cut-off at zero $\mathcal{N}^0(\mu, \sigma^2)$, where the location μ of a component PDF is an affine function of the corresponding ensemble member. The proposed BMA model is

$$p(x|f_{1,1}, \dots, f_{1,M_1}, \dots, f_{m,1}, \dots, f_{m,M_m}) := \sum_{k=1}^{m} \sum_{\ell=1}^{M_k} \omega_k q(x|f_{k,\ell}; \beta_{0,k}, \beta_{1,k}, \sigma^2), \quad (4)$$

where $q(x|\mathrm{f}; \beta_0, \beta_1, \sigma^2)$ is a truncated normal PDF with location $\beta_0 + \beta_1 f$ and scale σ^2, that is

$$q(x|\mathrm{f}; \beta_0, \beta_1, \sigma^2) := \frac{\frac{1}{\sigma}\varphi((x-\beta_0-\beta_1 f)/\sigma)}{\Phi((\beta_0+\beta_1 f)/\sigma)}, \text{ for } x \geq 0,$$

and 0, otherwise. Here φ and Φ denote the PDF and the cumulative distribution function (CDF) of the standard normal distribution, respectively.

For estimating parameters of the model specified by Eq. (4) *Baran* (2014) uses a full ML method, which means that all parameter estimates are obtained by maximizing the likelihood function corresponding to the training data.

3.2. Ensemble model output statistics

As noted, the EMOS predictive PDF is a single parametric density where the parameters are functions of the ensemble members.

Temperature

Similarly to the BMA approach, for modeling temperature (and pressure) normal distribution seems to be a reasonable choice. The EMOS predictive distribution suggested by *Gneiting et al.* (2005) is

$$\mathcal{N}(a_0 + a_1 f_1 + \cdots + a_M f_M, b_0 + b_1 S^2) \tag{5}$$

with $$S^2 := \frac{1}{M-1} \sum_{k=1}^{M} (f_k - \bar{f})^2,$$

where $\bar{f}$ denotes the ensemble mean. Location parameters $a_0 \in \mathbb{R}$, $a_1, \ldots, a_M \geq 0$ and scale parameters $b_0, b_1 \geq 0$ can be estimated from the training data by minimizing an appropriate verification score (see Section 3.3).

In the case when the ensemble can be divided into groups of exchangeable members, ensemble members within a given group get the same coefficient of the location parameter resulting in a predictive distribution of the form

$$\mathcal{N}(a_0 + a_1 \sum_{\ell_1=1}^{M_1} f_{1,\ell_1} + \cdots + a_m \sum_{\ell_m=1}^{M_m} f_{m,\ell_m}, b_0 + b_1 S^2), \tag{6}$$

where again, S^2 denotes the ensemble variance.

Wind speed

To take into account the non-negativity of the predictable quantity, in the EMOS model for wind speed proposed by *Thorarinsdottir and Gneiting* (2010), the normal predictive distribution of Eqs. (5) and (6) is replaced by a truncated normal distribution with cut-off at zero. This model is nearly as simple as the normal EMOS model for temperature, for exchangeable ensemble members the predictive distribution is

$$\mathcal{N}^0(a_0 + a_1 \sum_{\ell_1=1}^{M_1} f_{1,\ell_1} + \cdots + a_m \sum_{\ell_m=1}^{M_m} f_{m,\ell_m}, b_0 + b_1 S^2). \tag{7}$$

A summary of the above described models is given in *Table 1*, where the BMA component and EMOS predictive PDFs and their mean/location and

standard deviation/scale parameters are given as functions of the ensemble members f_ℓ and ensemble variance S^2.

Table 1. Summary of post-processing methods for temperature and wind speed forecasts. BMA component and EMOS predictive PDFs and their mean/location and standard deviation/scale parameters as functions of the ensemble members f_ℓ and ensemble variance S^2

		Predictive PDF	**Mean/location**	**Std. dev./scale**
Temperature	BMA	Normal mixture	$\beta_{0,k} + \beta_{1,k} f_k$	σ
	EMOS	Normal	$a_0 + \sum_{\ell=1}^{M} a_\ell f_\ell$	$\sqrt{b_0 + b_1 S^2}$
	BMA	Gamma mixture	$b_0 + b_1 f_k$	$c_0 + c_1 f_k$
Wind speed	BMA	Truncated normal mixture	$\beta_{0,k} + \beta_{1,k} f_k$	σ
	EMOS	Truncated normal	$a_0 + \sum_{\ell=1}^{M} a_\ell f_\ell$	$\sqrt{b_0 + b_1 S^2}$

3.3. Verification scores

In order to check the overall performance of the calibrated forecasts in terms of probability distribution function, the mean continuous ranked probability scores (CRPS; *Wilks*, 2011; *Gneiting* and *Raftery*, 2007) and the coverage and average width of 83.33% central prediction intervals are computed and compared for the calibrated and raw ensemble. Additionally, the ensemble mean and median are used to consider point forecasts, which are evaluated with the use of mean absolute errors (MAE) and root mean square errors (RMSE). We remark that for MAE and RMSE, the optimal point forecasts are the median and the mean, respectively (*Gneiting*, 2011; *Pinson* and *Hagedorn*, 2012). Further, given a CDF $F(y)$ and a real number x, the CRPS is defined as

$$crps(F, x) := \int_{-\infty}^{\infty} \left(F(y) - \chi_{\{y \geq x\}}\right)^2 dy,$$

where χ_H denotes the indicator of a set H. The mean CRPS of a probability forecast is the average of the CRPS values of the predictive CDFs and corresponding validating observations taken over all locations and time points considered resulting in a value in the units of the forecast variable. For the raw ensemble, the empirical CDF of the ensemble replaces the predictive CDF. Note that CRPS, MAE, and RMSE are negatively oriented scores, that is the smaller the better. Finally, the coverage of a $(1-\alpha)100\%$, $\alpha \in (0,1)$, central prediction interval is the proportion of validating observations located between the lower

and upper $\alpha/2$ quantiles of the predictive distribution. For a calibrated predictive PDF, this value should be around $(1-\alpha)100\%$.

4. *Results*

Using the ideas of *Baran et al.* (2013, 2014), we consider two different groupings of the members of the ALADIN-HUNEPS ensemble. In the first case we have two exchangeable groups ($m = 2$). One contains the control member denoted by f_c ($M_1 = 1$), while in the other are 10 ensemble members ($M_2 = 10$) corresponding to the differently perturbed initial conditions denoted by $f_{p,1}, \ldots, f_{p,10}$. Under these conditions, for temperature data we investigate the BMA model specified by Eq. (2) with three different bias correction methods (linear, additive, no bias correction) and the EMOS model given by Eq. (6), while for wind speed data the BMA models defined by Eqs. (3) and (4) and the EMOS model specified by Eq. (7) are studied. In this two-group situation we have only one independent BMA weight $\omega \in [0,1]$ corresponding, e.g., to the control, that is $\omega_1 = \omega$ and $\omega_2 = (1-\omega)/10$.

In the second case, the odd and even numbered exchangeable ensemble members form two separate groups $\{f_{p,1}, f_{p,3}, f_{p,5}, f_{p,7}, f_{p,9}\}$ and $\{f_{p,2}, f_{p,4}, f_{p,6}, f_{p,8}, f_{p,10}\}$, respectively ($m = 3$, $M_1 = 1$, $M_2 = M_3 = 5$), which idea is justified by the method their initial conditions are generated. For more details see Section 2, particularly the fact that only five perturbations are calculated and then they are added to (odd numbered members) and subtracted from (even numbered members) the unperturbed initial conditions. For calibrating ensemble forecasts of temperature and wind speed, we use the three-group versions of BMA and EMOS models considered earlier in the two-group case.

As typical example for illustrating the two different post-processing methods and groupings, we consider temperature data and forecasts for Debrecen valid on July 2, 2012. *Figs. 2a* and *2b* show the BMA predictive PDFs in the two- and three-group cases, the component PDFs corresponding to different groups, the median forecasts, the verifying observations, the first and last deciles, and the ensemble members. Besides the EMOS predictive PDFs the same quantities can be seen in *Figs. 2c* and *2d*, too. On the considered date the spread of the ensemble is reasonable (the ensemble range equals 2.368 K), but all ensemble members overestimate the validating observation (306.45 K). Obviously, the same holds for the ensemble median (308.927 K), while BMA median forecasts corresponding to the two- and three-group models (both equal to 306.524 K) are quite close to the true temperature. The point forecasts produced by the EMOS model are slightly worse (306.921 K for both groupings) but still outperform the ensemble median.

We start our data analysis by determining the optimal lengths of the training periods to be used for estimating the parameters of BMA and EMOS predictive distributions for 2m temperature and 10m wind speed. After finding them we compare the performances of BMA and EMOS post-processed forecasts using these optimal training period lengths. For EMOS models, the parameter estimates are obtained by minimizing the CRPS values of the predictive PDFs.

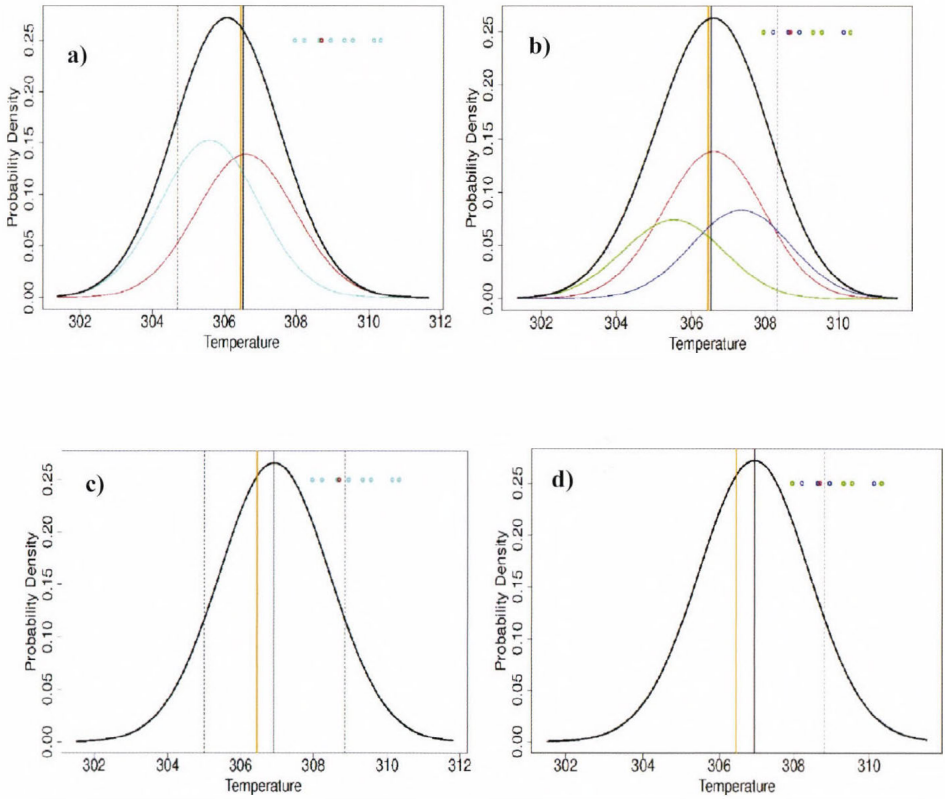

Fig. 2. (a) and *(b):* BMA; *(c)* and *(d):* EMOS density forecasts for 2m temperature (given in K) for Debrecen valid on July 2, 2012. BMA PDFs with linear bias correction in two- and three-group cases (overall: thick black line; control: red line; sum of exchangeable members on (a): light blue line; on (b): green (odd members) and blue (even members) lines), EMOS predictive PDFs in two- and three-group cases (thick black line), ensemble members (circles with the same colours as the corresponding BMA PDFs), BMA/EMOS median forecasts (vertical black line), verifying observations (vertical orange line) and the first and last deciles (vertical dashed lines).

4.1. Training period

Similarly to our previous studies (*Baran et al.*, 2013, 2014), we proceed in the same way as *Raftery et al.* (2005) and determine the length of training period to be used for BMA and EMOS calibrations by comparing MAE values of median forecasts, RMSE values of mean forecasts, CRPS values of predictive distributions, and coverages and average widths of 83.33% central prediction intervals calculated from the predictive PDFs using training periods of length of $10,11,\ldots,60$ calendar days. In order to ensure the comparability of the verification scores corresponding to different training period lengths, we issue calibrated forecasts of temperature and wind speed for the period from June 1, 2012 to March 31, 2013 (6 days with missing data are excluded). This means 298 calendar days following the first training period of maximal length of 60 days.

Temperature

For temperature data we consider BMA predictive PDF given by Eq. (2) with linear bias correction and EMOS model Eq. (6) with parameters minimizing the CRPS of probabilistic forecasts corresponding to the training data. In order to ensure a more direct comparison of the two models, we also investigated the performance of the BMA predictive PDF specified by Eq. (2) with parameter estimates minimizing the same verification score. It yielded sharper central prediction intervals and lower coverage for all training period lengths considered, but there were no significant differences in CRPS, MAE, and RMSE values corresponding to different parameter estimation methods.

Consider first the two-group situation. In *Fig. 3* the CRPS values of BMA and EMOS predictive distributions, MAE values of median, and RMSE values of mean forecasts are plotted against the length of the training period. Note that for normal EMOS model, mean and median forecasts are obviously coincide. First of all it is noticeable that the results are very consistent for all diagnostics, i.e., the curves are similar for all measures. EMOS produces better verification scores, and after 32 days there is no big difference among scores obtained with different training period lengths. In case of the BMA model, CRPS, MAE, and RMSE reach their minima at day 35, and this training period length gives the minima of CRPS and RMSE of the EMOS model, too (see *Table* 2). Although the minimum of MAE of the EMOS model is reached at day 42, the value at day 35 is very near to this minimum as well.

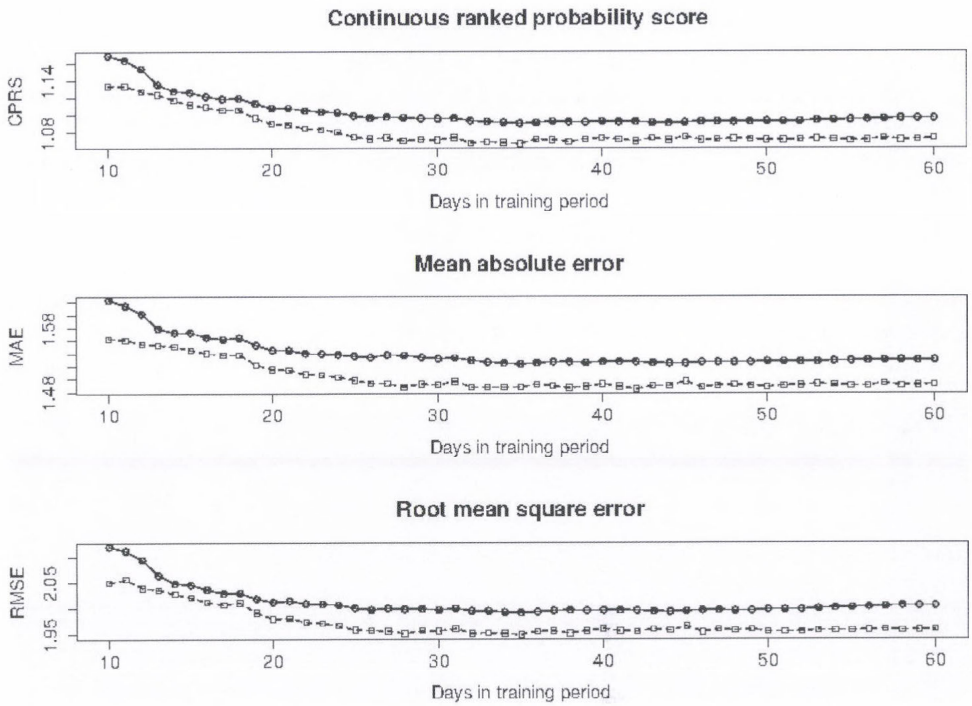

Fig. 3. Mean CRPS of predictive distributions, MAE of BMA/EMOS median, and RMSE of BMA/EMOS mean forecasts for temperature (given in K) corresponding to two-group models for various training period lengths (BMA: solid and ○; EMOS: dashed and □).

Table 2. Optimal training period lengths for temperature with respect to mean CRPS, MAE, and RMSE (given in K), the corresponding optimal scores, and scores at the chosen 35 days length.

		Mean CRPS			MAE			RMSE		
		opt. day	**opt. value**	**day 35 value**	**opt. day**	**opt. value**	**day 35 value**	**opt. day**	**opt. value**	**day 35 value**
Two groups	BMA	35	1.0901	1.0901	35	1.5230	1.5230	35	1.9914	1.9914
	EMOS	35	1.0671	1.0671	42	1.4843	1.4868	35	1.9494	1.9494
Three groups	BMA	35	1.0896	1.0896	35	1.5227	1.5227	36	1.9897	1.9899
	EMOS	26	1.0703	1.0718	26	1.4843	1.4895	28	1.9529	1.9570

Fig. 4 shows the average width and the coverage of the 83.33% central prediction interval for both models considered. Similarly to the previous diagnostics, after 32 days all curves are rather flat showing only a slightly increasing trend. EMOS model yields significantly sharper central prediction intervals for all training period lengths considered, but its coverage stays below the nominal value of 83.33% (dashed line). Unfortunately, the coverage of the BMA model also fails to reach the nominal value, but it is very close to 83.33% from day 35 onwards. The maximal coverage is attained at day 37. Comparing the average width and coverage, one can observe that they have opposite behavior, i.e., the average width values favor shorter training periods, while the coverage figures prefer longer ones. On the other hand, the trend of the average width values is rather flat after day 30 (or so). In any case, a reasonable compromise ought to be found, which is at the range of 30 – 40 days.

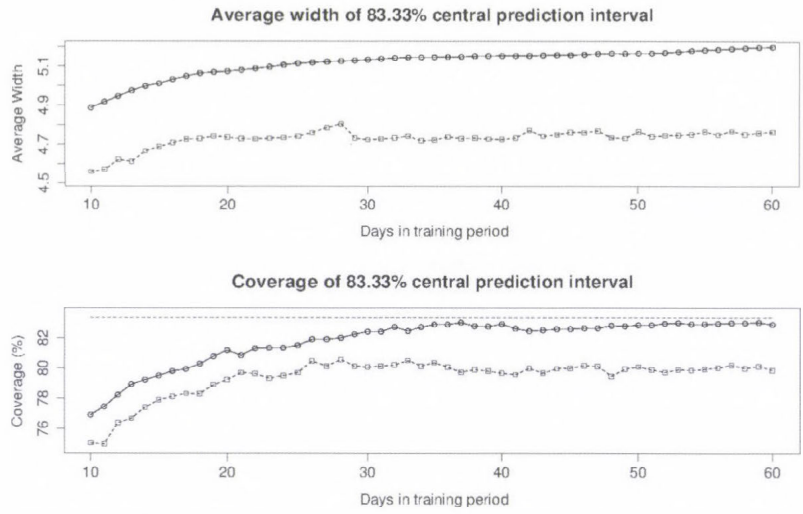

Fig. 4. Average width (given in K) and coverage of 83.33% BMA/EMOS central prediction intervals for temperature corresponding to two-group models for various training period lengths (BMA: solid and ○; EMOS: dashed and □).

As a summary, it can be said that a 35-day training period seems to be an acceptable choice both for the BMA and EMOS models (particularly see conclusions based on *Fig. 3*, which are not compromised by the other two diagnostics at *Fig. 4*).

Very similar conclusions can be drawn for the three-group models. The overall behaviors of the two post-processing methods for the various diagnostics (not shown) are very similar to those of their two-group counterparts. EMOS

model provides lower CRPS, MAE, and RMSE values and, moreover, the lower coverage combined with sharper central prediction interval all over the time periods. In terms of specific values, the minima of CRPS and MAE for the BMA model are reached again at day 35, while the RMSE takes its minimum at day 36 (the value at day 35 is very near to this minimum, see *Table 2*). For the EMOS model, CRPS, MAE, and RMSE reach their minima in the range of 26–28 days, and values at day 35 are again very close to these minima.

Regarding the average width, shorter training periods yield sharper central prediction intervals. The coverage for the EMOS model is always below the nominal value, while the maximal coverage of the BMA model is reached at day 59. However, as in general shorter training periods are preferred, a reasonable compromise is to consider the 35–38-day interval where the BMA coverage is also very high. Hence, the training period proposed for the two-group model can be kept for the three-group model as well, therefore, for temperature we suggest the use of a training period of length 35 days for all the investigated post-processing methods.

Wind speed

To calibrate ensemble forecasts of wind speed, we apply gamma and truncated normal BMA models given by Eqs. (3) and (4), respectively, and EMOS model specified by Eq. (7). In the latter case, similarly to EMOS calibration of temperature forecasts, estimation of parameters is done by minimizing the CRPS of probabilistic forecasts corresponding to the training data.

First, consider again the case when we have two groups of exchangeable ensemble members. Generally, the various scores have rather flat evolution with respect to the training lengths (see *Fig. 5* and *Fig. 6*). It is particularly true after day 25, which would suggest that basically any training length longer than 25 days might be an acceptable choice. Observe that the order of different methods with respect to a given score remains the same for all training period lengths. Truncated normal BMA produces the lowest CRPS values, while the best MAE and RMSE values correspond to EMOS post-processing. In any case if we wanted to pick up a single training period length as an optimal one, 43 days would be a reasonable choice. This is the value where the minima of CRPS of all three methods and the minimum of RMSE of gamma BMA are reached (see *Table 3*). The MAE values of the truncated normal BMA and EMOS models attain their minima at day 59, however, values corresponding to day 43 are practically the same. Finally, the minima of the MAE of the gamma BMA model and the RMSE of the truncated normal BMA and EMOS models are reached at days 47, 41, and 29, respectively, while in all three cases the values at day 43 are the second smallest ones.

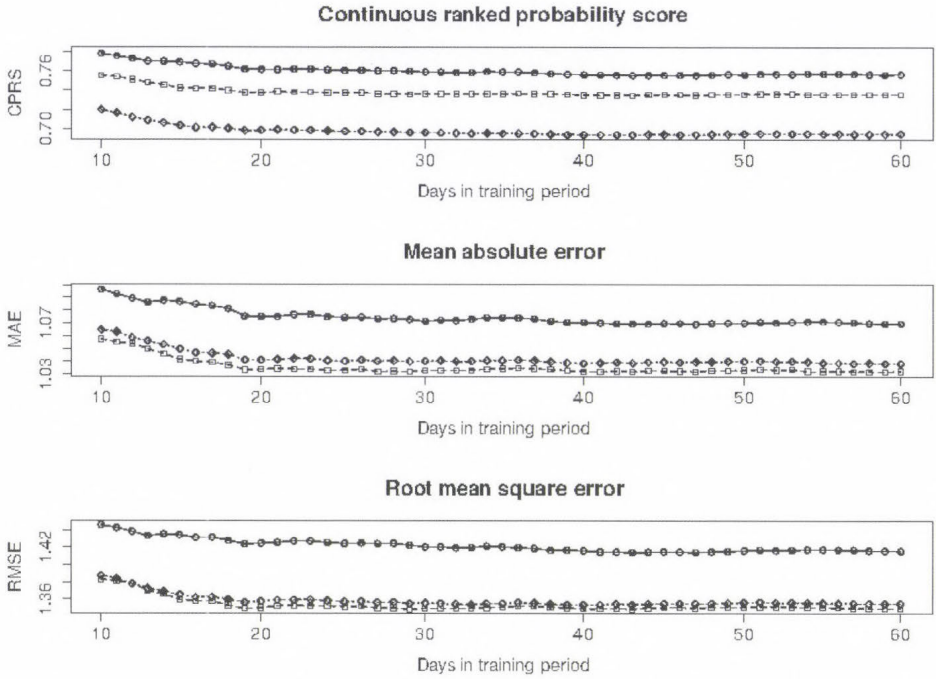

Fig. 5. Mean CRPS of predictive distributions, MAE of BMA/EMOS median and RMSE of BMA/EMOS mean forecasts for wind speed (given in m/s) corresponding to two-group models for various training period lengths (Gamma BMA: solid and ○; truncated normal BMA: dotted and ◊; EMOS: dashed and □).

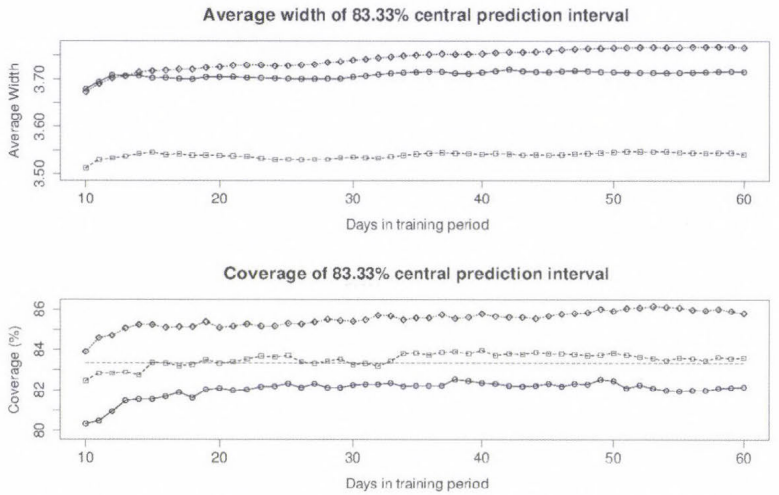

Fig. 6. Average width (given in m/s) and coverage of 83.33% BMA/EMOS central prediction intervals for wind speed corresponding to two-group models for various training period lengths (Gamma BMA: solid and ○; truncated normal BMA: dotted and ◊; EMOS: dashed and □).

EMOS post-processing yields the sharpest central prediction intervals and coverage values which are very close to the nominal level for all considered training period lengths (*Fig. 6*). The 83.33% central prediction intervals for the truncated normal BMA model are significantly wider than those of the EMOS together with a coverage varying between 83.89% and 86.14%. Gamma BMA results in narrower central prediction intervals, but its coverage never reaches the nominal level. The maximal coverage is attained at days 38 and 49. In this way, a 43-day training period length is also acceptable from the point of view of central prediction intervals.

The analysis of verification scores corresponding to the alternative grouping of ensemble members (not shown) leads again to very similar results. The most important difference between the two-group and three-group models is that forming three groups (especially for training periods longer than 20 days) improves MAE and RMSE values of the truncated normal BMA model, and they become very close to the corresponding values of EMOS. For the three-group EMOS model, CRPS and RMSE reach their minima at day 43, and this is the training period length where the minimal CRPS and the second smallest values of MAE and RMSE of the gamma BMA model are attained (see *Table 3*). For the latter model, the global minima of MAE and RMSE are at day 42. In case of truncated normal BMA, post-processing, CRPS, MAE, and RMSE have their minima at day 39, but since these curves are rather flat, values corresponding to a training period of length 43 days are very near. In this way, a 43-day training period seems to be acceptable for both groupings of ensemble members.

Table 3. Optimal training period lengths for wind speed with respect to mean CRPS, MAE and RMSE (given in m/s), the corresponding optimal scores, and scores at the chosen 43-day length.

		Mean CRPS			MAE			RMSE		
		opt. day	**opt. value**	**day 43 value**	**opt. day**	**opt. value**	**day 43 value**	**opt. day**	**opt. value**	**day 43 value**
Two	BMA, g.	43	0.7551	0.7551	47	1.0692	1.0694	43	1.4145	1.4145
groups	BMA, tr.	43	0.6933	0.6933	59	1.0385	1.0389	41	1.3536	1.3540
	EMOS	43	0.7346	0.7346	59	1.0320	1.0322	29	1.3488	1.3491
Three	BMA, g.	43	0.7559	0.7559	42	1.0690	1.0691	42	1.3940	1.3941
groups	BMA, tr.	39	0.6930	0.6930	39	1.0377	1.0382	39	1.3535	1.3543
	EMOS	43	0.7355	0.7355	28	1.0326	1.0328	43	1.3504	1.3504

4.2. Ensemble calibration using BMA and EMOS post-processing

According to the results of the previous section, to compare the performance of BMA and EMOS post-processing on the 11-member ALADIN-HUNEPS ensemble, we use rolling training periods of lengths 35 days for temperature and 43 days for wind speed.

Temperature

For post-processing ensemble forecasts of temperature, we consider the BMA model defined by Eq. (2) with all three bias correction methods introduced in Section 3.1 (linear, additive, none) and EMOS model minimizing the CRPS of probabilistic forecasts corresponding to the training data. The application of three different BMA bias correction methods is justified by a previous study dealing with statistical calibration of the ALADIN-HUNEPS temperature forecasts (*Baran et al.*, 2014), where the simplest BMA model without bias correction showed the best overall performance (although that study was using different ALADIN-HUNEPS dataset period, which preceded the one investigated in this article).

The use of a 35-day rolling training period implies that ensemble members, validating observations, and predictive PDFs are available for the period from May 7, 2012 to March 31, 2013 (having 323 calendar days just after the first 35-day training period). This time interval starts nearly 4 weeks earlier than the one used for determination of the optimal training period length.

The first step in checking the calibration of our post-processed forecasts is to have a look at their probability integral transform (PIT) histograms. The PIT is the value of the predictive CDF evaluated at the verifying observations (*Raftery et al.*, 2005), which provides a good and easily interpretable measure about the possible improvements of the under-dispersive character of the raw ensemble. The closer the histogram to the uniform distribution, the better the calibration. In *Fig. 7,* PIT histograms corresponding to all three versions of the BMA model and to the EMOS model are displayed both in the two- and three-group cases. A comparison to the verification rank histogram of the raw ensemble (see *Fig. 1*) shows that at every case, post-processing significantly improves the statistical calibration of the forecasts. However, the BMA model without bias correction now becomes over-dispersive and the PIT values of the EMOS are slightly better, while at the same time, for the BMA models with linear and additive bias correction, one can accept uniformity. This visual perception is confirmed by the p-values of Kolmogorov-Smirnov tests for uniformity of the PIT values (see *Table 4*). Therefore, the BMA model with additive bias correction produces the best PIT histograms (the linear bias correction case is just slightly worse), the performance of the EMOS model is also quite good, while the fit of the BMA model without bias correction is rather

poor. One can additionally observe that the three-group models systematically outperform the two-group ones.

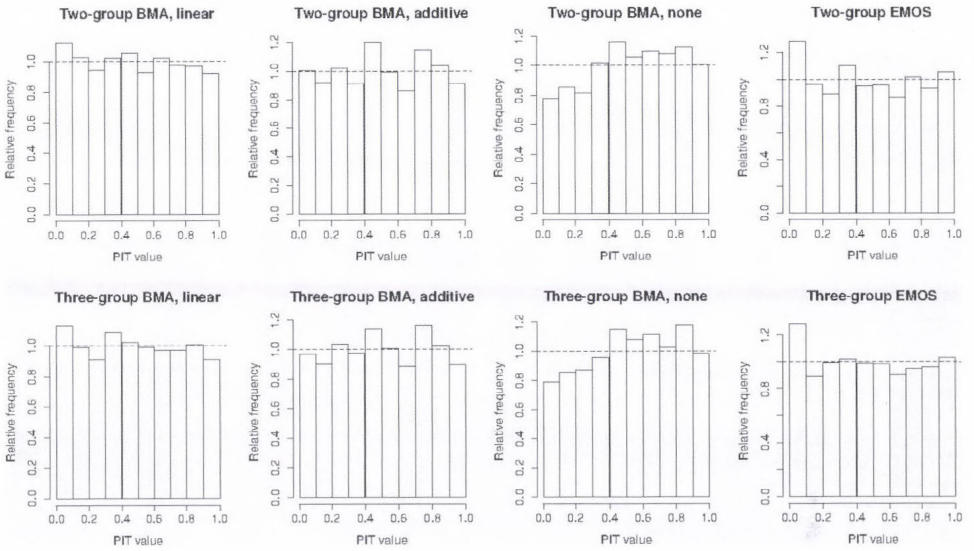

Fig. 7. PIT histograms for BMA and EMOS post-processed forecasts of temperature using two- and three-group models.

Table 4. p-values of Kolmogorov-Smirnov tests for uniformity of PIT values corresponding to predictive distributions of temperature

	BMA model with bias correction			EMOS model
	linear	additive	none	
Two groups	0.1393	0.2405	2.2×10^{-10}	0.0062
Three groups	0.2281	0.4617	4.1×10^{-9}	0.0093

In *Table 5*, verification measures of probabilistic and point forecasts calculated using BMA and EMOS models are given together with the corresponding scores of the raw ensemble. By examining these results, one can clearly observe again the obvious advantage of post-processing with respect to the raw ensemble. This is quantified in decrease of CRPS, MAE, and RMSE values and in a significant increase in the coverage of the 83.33% central

prediction intervals. On the other hand, the post-processed forecasts are less sharp (e.g., 83.33% central prediction intervals are around 30% – 40% wider than the raw ensemble range). This fact is coming from the small dispersion of the raw ensemble, as also seen in the verification rank histogram of *Fig. 1*. Furthermore, BMA and EMOS models distinguishing three exchangeable groups of ensemble members slightly outperform their two-group counterparts (in agreement with the interpretations based on the PIT histograms). Comparing the different post-processing methods, it is noticeable that on the one hand, EMOS produces the lowest CRPS, MAE, and RMSE values and sharpest central prediction intervals both in the two- and three-group cases, although with coverages far below the targeted 83.33%. On the other hand, in terms of CRPS, MAE, and RMSE, the behavior of the BMA model with linear bias correction is just slightly worse, and at the same time this method produces the best approximation of the nominal coverage. Taking also into account the fit of the PIT values to the uniform distribution (see *Fig. 7* and *Table 4* again), one can conclude that overall from the four competing post-processing methods, the BMA model with linear bias correction shows the best performance. These results are not in contradiction with the ones for a previous period (see *Baran et al.* (2014), where the no bias correction case proved to be the optimal), since the characteristics of the raw ALADIN-HUNEPS system had been slightly changed in between. The coverage of the system had been significantly improved (from 46% to 60%), although the latest system became slightly biased (as compared to the previously examined one). Therefore, due to the existence of the bias, it is not surprising that one of the versions with bias correction has the best behavior.

Table 5. Mean CRPS of probabilistic, MAE, and RMSE of median/mean forecasts, average width, and coverage of 83.33% central prediction intervals for temperature (given in K)

		Mean CRPS	MAE		RMSE		Average widths	Coverage (%)
			median	mean	median	mean		
Two groups	BMA, lin.	1.0815	1.5101	1.5097	1.9789	1.9765	5.1375	83.00
	BMA, add.	1.1029	1.5395	1.5329	2.0028	1.9871	5.5146	84.21
	BMA none	1.1131	1.5536	1.5444	2.0167	2.0014	5.7191	84.80
	EMOS	1.0586	1.4731	1.4731	1.9348	1.9348	4.7203	80.43
Three groups	BMA, lin.	1.0801	1.5082	1.5059	1.9767	1.9726	5.1369	83.28
	BMA, add.	1.0998	1.5346	1.5254	1.9962	1.9783	5.5096	84.12
	BMA none	1.1123	1.5509	1.5407	2.0156	1.9988	5.7095	85.11
	EMOS	1.0591	1.4689	1.4689	1.9308	1.9308	4.7523	80.53
Raw ensemble		1.2284	1.5674	1.5512	2.0434	2.0131	3.9822	60.53

Wind speed

According to results of Section 4.1, to compare the predictive performances of gamma BMA (Eq. (3)), truncated normal BMA (Eq. (4)) and EMOS (Eq. (7)) post-processing on the 11-member ALADIN-HUNEPS ensemble forecast of wind speed, we use a training period of length 43 calendar days. In this way, ensemble members, validating observations, and predictive distributions are available for the period from May 15, 2012 to March 31, 2013 (313 calendar days).

First, consider again the PIT histograms of various calibration methods, which are displayed in *Fig. 8*. Compared to the verification rank histogram of the wind speed ensemble (see *Fig. 1*), the statistical post-processing induced improvements are obvious, however, e.g., in case of truncated normal BMA, both corresponding PIT histograms are slightly over-dispersive. The p-values of Kolmogorov-Smirnov tests given in *Table 6* also show that truncated normal BMA models produce the poorest fit, while for gamma BMA and EMOS models one can accept uniformity. In case of BMA calibration, the three-group models again outperform the two-group ones, while for EMOS the situation is the reverse. A similar behavior can be observed in *Table 7*, where the verification scores of probabilistic and point forecasts calculated using BMA and EMOS post-processing and the corresponding measures of the raw ensemble are given. Considering first the probabilistic forecasts (in terms of CRPS, average width of central prediction interval, and coverage), one can observe that the calibrated forecasts are smaller in CRPS, wider in central prediction intervals, and higher in coverage compared to the raw ensemble. Equally, to the two- and in three-group cases the smallest CRPS values belong to the truncated normal BMA model, while EMOS post-processing produces the sharpest central prediction intervals and the best approximation of the nominal coverage of 83.33%. Regarding the point forecasts (median and mean) calculated from the truncated normal BMA and EMOS predictive PDFs, generally there are smaller MAE and RMSE values than those of the raw ensemble. However, there is an exception for the gamma BMA model, since these scores are higher indicating degradations. A possible explanation might be related to the fact that in the investigated period (May 15, 2012 – March 31, 2013) both the raw ensemble median and the ensemble mean slightly overestimate the validating observations (their average biases (standard errors) are 0.0907 (0.0249) and 0.0972 (0.0244), respectively). Therefore, the small bias should be removed by relevant bias corrections. On the other hand, we believe that the simplest bias correction procedure of the gamma BMA model cannot eliminate these inaccuracies, moreover, it might introduce some additional errors. It is a matter of fact that in the two-group case, the average biases of the median and mean of the gamma BMA predictive PDF are -0.1935 and -0.1318 with standard errors of 0.0250 and 0.0253, respectively, while for the EMOS model showing the lowest MAE and RMSE values, these biases are only -0.0735 and

−0.0293, both having a standard error of 0.0242. Therefore, the EMOS model is able to compensate for the existing biases, which is also the case for the truncated normal BMA case, but not for the gamma BMA calibration. The difference in behavior between the two BMA calibration methods is attributed to the more sophisticated bias correction algorithm, which is applied for the truncated normal BMA case.

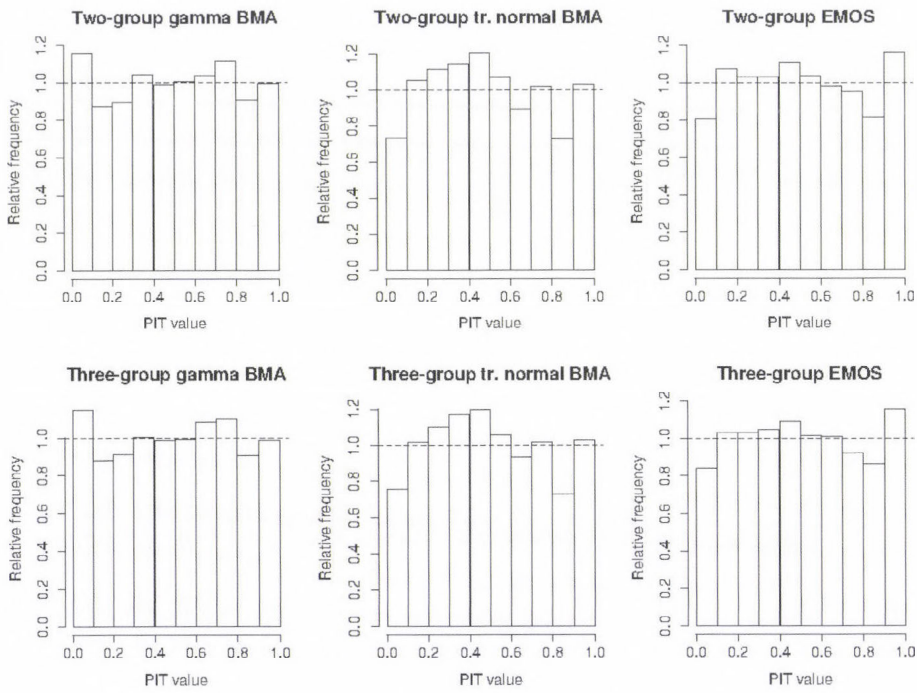

Fig. 8. PIT histograms for BMA and EMOS post-processed forecasts of wind speed using two- and three-group models.

Table 6. p-values of Kolmogorov-Smirnov tests for uniformity of PIT values corresponding to predictive distributions of wind speed.

	BMA model with bias correction		**EMOS model**
	gamma	**tr. normal**	
Two groups	0.1812	0.0023	0.1272
Three groups	0.2085	0.0043	0.0967

Table 7. Mean CRPS of probabilistic, MAE, and RMSE of median/mean forecasts, average width, and coverage of 83.33% central prediction intervals for wind speed (given in m/s).

		Mean CRPS	MAE		RMSE		Average widths	Coverage (%)
			median	mean	median	mean		
Two groups	BMA, gamma	0.7601	1.0747	1.0895	1.4176	1.4267	3.7151	81.87
	BMA, tr. n.	0.6982	1.0446	1.0471	1.3693	1.3632	3.7621	85.46
	EMOS	0.7381	1.0369	1.0375	1.3593	1.3572	3.5340	83.59
Three groups	BMA, gamma	0.7612	1.0754	1.0828	1.4192	1.4052	3.7064	82.03
	BMA tr. n.	0.6980	1.0437	1.0460	1.3696	1.3639	3.7498	85.08
	EMOS	0.7349	1.0381	1.0388	1.3620	1.3597	3.5219	83.11
Raw ensemble		0.8029	1.0688	1.0549	1.3980	1.3728	2.8842	68.22

To summarize, gamma BMA model outperforms the other two methods in terms of fit of PIT values, but it has the highest CRPS and very poor verification scores for the point forecasts. MAE and RMSE values corresponding to EMOS and truncated normal BMA are lower than those of the raw ensemble and rather similar to each other. From these two methods, truncated normal BMA produces much lower CRPS, while EMOS post-processing results in sharper central prediction intervals, better coverage, and better fit of PIT values to the uniform distribution, so we conclude that the overall performance of this method is the best for the calibration of the wind speed raw ensemble forecasts.

5. Discussion and conclusions

In this paper we have compared different versions of the BMA and EMOS statistical post-processing methods in order to improve the calibration of 2 m temperature and 10 m wind speed forecasts of the ALADIN-HUNEPS system. First, we have demonstrated the weaknesses of the ALADIN-HUNEPS raw ensemble system being under-dispersive and therefore uncalibrated. We have indicated that the under-dispersive character of the ALADIN-HUNEPS system had been improved compared to studies based on a former dataset, however, more enhancements are still needed. On the other hand, the latest dataset shows some features of bias of ALADIN-HUNEPS, which were not observed in the earlier studies. This fact has an influence on the optimal choice of statistical calibration, since the use of bias correction is getting more essential. Some standard measures were applied, which are related to the characteristics of the ensemble probability density functions and also the point forecasts as described by the mean/median of the ensemble. The various systems improve different aspects of the ensemble, however, overall both the BMA and the EMOS method

are capable to deliver significant improvements on the raw ALADIN-HUNEPS ensemble forecasts (for temperature and wind speed as well). In case of temperature, the best BMA method slightly outperforms the EMOS technique (although it should not be forgotten that, for instance, in terms of point forecasts, EMOS is better than BMA), while for calibrating ensemble forecasts of wind speed, the EMOS model shows the best performance.

Acknowledgments–Research was supported by the Hungarian Scientific Research Fund under Grant No. OTKA NK101680 and by the TÁMOP-4.2.2.C-11/1/KONV-2012-0001 project. The project has been supported by the European Union, co-financed by the European Social Fund. Essential part of this work was made during the visiting professorship of the first author at the Institute of Applied Mathematics of the University of Heidelberg. The authors are indebted to Tilmann Gneiting for his useful suggestions and remarks, to Thordis Thorarinsdottir for the R codes of EMOS for wind speed, and to *Mihály Szűcs* from the HMS for providing the data. Last but not least, the authors are very grateful to the Reviewers for their valuable comments.

References

Baran, S., 2014: Probabilistic wind speed forecasting using Bayesian model averaging with truncated normal components. *Comput. Stat. Data. Anal. 75*, 227–238.

Baran, S., Horányi, A. and *Nemoda, D.*, 2013: Statistical post-processing of probabilistic wind speed forecasting in Hungary. *Meteorol. Z. 22*, 273–282.

Baran, S., Horányi, A. and *Nemoda, D.*, 2014: Probabilistic temperature forecasting with statistical calibration in Hungary. *Meteorol. Atmos. Phys. 124*, 129–142.

Bouallégue, B.Z., Theis, S. and *Gebhardt, C.*, 2013: Enhancing COSMO-DE ensemble forecasts by inexpensive techniques. *Meteorol. Z. 22*, 49–59.

Buizza, R., Houtekamer, P.L., Toth, Z., Pellerin, G., Wei, M., and *Zhu, Y.*, 2005: A comparison of the ECMWF, MSC, and NCEP global ensemble prediction systems. *Mon. Wea. Rev. 133*, 1076–1097.

Buizza, R., Tribbia, J., Molteni, F. and Palmer, T., 1993: Computation of optimal unstable structures for a numerical weather prediction system. *Tellus A 45*, 388–407.

Descamps, L., Labadie, C., Joly, A., and *Nicolau, J.* (2009) Ensemble Prediction at Météo France (poster introduction by Olivier Riviere) *31st EWGLAM and 16th SRNWP meetings*, September 28 – October 1, 2009. Available at: http://srnwp.met.hu/Annual Meetings/2009/download/sept29/morning/posterpearp.pdf

Eckel, F.A. and *Mass, C.F.*, 2005: Effective mesoscale, short-range ensemble forecasting. *Wea. Forecasting 20*, 328–350.

Fraley, C., Raftery, A.E.. and *Gneiting, T.*, 2010: Calibrating multimodel forecast ensembles with exchangeable and missing members using Bayesian model averaging. *Mon. Wea. Rev. 138*, 190–202.

Fraley, C., Raftery, A.E., Gneiting, T., and *Sloughter, J.M.*, 2009: EnsembleBMA: An R package for probabilistic forecasting using ensembles and Bayesian model averaging. *Technical Report 516R*, Department of Statistics, University of Washington. Available at: www.stat.washington.edu/research/reports/2008/tr516.pdf

Fraley, C., Raftery, A.E., Gneiting, T., Sloughter, J.M. and Berrocal, V.J., 2011: Probabilistic weather forecasting in R. *The R Journal 3*, 55–63.

Gebhardt, C., Theis, S.E., Paulat, M., and *Bouallégue, Z.B.*, 2011: Uncertainties in COSMO-DE precipitation forecasts introduced by model perturbations and variation of lateral boundaries. *Atmos. Res. 100*, 168–177.

Gneiting, T., 2011: Making and evaluating point forecasts. *J. Amer. Statist. Assoc. 106*, 746–762.

Gneiting, T. and *Raftery, A.E.*, 2007: Strictly proper scoring rules, prediction and estimation. *J. Amer. Statist. Assoc. 102*, 359–378.

Gneiting, T., Raftery, A.E., Westveld, A.H., and *Goldman, T.,* 2005: Calibrated probabilistic forecasting using ensemble model output statistics and minimum CRPS estimation. *Mon. Wea. Rev. 133*, 1098–1118.

Hágel, E., 2010: The quasi-operational LAMEPS system of the Hungarian Meteorological Service. *Időjárás 114*, 121–133.

Horányi, A, Kertész, S., Kullmann, L., and *Radnóti, G.,* 2006: The ARPEGE/ALADIN mesoscale numerical modeling system and its application at the Hungarian Meteorological Service. *Időjárás 110*, 203–227.

Horányi, A., Mile, M., and *Szűcs, M.,* 2011: Latest developments around the ALADIN operational short-range ensemble prediction system in Hungary. *Tellus A 63*, 642–651.

Iversen, T., Deckmyn, A., Santos, C., Sattler, K., Bremnes, J.B., Feddersen, H., and *Frogner, I-L.,* 2011: Evaluation of 'GLAMEPS' - a proposed multimodel EPS for short range forecasting. *Tellus A 63*, 513–530.

Justus, C.G., Hargraves, W.R., Mikhail, A., and *Graber, D.*, 1978: Methods for estimating wind speed frequency distributions. *J. Appl. Meteor. 17*, 350–353.

Labadie, C., Descamps,L., Cebron, P., and *Michel, Y.,* 2012: PEARP initialization with Ensemble Data Asssimilation and Singular Vectors. International Conference on Ensemble Methods in Geophysical Sciences, Toulouse, France, November 12–16, 2012. Available at: http://www.meteo.fr/cic/meetings/2012/ensemble.conference/presentations/session07/2.pdf

Leutbecher, M. and *Palmer, T.N.*, 2008: Ensemble forecasting. *J. Comp. Phys. 227*, 3515–3539.

Pinson, P. and *Hagedorn, R.*, 2012: Verification of the ECMWF ensemble forecasts of wind speed against analyses and observations. *Meteorol. Appl. 19*, 484–500.

Raftery, A.E., Gneiting, T., Balabdaoui, F., and *Polakowski, M.,* 2005: Using Bayesian model averaging to calibrate forecast ensembles. *Mon. Wea. Rev. 133*, 1155–1174.

Sloughter, J.M., Gneiting, T., and *Raftery, A.E.,* 2010: Probabilistic wind speed forecasting using ensembles and Bayesian model averaging. *J. Amer. Stat. Assoc. 105*, 25–37.

Sloughter, J.M., Raftery, A.E., Gneiting, T., and *Fraley, C.,* 2007: Probabilistic quantitative precipitation forecasting using Bayesian model averaging. *Mon. Wea. Rev. 135*, 3209–3220.

Soltanzadeh, I., Azadi, M., and *Vakili, G.A.,* 2011: Using Bayesian Model Averaging (BMA) to calibrate probabilistic surface temperature forecasts over Iran. *Ann. Geophys. 29*, 1295–1303.

Thorarinsdottir, T.L. and *Gneiting, T.,* 2010: Probabilistic forecasts of wind speed: ensemble model output statistics by using heteroscedastic censored regression. *J. Roy. Statist. Soc. Ser. A 173*, 371–388.

Toth, Z. and *Kalnay, E.*, 1997: Ensemble forecasting at NCEP and the breeding method. *Mon. Wea. Rev. 125*, 3297–3319.

Tuller, S.E. and *Brett, A.C.*, 1984: The characteristics of wind velocity that favor the fitting of a Weibull distribution in wind speed analysis. *J. Appl. Meteorol. 23*, 124–134.

Wilks, D.S., 2011: Statistical Methods in the Atmospheric Sciences. 3rd ed., Elsevier, Amsterdam.

Wilks, D.S. and *Hamill, T.M.*, 2007: Comparison of ensemble-MOS methods using GFS reforecasts. *Mon. Wea. Rev. 135*, 2379–2390.

Williams, R.M., Ferro, C.A.T., and *Kwasniok, F.*, 2014: A comparison of ensemble post-processing methods for extreme events. *Q. J. R. Meteorol. Soc.140*, 1112–1120.

IDŐJÁRÁS

Quarterly Journal of the Hungarian Meteorological Service
Vol. 118, No. 3, July – September, 2014, pp. 243–256

Effects of leveling error on the measurement of global radiation

László Menyhárt[1*], **Angéla Anda**[1], and **Zoltán Nagy**[2]

[1]*Department of Meteorology and Water Management, University of Pannonia Georgikon Faculty, Festetics u. 7, H-8360 Keszthely, Hungary*

[2]*Hungarian Meteorological Service, Gilice tér 39, H-1181 Budapest, Hungary*

**Corresponding author E-mail: menyhart-l@georgikon.hu*

(Manuscript received in final form January 10, 2014)

Abstract—Pyranometers are fundamental instruments widely used for measuring global irradiance. When operating weather stations without continuous manning, pyranometer may tilt from horizontal position. Error caused by inclination of a few degrees was calculated for the annual, daily, and instantaneous global radiations. Global irradiance incident on both horizontal and tilted surfaces were calculated from the direct beam, diffuse and ground-reflected irradiances. These components were measured by accurately leveled and regularly supervised instruments. The second purpose of this paper was to determine the minimum tilt angle that is detectable by calculating certain quantities. To detect the east-west inclination, the sum of the global radiation before and after the solar noon was compared. To detect the north-south inclination, it was tested whether the global irradiance measured at a fixed solar elevation with a horizontal and a tilt pyranometer is stochastically equal. Our findings show that tilt angle of 1° in east-west direction is already detectable. Tilting to the direction at an angle of 15° from the north-south is the most difficult to detect. Here 3° is the smallest detectable tilt angle.

Key-words: global radiation, global irradiance, pyranometer, tilt error, detection of tilt, leveling of pyranometer

1. Introduction

The demand for high-precision global radiation measurement has risen steadily in recent decades. Global radiation data with high spatial and temporal resolution are required in different fields including meteorological and climate models, active and passive solar energy systems, agriculture, and the solar architecture. Consequently, the instruments measuring solar radiation have shown significant progress. The number of weather stations equipped with solar instruments continues to grow, and the use of pyranometers for industrial purposes became general. In spite of this, compared to other meteorological variables, the measurement of solar radiation is more prone to errors *(Moradi,* 2009*)*. *Younes et al.* (2005) classified the most general types of errors into two major categories: (1) equipment error and uncertainty, and (2) operational related problems and errors. The former includes the cosine response, azimuth response, temperature response, spectral selectivity, stability, non-linearity, and dark offset long-wave radiation error. The latter includes the incorrect sensor leveling, shading caused by objects above the horizon, electric fields in the vicinity of cables, mechanical loading of cables (piezoelectric effects), dust, snow, dew, bird -droppings, etc. A variety of useful procedures for post-measurement quality control have been published in the past years *(Geiger et al.,* 2002*;* *Muneer* and *Fairooz,* 2002*;*, *Younes et al.,* 2005*;* *Shi et al.,* 2008; *Moradi,* 2009*;*, *Tang et al.,* 2010; *Journée* and *Bertrand,* 2011*;* *Miras-Avalos et al.,* 2012*)*. These methods define an upper and a lower threshold and remove values being outside the acceptance range. So the extremely low or high values are eliminated, however, a value between the thresholds may also be erroneous. The correction of the equipment errors are dealt with in several papers as well *(Stoffel et al,* 2000*;* *Reda,* 1999*;*, *Bush et al.,* 2000*;* *Reda et al.,* 2005*;* *Lester* and *Myers,* 2006*;*, *Ji,* 2007*;* *Marquez et al.,* 2010*)*.

Our aim is to develop a method to detect the tilt of the pyranometer without additional measurements. This paper is the first step in the program. One purpose is to quantify the effects of the tilt. The second purpose is to estimate the minimum tilt angle which is detectable from the time series of global irradiance alone.

To help the accurate leveling of the pyranometer, the instrument is supplied with a spirit level. In case of careful mounting, the angle between the plane of the sensor and the horizontal is less than 1° or 0.1°, depending on the type of the pyranometer. In case of tilt, posterior correction is not possible, since neither the direction nor the extent of the tilt are known. Global radiation incident on a tilted surface is essential for different uses of solar energy, so numerous studies focus on its estimation. In such cases, the angle between the absorbing surface and the horizontal is considerably greater than in the case of pyranometer leveled incorrectly. If the latter is tilted over 5°, it is already visible to the naked eye. Therefore, the effects of tilt angle not greater than 10° were investigated.

Bacher et al. (2013) presented a method to correct systematical errors, including tilt error. The sensor output level under clear-sky conditions is estimated directly from the observation by means of quantile regression. This is compared to solar radiation calculated with a clear-sky model. The different types of systematical errors are not examined separately, all of them are corrected in the same step.

Tilt error is particularly common if solar irradiance is measured from ship, buoy, aircraft, or other moving platforms. Correction methods developed for moving platforms is presented in *Long et al.,* (2010) and *Boers et al.,* (1998). The error due to the rocking motion and preferential tilt were calculated using the assumption that the diffuse to direct ratio was constant (*Katsaros* and *DeVault,* 1986). The novelty of the present study is that instead of estimating this ratio, a full-year time series of direct, diffuse, and reflex irradiances are used.

2. *Material and methods*

The error caused by tilt depends basically on the solar position, direction and magnitude of the tilt, and the diffuse to direct ratio. Carrying out measurements with pyranometers tilted in different directions and to different degrees would be extremely lengthy and costly. Therefore, both the global irradiance incident on horizontal and that incident on inclined surface were calculated from diffuse horizontal irradiance, direct normal irradiance, and ground-reflected irradiance. The data used in this paper were measured in the György Marczell Main Observatory (47°25'45"N and 19°10'56"E) of the Hungarian Meteorological Service from January 1, 2011 to November 27, 2011 and from December 8, 2011 to December 31, 2011. Both the diffuse irradiance and the ground-reflected irradiance were measured with Kipp&Zonen CM11 pyranometers while the direct normal irradiance was measured by Kipp&Zonen CH1 pyrheliometer. All measurements were carried out with precisely leveled instruments with continuous supervision. Sampling took place in every two seconds and their means were recorded on ten minute basis. The solar coordinates were calculated for the middle of the ten-minute intervals by the algorithm proposed by *Reda* and *Andreas* (2004).

In case of horizontal pyranometers, the global irradiance was calculated as the sum of the diffuse sky irradiance and the vertical component of the direct solar irradiance.

$$G_H = B \cdot \sin\varphi + D, \tag{1}$$

where G_H is the global irradiance incident on horizontal surface, B is the direct normal irradiance, D is the diffuse sky irradiance, and φ is the solar elevation.

When the pyranometer is tilted, it loses irradiance from a portion of the sky and instead receives radiation from below the horizon. So, in such a case the global irradiance was calculated by

$$G_t = B_t + D_t + R_t, \tag{2}$$

where G_t is the global irradiance incident on tilted surface, B_t, D_t, and R_t are the components of direct normal, sky diffuse, and ground-reflected irradiances, respectively. These components are perpendicular to the plane of the pyranometer and calculated by

$$B_t = B \cdot [\sin\varphi \cdot \cos s + \cos\varphi \cdot \cos(\alpha - \gamma) \cdot \sin s], \tag{3}$$

$$D_t = D \cdot \frac{1 + \cos s}{2}, \tag{4}$$

$$R_t = R \cdot \frac{1 - \cos s}{2}, \tag{5}$$

where s is the tilt angle that the plane of the pyranometer makes with the horizontal surface (s is always positive and represents the slope in any direction), γ is the azimuth angle of the tilt, where γ=0 for slopes oriented to south and it increases in clockwise direction. α is the solar azimuth and R is the ground-reflected irradiance measured by a horizontal, downward facing pyranometer. Eqs. (3), (4), and (5) are detailed in *Iqbal* (1983). Both the sky diffuse and ground-reflected irradiances were considered as isotropic, since the investigated tilt angle was restricted below 10°. Eqs. (4) and (5) show that if s is small then $D_t \approx D$ and $R_t \approx 0$. Consequently, the direct component is mostly affected by the inclination.

If a measured value or the calculated B_t component was negative it was replaced with zero.

The relative error caused by the tilt was calculated by

$$E = \frac{G_t - G_H}{G_H}, \tag{6}$$

where γ was varied between 0° and 330° by 30°, as well as s was varied between 1° and 10° by 1°. Annual, diurnal, and instantaneous global radiations

were calculated for each case. The tilt of the pyranometer was assumed to be constant all year.

Quantities appropriate to detect the tilt of the pyranometer were looked for. Tilt towards the east or west causes diurnal asymmetries in the global radiation. Asymmetry may also be caused by diurnal variation of the atmospheric transmittance. Whereas the direction of the asymmetry caused by the tilt is the same on each day, that caused by the variation of the transmittance varies stochastically. To detect the inclination, those days shall be used when the direct to global ratio is high and the diurnal variation of the atmospheric transmittance is low. Three days where the diurnal global radiation was the highest were selected in each month. Sum of the global radiation measured before and after the solar noon were compared with paired samples t-test. The assumption underlying this test is that the difference of the two variables follows a normal distribution. Normality was tested with Shapiro-Wilk test. Statistical significance level was accepted to be $p<0.05$.

Tilt towards the north or south does not cause diurnal asymmetry. However, it causes distortion in the annual course of global irradiance corresponding to a given solar elevation. The lower the sun, the higher the angle of incidence and the greater the tilt error. At low solar elevation angles, around the winter solstice the sun is in the southern sky, and around the summer solstice it is in the northern sky. Consequently, the global irradiance measured by a pyranometer tilted towards the south is higher in winter and lower is summer compared with those measured by a horizontal pyranometer. This effect decreases with the increase of solar elevation in summer, because the sun moves away from the north. That is why the days around the winter solstice are the most suitable to detect the north-south tilt.

Sixty days before and after the winter solstice were used. These days were randomly divided into two groups of equal size. On the days being in the first and second group, the global irradiance measured with the horizontal and the tilted pyranometer was modeled, respectively. The highest 20 values corresponding to a given solar elevation were selected from both groups. Since these data did not follow the normal distribution, they were compared with the nonparametric Mann-Whitney U test. Statistical significance level was accepted to be $p<0.05$. Global irradiance corresponding to the solar elevation of 8°, 10°, 12°, 14°, 16°, 18°, 20°, and 22° were examined one by one. In order to eliminate the effect of randomness, the days when the pyranometer was assumed to be horizontal and tilted, respectively, were interchanged. The statistical test was repeated in this way. The difference was considered to be due to the tilt only if it was found significant in both cases.

If there is not a sufficient number of clear-sky measurements, the twenty highest values may include partially cloudy measurements too. It may reduce the power of the method. Therefore, the whole procedure was repeated with the highest 10 values corresponding to the given solar elevation.

The measurements were not carried out at the same solar elevation on each day. Therefore, the values of solar elevation expressed in degree were rounded to the nearest whole number. Hence, the global irradiance was corrected with linear interpolation as follows. When the solar elevation was rounded up before the solar noon or rounded down after the solar noon, then

$$G_t^{\text{int}} = G_t + \frac{G_{t+1} - G_t}{\varphi_{t+1} - \varphi_t}\left(\varphi_t^{\text{int}} - \varphi_t\right). \tag{7}$$

When the solar elevation was rounded down before the solar noon or rounded up after the solar noon, then

$$G_t^{\text{int}} = G_t + \frac{G_{t-1} - G_t}{\varphi_{t-1} - \varphi_t}\left(\varphi_t^{\text{int}} - \varphi_t\right), \tag{8}$$

where G_t^{int} is the global irradiance corresponding to the rounded solar elevation, G_t, G_{t+1}, and G_{t-1} are the global irradiance corresponding to the actual, 10 minutes later, and 10 minutes earlier measurements, respectively.

3. *Results*

3.1. Annual total global radiation

The relative error of the annual total global radiation was found to be directly proportional to the tilt angle in case of a fixed tilt direction (*Fig. 1*) in the examined range. It was found to be estimated by

$$E_{year} = s(-0.00054 + 0.0070\cos\gamma), \tag{9}$$

where E_{year} is the relative error of the annual total global radiation and s is expressed in degree. The goodness of fit of the model was excellent, R^2=0.99. Tilt towards the north and south results in a relative error of –0.0075 and 0.0065 per degree, respectively. The lowest error, 0.0005 per degree, was found in the case of tilt towards the east or west.

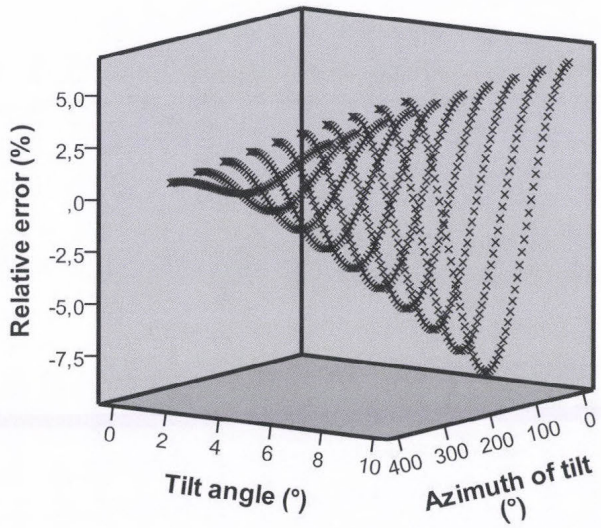

Fig. 1. Relative error of the annual total global radiation in 2011.

3.2. Daily total global radiation

The annual course of the error of the daily total global radiation has a typical pattern. The two most different cases are shown in *Fig. 2*. As it was expected, the lowest relative error was found on clear-sky day in winter with pyranometer tilted towards the north. In case of tilt angle of 1°, this error was lower than –4.5% (*Fig. 2a*). The same tilt caused an error about –0.3% around the summer solstice. The errors around zero were observed on the overcast days when the direct normal irradiance was zero or negligible. There were some days on summer, when the error was positive. It occurred on the days, when the direct normal irradiance was high in the morning and in the evening, and the sun was in the northern sky, and it was low around the solar noon when the sun was in the southern sky. The lower envelope of the scatter plot (*Fig. 2a*) shows the relative error corresponding to the clear-sky days.

In case of pyranometer tilted towards the east or west, the relative error was about zero both on the clear-sky and the overcast days (*Fig. 2b*). The relative error with the highest absolute value was found on the days when the morning was overcast and the afternoon was clear-sky or vice versa. On these days the absolute value of the relative error caused by tilt angle of 1°was about 1%, while on clear-sky days it was about 0.1%.

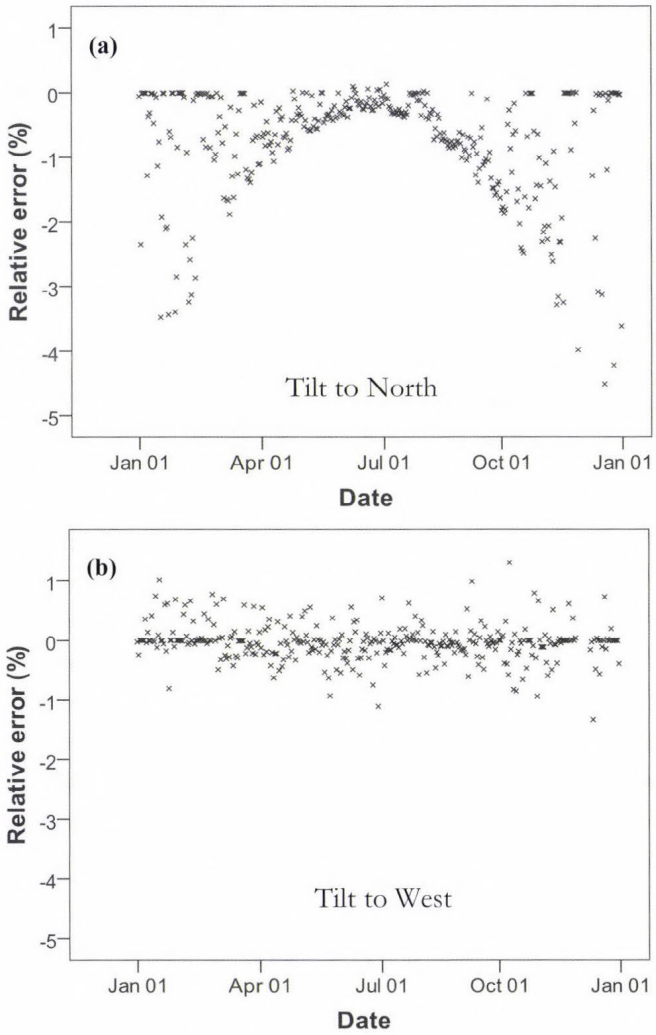

Fig. 2. Relative error of the daily total global radiation for tilt of 1° (a) to the north and (b) to the west, in 2011.

3.3. Global irradiance

The daily course of the relative error of the global irradiance depends strongly on the apparent daily path of the sun. To present the three most different cases, a clear-sky day was selected from around the summer solstice, autumn equinox, and winter solstice (*Fig. 3*). Compared to the annual or daily total, the relative

error of the 10-minute average, caused by the same tilt, was notably higher. Around the winter solstice at low solar elevation angles, the error caused by the tilt of 1° to the south exceeds 8%. At solar elevation angles higher than 30°, even if the pyranometer is tilted towards the sun, the error caused by the tilt of 1° is lower than 1% (*Fig. 3a*).

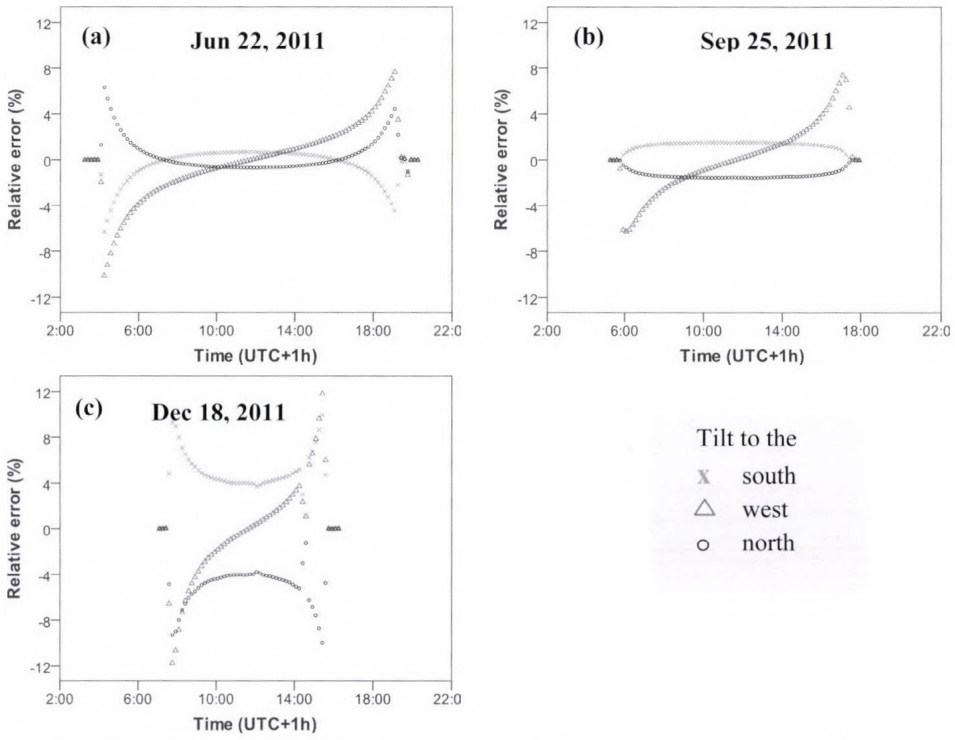

Fig. 3. Relative error of global irradiance, caused by the tilt of 1° around the (a) summer solstice, (b) autumnal equinox, and (c) winter solstice.

3.4. Comparison of the total global radiation measured before and after the solar noon

The tilt angles and the azimuth angles at which the comparison was carried out are shown in *Table 1* and *Table 2*. The difference of the two quantities followed normal distribution in each case. The results, as shown in *Table 1*, indicate that even tilt of 1° resulted in significant asymmetry if the azimuth of the tilt was within the range of 60° to 120° or 240° to 300°. For tilt angle of 1.5°, the asymmetry was significant when the azimuth of the tilt ranged from 30° to 150° or from 210° to 330°. The closer the tilt direction to the north or to the south, the less the asymmetry expected to be significant. If the direction, of the tilt makes

an angle of 15° with the south-north direction the tilt angle must be at least 3° to result in significant asymmetry (*Table 2*).

Table 1. Difference of the total global radiation measured before and after the solar noon (kJ/m^2) in case of tilt angles smaller than 2°

tilt angle	0°	30°	60°	90°	120°	150°	180°	210°	240°	270°	300°	330°
0.5°	27	92	139	157	139	91	12	–101	–149	–166*	–149	–52
1.0°	18	149	253**	287**	251**	155	11	–166*	–262**	–296**	–262**	–178*
1.5°	19	216*	366**	417**	364**	220**	10	–232**	–374**	–427**	–389**	–244**

(*:$p<0.05$; **:$p<0.01$)

Table 2. Difference of the total global radiation measured before and after the solar noon (kJ/m^2) in case of tilt angles of 2° and 3°

tilt angle	15°	165°	195°	345°
2°	155	144	–171*	–169*
3°	194*	209**	–238**	–242**

(*:$p<0.05$; **:$p<0.01$)

3.5. Global irradiance corresponding to a given solar elevation angle

This quantity has a typical annual course due to the annual variation of the Sun-Earth distance and the atmospheric transmittance. It was modified by the tilt of the pyranometer (*Fig. 4*). The closer the solar azimuth corresponding to the given solar elevation angle to the azimuth of the tilt, the higher the relative error. Consequently, the error with the highest absolute value was found around the winter solstice in case of tilt to north-south (*Fig. 5a*). In case of tilt to east-west, it was found sometimes after the spring equinox as well as sometimes before the autumn equinox (*Fig. 5b*). Obviously, the exact date depends on the solar elevation angle in question.

Global irradiance corresponding to a given solar elevation was expected to show the tilt to the south-north direction. That is why the global irradiance incident on the horizontal and the tilted surface was only compared when the azimuth of the tilt was within the ranges of 0°–30°, 150°–210° and 330–360°. Due to the high number of the comparisons, only the significance of the

difference is reported. Let a particular tilt be called detectable at a given solar elevation angle if the difference corresponding to the given solar elevation angle was found statistically significant regardless of which days were considered horizontal. These cases are highlighted with dark background in *Table 3*. The tilt of 1.5° to south was detectable at none of the solar elevation angles. Even the tilt of 2° to south was detectable at only two solar elevation angles. Tilt of 3° within the ±30° range around the south-north direction was already detectable at four different solar elevation angles. These results indicate that tilt to south-north is harder to detect than the tilt to east-west. The smallest detectable tilt angle in each tilt direction is presented in *Fig 6*.

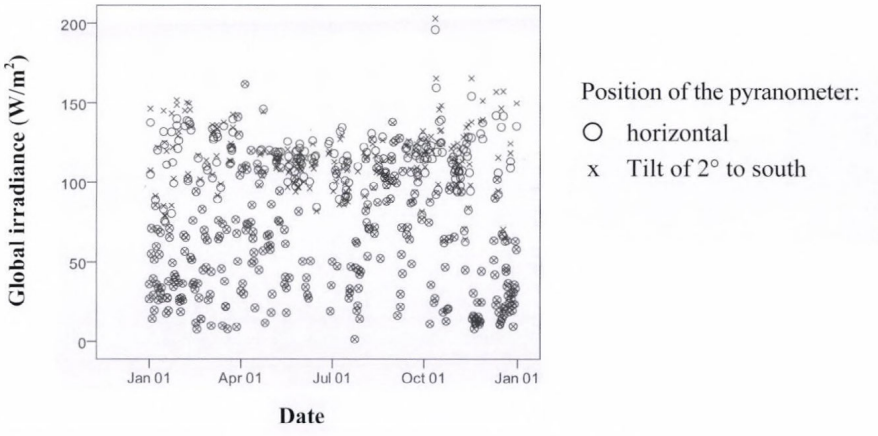

Fig. 4. Global irradiance corresponding to the solar elevation of 10°, in 2011.

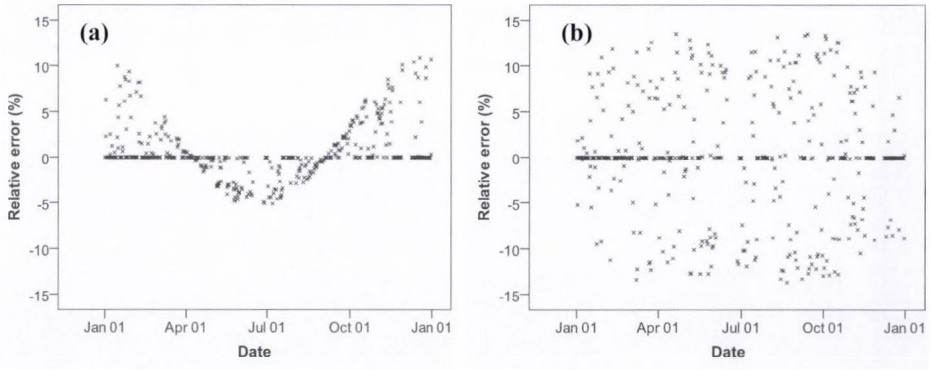

Fig. 5. Relative error of the global irradiance corresponding to the solar elevation of 10° in case of a 2° tilt (a) towards the south and (b) west, in 2011.

Table 3. Significance of the difference of global irradiance incident on the horizontal and the tilted surface. At tilt azimuth of 15°, 165°, 195°, 345°, the test was carried out at tilt angle of only 3°.

tilt angle	sol. elev.	0°	15°	30°	150°	165°	180°	195°	210°	330°	345°
1,5°	8°	* d		* d	* d		*dd		* d	* d	
	10°	* d		* d	* d		* d		* d	* d	
	12°	* d		* d	* d		* d		* d	* d	
	14°	* d		* d	*		*		*	* d	
	16°	* d		* d	*		*		*	*	
	18°	* d		* d	* d		* d		* d	* d	
	20°	*		* d	* d		* d		* d	* d	
	22°	*		* d	*		*		*	*	
2°	8°	* dd		* d	* d		*dd		*dd	*dd	
	10°	* d		*d	* d		*dd		* d	* d	
	12°	* d		*d	* d		* d		* d	* d	
	14°	* dd		*dd	* d		*dd		*	*dd	
	16°	* d		*d	*		**d		*	* d	
	18°	* d		*d	* d		* d		* d	* d	
	20°	*		*d	* d		* d		* d	*	
	22°	* d		d	*		*		*	*	
3°	8°	* dd	* d	* d	* d	**dd	**dd	**dd	**dd	*dd	*dd
	10°	* dd	*dd	* d	*dd	*dd	*dd	*dd	* d	* d	* d
	12°	* dd	*dd	* d	* d	*dd	* dd	*dd	* d	* d	*dd
	14°	* dd	*dd	*dd	**d	**dd	**dd	**dd	*dd	*dd	*dd
	16°	**dd	**dd	*dd	**d	*dd	**dd	* dd	**dd	*dd	**dd
	18°	**d	**d	**d	**d	**d	**d	**d	**d	**d	**d
	20°	* d	* d	* d	* d	* d	* d	* d	* d	* d	* d
	22°	**dd	** dd	** dd	**	*dd	**dd	** d	** d	**dd	**dd

*: p<0.05 with the 20 highest values; d: p<0.05 with the 10 highest values;
**: p<0.05 with the 20 highest values regardless of which days were considered horizontal; dd: p<0.05 with the 10 highest values regardless of which days were considered horizontal. ** and dd are denoted with grey background.

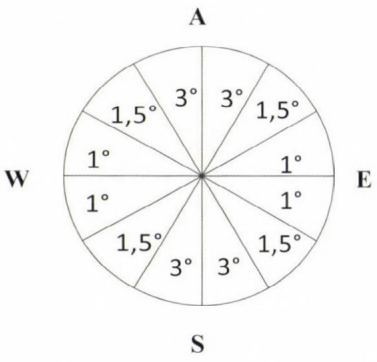

Fig. 6. The smallest detectable tilt angles in each tilt direction. Sectors represent ranges of 30°.

4. Discussion

The uncertainty of the daily total global radiation shall not exceed 2%, 5%, and 10% in cases of the secondary standard, first class, and second class pyranometers, respectively, according to the ISO standard (*ISO,* 1990). Our findings show that even a tilt of 1° can cause greater variation in the daily total values than the inherent uncertainty of a secondary standard pyranometer. The effect of a tilt of 2.5° can exceed the inherent uncertainty of even a second class pyranometer. It indicates that developing a method that assesses the data series of global irradiance with respect to the leveling would be very useful.

The aim of this paper was to find quantities that are calculated only from global radiation and suitable to assess the leveling of the pyranometer. The difference of the total global radiation measured before and after the solar noon has been shown to be very sensitive to the tilt to east-west. As small as tilt of 1° to east-west can be detected. The method is adaptable to any latitude, but the value of 1° refers only to the latitude of around 47°N. The selection of clear-sky days is a key element in the process. Refinement of the selection method is expected to shorten the length of the measurements necessary for the detection of a tilt.

The highest error in both the annual and the daily total global radiation is caused by the tilt to south-north, yet it is the most difficult to detect. Three degrees as the smallest detectable tilt seems like a lot. Assessing the global irradiance corresponding to a given solar elevation angle requires reference data that is considered as horizontal global irradiance. In the current study it was calculated from measurements of a few days. Future work will involve a multi-annual high accuracy measurement series. It will give the opportunity to analyze the annual course of the solar irradiance corresponding to a given solar elevation angle rather than the 10 or 20 highest values measured around the winter solstice. It is expected to allow smaller tilts to become detectable.

Overall, the power of the method using the twenty highest values is greater than that using the ten highest values. However, half of the cases showed by the twenty highest values were not showed by the ten highest values. It proves that both procedures were reasonable to use. The strength of investigating the solar irradiance corresponding to a given solar elevation angle is that it does not require clear-sky days, only shorter clear-sky periods of time. Its drawback is that the power to detect the tilt is not the same in each part of the year. Investigating the morning and afternoon solar irradiances separately can contribute to the detection of the tilt to east-west.

It has been shown that there is a good chance to detect a tilt as small as 1° to east-west, and we hope that as small as 2° will be detectable in any other directions by the refinement of the method. Future works will carry out measurements with tilted pyranometers to verify these findings.

Acknowledgements–The financial and infrastructural support of the State of Hungary and the European Union in the frame of the TÁMOP-4.2.2/B-10/1-2010-0025 project is gratefully acknowledged.

References

Bacher, P., Madsen, H., Perers, B., and *Nielsen, H. A.,* 2013: A non-parametric method for correction of global radiation observations. *Solar Energy 88*, 13–22.

Boers, R., Mitchell, R.M., and *Krummel, P.B.,* 1998: Correction of aircraft pyranometer measurements for diffuse radiance and alignment errors. *J. Geophys. Res. 103(D13)*, 16753–16758.

Bush, B.C., Valero, F.P.J., Simpson, A.S., and *Bignoneet, L.,* 2000: Characterization of thermal effects in pyranometers: a data correction algorithm for improved measurement of surface insolation. *J. Atmos. Ocean. Tech. 17*, 165–175.

Geiger, M., Diabate, L., Menard, L., Wald, L., 2002: A web service for controlling the quality of measurements of global solar irradiation. *Solar Energy 73*, 475–480.

ISO: International Organization for Standardization, 1990: Solar Energy – Specification and Classification of Instruments for Measuring Hemispherical Solar and Direct Solar Radiation. ISO 9060.

Iqbal, M., 1983: An introduction to solar radiation. Academic press, New York, Chap 11, 303–334.

Ji, Q., 2007: A method to correct the thermal dome effect of pyranometers in selected historical solar irradiance measurements. *J. Atmos. Ocean. Tech. 24*, 529–536.

Journée, M. and Bertrand, C., 2011: Quality control of solar radiation data within the RMIB solar measurements network. *Solar Energy 85*, 72-86.

Katsaros, K.B. and *DeVault, J.E.,* 1986: On irradiance measurement errors at sea due to tilt of pyranometers. *J. Atmos. Ocean. Tech. 3*, 740–745.

Long , C.N., Bucholtz, A., Jonsson, H., Schmid, B., Vogelmann, A., and *Wood, J.,* 2010: A Method of Correcting for Tilt from Horizontal on Downwelling Shortwave Irradiance Measurements on Moving Platforms. *Open Atmos. Sci. J. 4*, 78–87.

Lester, A. and *Myers, D.R.,* 2006: A method for improving global pyranometer measurements by modeling responsivity functions. *Solar Energy 80*, 322–331.

Marquez, J.M.A., Bohorquez, M.A.M., Garcia, J.M., and *Nieto, F.J.A.,* 2010: A new automatic system for angular measurement and calibration in radiometric instruments. *Sensors 10*, 3703–3717.

Miras-Avalos, J.M., Rodriguez-Gomez, B.A., Meizoso-Lopez, M.C., Sande-Fouz, P., Gonzalez-Garcia, M.A., and *Paz-Gonzalez, A.,* 2012: Data quality assesment and monthly stability of ground solar radiation in Galicia (NW Spain) *Solar Energy 86,* 3499–3511.

Moradi, I., 2009: Quality control of global solar radiation using sunshine duration hours. *Energy 34,* 1–6.

Muneer, T. and *Fairooz, F.,* 2002: Quality control of solar radiation and sunshine measurements–lessons learnt from processing worldwide databases. Building *Serv. Engin. Res. Tech. 23*, 151–66.

Reda, I., 1999: Improving the Accuracy of Using Pyranometers to Measure the Clear Sky Global Solar Irradiance. *9th ARM Science Team Meeting Proceedings,* San Antonio, Texas, March 22–26.

Reda, I. and *Andreas, A.,* 2004: Solar Position Algorithm for Solar Radiation Applications, *Solar Energy 76*, 577–589.

Reda, I., Hickley, J., Long, C., Myers, D., Stoffel, T., Wilcox, S., Michalsky, J.J., Dutton, E. G. and *Nelson, D.,* 2005: Using a blackbody to calculate net longwave responsivity of shortwave solar pyranometers to correct for their thermal offset error during outdoor calibration using the component sum method. *J. Atmos. Ocean. Tech. 22*, 1531–1540.

Shi, G.Y., Hayasaka, T., Ohmura, A., Chen, Z.H., Wang, B., Zhao, J.Q., Che, H.Z., and *Xu, L.,* 2008: Data quality assessment and the long-term trend of ground solar radiation in China. *J. Appl. Meteorol. Climatol. 47*, 1006–1016.

Stoffel T, Redo I, Myers D, Renne D, Wilcox S, and *Treadwell J.,* 2000: Current issues in terrestrial solar radiation instrumentation for energy, climate andspace applications. *Metrologia 37*, 399–402.

Tang, W., Yang, K., He, J., and *Qin, J.,* 2010: Quality control and estimation of global solar radiation in China. *Solar Energy 84,* 466–475.

Younes, S., Claywell, R., and *Muneer, T.,* 2005: Quality control of solar radiation data: present status and proposed new approaches. *Energy 30,* 1533–1549.

IDŐJÁRÁS

Quarterly Journal of the Hungarian Meteorological Service
Vol. 118, No. 3, July – September, 2014, pp. 257–281

Microclimate-vegetation relationships in natural habitat islands: species preservation and conservation perspectives

Zoltán Bátori[1]*, Attila Lengyel[2], Miklós Maróti[3], László Körmöczi[1], Csaba Tölgyesi[1], András Bíró[3], Miklós Tóth[3], Zoltán Kincses[4], Viktória Cseh[1], and László Erdős[1]

[1]*University of Szeged, Department of Ecology, H-6726 Szeged, Közép fasor 52, Hungary*

[2]*Hungarian Academy of Sciences, Institute of Ecology and Botany, H-2163 Vácrátót, Alkotmány u. 2-4, Hungary*

[3]*University of Szeged, Bolyai Institute, H-6720 Szeged, Aradi vértanúk tere 1, Hungary*

[4]*University of Szeged, Department of Technical Informatics, H-6720 Szeged, Árpád tér 2, Hungary*

**Corresponding author E-mail: zbatory@gmail.com*

(Manuscript received in final form February 10, 2014)

Abstract— Information about the relationship between the spatial and temporal patterns of different climatic parameters and the vegetation is especially important from a nature conservation perspective. We studied the influence of microclimatic parameters (air temperature and air humidity) on certain natural habitat islands (karst sinkhole and sand dune slack) and on their plant species composition and vegetation pattern in Hungary. Vegetation data together with topographic variables were collected along transects to reveal the vegetation patterns on the slopes. Microclimatic parameters were measured with wireless sensor motes equipped with air temperature and humidity sensors. Interactions were examined using distance-based redundancy analysis. We found that the species composition of natural habitat islands varied markedly within short distances, depending on the prevailing microclimatic conditions. Elements of microclimate (daily, daytime, and nighttime averages) have different effects on vegetation pattern and species composition. The observed patterns can be interpreted based on our knowledge on the structure of plant communities and on the role of geomorphology. Future temperature increase, droughts, and forestry activities are the main threats to the habitat diversity and hence to the species diversity of habitat islands in Hungary.

Key-words: air humidity, air temperature, climate change, habitat island, Hungary, refugium, vegetation inversion, wireless sensor

1. Introduction

Microclimate is a suite of climatic conditions measured usually directly on the ground or very close to it (*Geiger*, 1965). The effects of different microclimatic parameters (e.g., air temperature and air humidity) on animals and plants have been widely studied because they are essential to individual organisms for reproduction (e.g., germination) and ecological processes (e.g., evapotranspiration, microbial activity, nutrient cycling, photosynthesis, and regeneration) (*Bátori et al.*, 2012a; *Forseth* and *Teramura*, 1987; *Holl*, 1999; *Marlatt*, 1961; *Schimel* and *Parton*, 1986). The interactions between microclimate and vegetation have been studied both at local and regional scales. Local-scale studies have focused mainly on individuals and stands, providing important information about the local ecological processes and sometimes, based on the extension and generalization of the results, about larger-scale ecological processes (*Antonić et al.*, 1997; *Bátori et al.*, 2011; *Herrera*, 1995). The number of landscape studies examining microclimate and its relationship with flora, vegetation, and related ecological processes in the context of landscape is much lower (*Xu et al.*, 2004).

The interaction between topography and climate is complex and its details are not completely understood (*Dobrowski*, 2011). There is no doubt, however, that topography and related terrain effects strongly affect the local environmental and climatic conditions (*Bátori et al.*, 2009; *Geiger*, 1950; *Whiteman et al.*, 2004). The effect of geomorphology on temperature inversion strengths, diurnal temperature regimes, and vertical temperature gradients has a great impact on vegetation pattern and plant survival. However, vegetation cover usually has a mitigating effect on air and soil temperatures (*Allen* and *Burton*, 1993; *Fetcher et al.*, 1985; *Oliver et al.*, 1987); therefore, elements of microclimate are usually less extreme in forests than in grasslands. In addition, many studies suggest that not only the diurnal or monthly average temperature and humidity values but also the differences between the daytime and nighttime averages as well as their changes affect markedly species composition, vegetation pattern, and ecological processes (*Liu et al.*, 2006; *Mohammed* and *Tarpley*, 2009; *Shiu et al.*, 2009). It is important to note that management related variables often explain more variation in vegetation than any other variables together, indicating the importance of management as determining species composition (*Aude* and *Lawesson*, 1998). Therefore, the effects of microclimate must be interpreted differently under different disturbance regimes, various topographical features, and vegetation covers.

The spatial distribution of microclimate is an essential factor for habitat suitability for many species (*Mantilla-Contreras et al.*, 2011; *Rich* and *Weiss*, 1991). Since climate change apparently affects the occurrences of species and the phenology of animal and plant activity (*Molnár et al.*, 2012; *Rijnsdorp et al.*, 2009; *Thomas et al.*, 2004; *Walther et al.*, 2002) by shifting the overall

temperature distribution, changing the precipitation regime and increasing the frequency of extreme weather events (*Easterling et al.*, 2000; *Parmesan et al.*, 2000), the investigation of the habitats suitable for providing refugia for affected species is of crucial importance. One of the most important insights that scientists can offer for conservation biology is how species are expected to respond to changes in regional and local climate. Hence, an increasing number of species distribution models have recently been reported (*Rasztovits et al.*, 2012; *Schwartz et al.*, 2006). From the point of view of an ecologist, investigations of island-like habitats can offer many possibilities to answer the above question (*Bátori et al.*, 2012b; *Körmöczi et al.*, 1981). According to the well accepted theory, 'islands' should not necessarily be land masses in water but may be particular geological types, soil types, or vegetation types surrounded by dissimilar types of rock, soil or vegetation (*Begon et al.*, 2006). However, we must distinguish between (semi)natural habitat islands and artificially created habitat islands (e.g., agricultural fields, cities, secondary grasslands), because environmental conditions (e.g., microclimate, nutrient availability, water supply), ecological processes, and organism responses are fundamentally different in the two types (*Pinke et al.*, 2012; *Unger*, 1999).

Several previous studies focused on relatively small areas with special temperature and humidity properties that harbor many species that once occurred in larger and more continuous populations (*Müller et al.*, 2006; *Turlure et al.*, 2010). For example, the lowland fens of the Carpathian Basin serve as refuges for many boreal plants (e.g., *Menyanthes trifoliata* L., *Potentilla palustris* (L.) Scop., *Trollius europaeus* L.), and the karst sinkholes and deep ravines of hill and mountain ranges preserved high-mountain species (e.g., *Rubus saxatilis* L., *Stachys alpina* L., *Viola biflora* L.) (*Király*, 2009; *Simon*, 2000). Most of these plants are climatic relicts, whose populations persist in isolated enclaves of suitable climate space surrounded by areas where the climate is not suitable for them (*Hampe* and *Jump*, 2011). Therefore, these habitats can be used for vegetation history studies as well, because their flora reflects cooler climatic periods (*Bátori et al.*, 2012b). Not only climate relicts but also other groups of species may be good indicators for microclimatic conditions of different habitats. For example, *Erdős et al.* (2013) revealed that the vascular plants of the mosaic of lowland xeric grasslands and mesic forests indicate very different climatic conditions along an edge to interior gradient. They also pointed out that the species composition of these habitat complexes may be very diverse and may contain many rare and endangered mesic forest plants, which are more characteristic of the hill and mountain ranges of the Carpathian Basin. In these cases, the local climatic conditions allow many species to maintain their populations in places where the surrounding environmental conditions (e.g., warmer climate) are not suitable for them.

The objective of this study is to examine and compare the species composition and vegetation pattern of natural habitat islands in Hungary, and to

make an attempt to explain these phenomena with microclimatic variables including the daily, daytime and nighttime air temperature and air humidity regimes. We also discuss the potential role of these habitats in preserving different groups of plant species under future climate change.

2. Methods

2.1. Study sites and vegetation survey

Study sites were selected in two different parts of Hungary (*Fig. 1*), where the landscapes contain many natural habitat islands. The fieldwork was conducted between 2009 and 2012 in a large karst sinkhole of the Mecsek Mountains (46°7'17" N, 18°12'11" E; 498 m above sea level) and in a deep sand-dune slack of Bugac (46°41'46" N, 19°36'9" E; 111 m above sea level). All samples were taken in summer, when the influence of spatial microclimatic properties was expected to be the greatest on the habitat islands. Neither site showed signs of considerable human or animal disturbance.

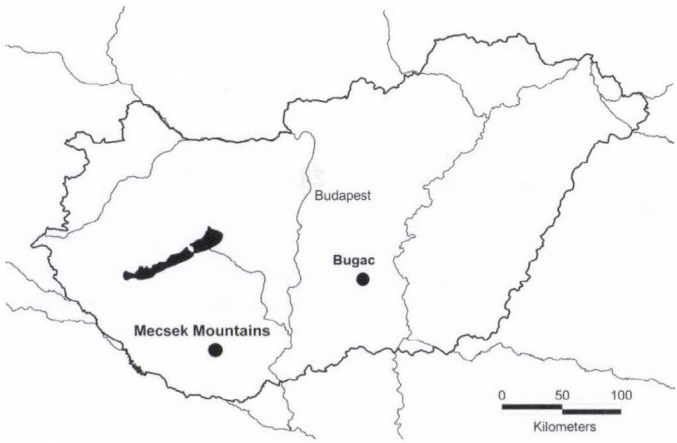

Fig. 1. Location of the study sites in Hungary.

Transect sampling was applied in both sites. Plot sizes were optimized according to our former studies and experiences (*Bátori et al.*, 2012b; *Tölgyesi* and *Körmöczi*, 2012).

In the Mecsek Mountains, a sub-Mediterranean type, middle-aged mesic oak-hornbeam (*Asperulo taurinae-Carpinetum*) and beech forests (*Helleboro odori-Fagetum*) covered the north-facing, east-facing, and west-facing slopes of the approximately 30 m deep sinkhole. A transition between a xeric turkey oak-sessile oak forest (*Potentillo micranthae-Quercetum dalechampii*) and an oak-

hornbeam forest occurred on the south-facing rim and an oak-hornbeam forest on the south-facing slope. The sinkhole bottom was covered by a ravine forest (*Scutellario altissimae-Aceretum*) (*Bátori et al.*, 2011). Herb layer was sampled along a 2 m wide and 243 m long transect consisting of 50 plots, 2 m × 1 m each. The transect was established in a north to south direction traversing the deepest point of the sinkhole.

At Bugac, a xeric grassland (*Festucetum vaginatae*) occupied the major part of the investigated sand dune (*Körmöczi* and *Balogh*, 1990), which is part of the Kiskunság Sand Ridge. The lower parts of the dune were covered by a remnant of a wet interdune vegetation patch (*Molinio-Salicetum rosmarinifoliae*). The vegetation was sampled along a 1 m wide and 14 m long transect consisting of 14 plots, 1 m × 0.25 m each. The transect was established in a northeast to southwest direction (following the orientation of the dune) traversing the deepest point of the dune slack. The elevation difference between the highest and deepest points was approximately 1.7 m.

Presence/absence of all vascular plant species (including tree saplings and low shrubs), mosses and lichens of the summer aspect was recorded in all plots (see *Appendix*). According to the topographic profiles of each transect, the plots were classified into two groups: plots of the upper slopes and plots of the bottoms. The different habitats (the bottom and upper transect sections) were compared based on vegetation and microclimatic parameters during subsequent analyses.

Plant community names are used according to *Borhidi et al.* (2012), the nomenclature of mosses and lichens follow *Simon* (1991), while the names of vascular plant taxa follow *Király* (2009).

2.2. Microclimate measurement

We used 50 IRIS (XM2110CA) wireless sensor motes from Crossbow, each of which was equipped with an MTS400 (SN21140CA) weather sensor board, which included air temperature and air humidity sensors. We measured air temperature (°C) and air humidity (%) for 24 hours 25 cm above the ground surface in the plots of the 2 transects. The signals from the sensors were recorded once every minute, therefore, 1440 temperature and 1440 humidity datapoints (24 × 60, respectively) were obtained from each mote. From these data, the daily minimum air temperature (DMinAT), daily maximum air temperature (DMaxAT), daily minimum air humidity (DMinAH), daily maximum air humidity (DMaxAH), mean daily air temperature (MDAT), mean daily air humidity (MDAH), mean daytime air temperature (MDtAT), mean daytime air humidity (MDtAH), mean nighttime air temperature (MNtAT), and mean nighttime air humidity (MNtAH) were calculated. 'Daytime' is defined as the time interval between 7 a.m. and 7 p.m., while 'nighttime' is the interval between 7 p.m. and 7 a.m. Microclimate measurements were carried out after a dry period, under clear weather conditions.

2.3. Analysis

Percentage frequencies for the species were determined with the JUICE 7.0.25 program (*Tichý*, 2002). After testing normality, one-way ANOVA and subsequent Tukey's HSD post hoc tests were applied in order to reveal the differences in species number between the different habitats, using the stats package of R 2.10.1 (*R Development Core Team*, 2009).

Detrended correspondence analysis (DCA) (*Hill* and *Gauch*, 1980) was used to detect the major gradients of floristic variation of the plots within the study sites. DCA is an ordination technique, which is able to identify gradients in community composition. Its advantage over other unconstrained ordination methods is that it is theoretically free from the so-called 'arch effect', thus, DCA axes correspond better to gradients with high turnover (*Legendre* and *Legendre*, 1998). The procedure was computed using Past 1.18 (*Hammer et al.*, 2001).

Variation of species presence/absence data was related to temperature and humidity measurements using distance-based redundancy analysis (db-RDA) (*Legendre* and *Anderson*, 1999). db-RDA is an ordination method, which arranges data objects in a space defined by the linear combinations of explanatory (environmental) variables and, at the same time, quantifies the variation in species composition explained by the environmental variables. The variation of species composition in db-RDA has to be expressed on the basis of a dissimilarity measure between pairs of community sample units. Here we applied the complement of Sörensen index as a dissimilarity measure, with the formula

$$D_{\text{Sörensen}}=1-2*a/(2*a+b+c),$$

where a is the number of species present in both members of the pair, b and c are the number of species present in one and the other plot (*Legendre* and *Legendre,* 1998). Considering our previous results (*Bátori et al.* 2011), the following measurements were used as explanatory variables: MDAT, MDtAT, MNtAT, MDAH, MDtAH, and MNtAH. For each study site, the gross effect of each climatic variable was calculated by constructing a db-RDA model with the tested variable as the only predictor and the compositional data as the dependent variables (hereafter called 'one-predictor model'). Effect strengths of each climatic variable were quantified by the percentage explained variance and F value of the respective db-RDA model, and their significance was assessed by a permutation test (see *Table 1*). Then, for each study site, the most effective temperature and humidity variables were selected based on the lowest P and the highest F values. With these two as background variables, a new db-RDA was performed ('two-predictor model') in order to assess the cumulative effect of the best climatic variables (see *Table 2*). There was high collinearity within temperature variables and humidity variables, thus, the other 2–2 variables of

these climatic factors were not involved in the model. 'Two-predictor models' were visualized on biplots. Ordinations were performed using the vegan R package (*Oksanen et al.*, 2009; *R Development Core Team*, 2009).

Moreover, we also used the coenological preferences of the plant species (*Soó*, 1980) to characterize each habitat.

Table 1. Summary statistics for the 'one-predictor' db-RDA models. MDAT: mean daily air temperature, MDtAT: mean daytime air temperature, MNtAT: mean nighttime air temperature, MDAH: mean daily air humidity, MDtAH: mean daytime air humidity, MNtAH: mean nighttime air humidity

Predictors	Var. %	F value	P value
	Mecsek Mountains: sinkhole		
MDAT	18.7	9.160	<0.001
MDtAT	17.5	8.478	<0.001
MNtAT	17.7	8.592	<0.001
MDAH	16.8	8.039	<0.001
MDtAH	14.9	7.028	<0.001
MNtAH	16.7	7.994	<0.001
	Bugac: sand-dune slack		
MDAT	32.5	5.071	<0.005
MDtAT	24.1	3.387	<0.05
MNtAT	30.2	4.560	<0.005
MDAH	34.8	5.578	<0.001
MDtAH	31.9	4.935	<0.001
MNtAH	29.0	4.328	<0.005

Table 2. Summary statistics for the 'two-predictor' db-RDA models. MDAT: mean daily air temperature, MDAH: mean daily air humidity

Predictors	Var. %	F value	P value
	Mecsek Mountains: sinkhole		
MDAT + MDAH	21.0	6.249	<0.001
	Bugac: sand-dune slack		
MDAT + MDAH	37.8	3.342	<0.005

3. *Results*

3.1. Microclimate and flora of the karst sinkhole

The MDAT changed from 19.9 to 17.6 °C along a microclimatic gradient in the sinkhole (*Fig. 2).*

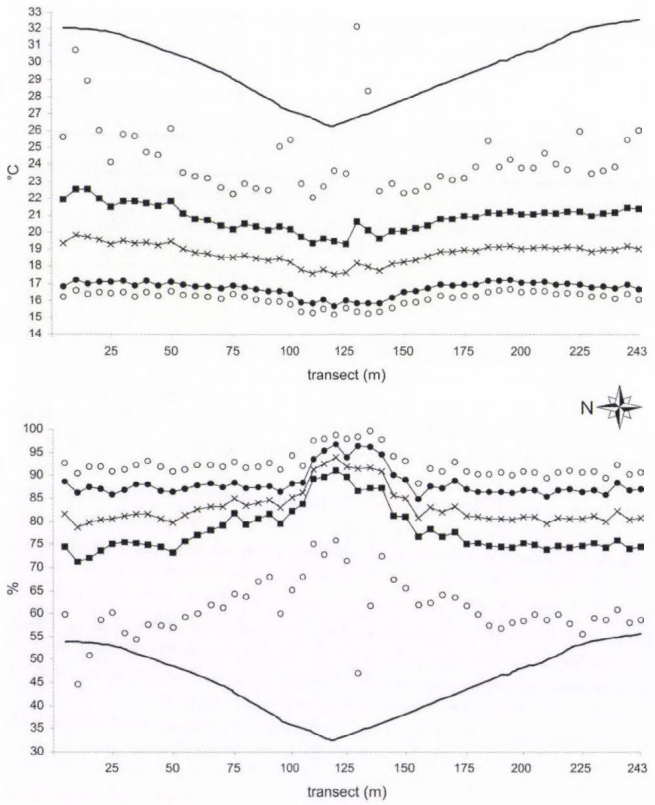

Fig. 2. Air temperature and air humidity values along the transect of the sinkhole of the Mecsek Mountains (August 9–10, 2010). Notations: ○: minimum and maximum air temperature (DMinAT, DMaxAT) and air humidity (DMinAH, DmaxAH) values; ■: mean daytime air temperature (MDtAT) and air humidity (MDtAH) values; ×: mean daily air temperature (MDAT) and air humidity (MDAH) values; ●: mean nighttime air temperature (MNtAT) and air humidity (MNtAH) values.

The maximum MDAT (19.9 °C) was detected in a plot of the south-facing rim where the transition between a turkey oak-sessile oak forest and an oak-hornbeam forest situated consisting of many dry oak forest and mesic oak forest species. The lowest MDAT (17.6 °C) and the DMinAT (15.1 °C) were recorded

on the bottom of the sinkhole, under the ravine forest. The MNtAT and MDtAT showed a very similar pattern, however, the DMaxAT (32.1 °C) was detected on the bottom of the sinkhole. Air humidity values also changed markedly along the transect with the lowest MDAH (79%) on the higher zone of the sinkhole slopes and with the highest MDAH (94%) in the sinkhole bottom (*Fig. 2*). The rest of the air humidity values followed a similar pattern. The 24-hour pattern of air temperature and air humidity also differed markedly between the upper sinkhole slopes and the sinkhole bottom (*Figs. 3–4*).

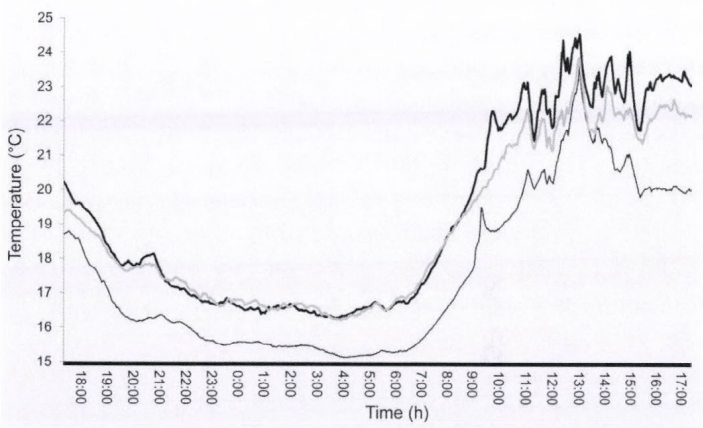

Fig. 3. Air temperature values in three plots along the transect (south-facing sinkhole slope: thick black line; sinkhole bottom: thin line; north-facing sinkhole slope: thick grey line) of the sinkhole of the Mecsek Mountains, measured over a 24-hour period (August 9–10, 2010).

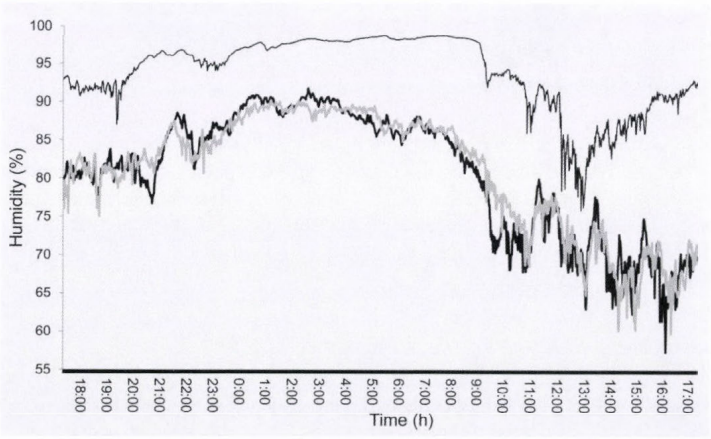

Fig. 4. Air humidity values in three plots along the transect (south-facing sinkhole slope: thick black line; sinkhole bottom: thin line; north-facing sinkhole slope: thick grey line) of the sinkhole of the Mecsek Mountains, measured over a 24-hour period (August 9–10, 2010).

The most frequent (>80%) species were *Fraxinus excelsior* L. on the upper sinkhole slopes and *F. excelsior* and *Galeobdolon luteum* s.l. on the sinkhole bottom. Species that occurred only in the sinkhole bottom include *Aconitum vulparia* Rchb., *Athyrium filix-femina* (L.) Roth, *Atropa belladonna* L., *Carex sylvatica* Huds., *Circaea lutetiana* L., *Dryopteris filix-mas* (L.) Schott, *Eupatorium cannabinum* L., *Paris quadrifolia* L., *Polystichum aculeatum* (L.) Roth, *P. setiferum* (Forssk.) Woyn., *Pyrus pyraster* (L.) Burgsd., *Rubus fruticosus* agg., *Solanum dulcamara* L., *Stachys sylvatica* L., *Urtica dioica* L., and *Veronica montana* L. According to the ANOVA, species number in the upper slopes and in the sinkhole bottom did not differ significantly (P=0.710). The proportions of the different species groups are shown in *Fig. 5*. Species of mesic oak forests (38%) and Central European beech forests (40%) had the highest proportions on the sinkhole slopes, but species of dry oak forests (9%) and Illyrian beech forests (9%) also had an important role in structuring the plant communities. The sinkhole bottom was covered mainly by beech forest species (54%), but the proportions of mesic oak forest species (14%) and indifferent species (12%) were also considerable. It is important to note that the sinkhole bottom held some species of deep ravines and gorges (e.g., *Aconitum vulparia* and *Polystichum aculeatum*) (2%), which were restricted to them.

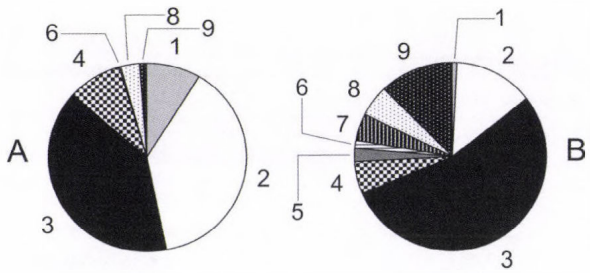

Fig. 5. Proportions of the different species groups of the sinkhole slopes (A) and of the sinkhole bottom (B). 1: species of dry oak forests; 2: species of mesic oak forests; 3: species of Central European beech forests; 4: species of Illyrian beech forests; 5: species of deep ravines and gorges; 6: species of wet forests; 7: species of marshes; 8: weed species; 9: indifferent species.

3.2. Microclimate and flora of the sand-dune slack

Air temperature and air humidity changed markedly along the transect of Bugac (*Fig. 6*). The lowest MDAT (15.8 °C) was recorded in the bottom of the dune slack where a remainder of the association *Molinio-Salicetum rosmarinifoliae* occurred. The highest MDAT (20.2 °C) was recorded in the open sandy

grassland of the upper slope. MDtAt and MNtAT values showed a marked decrease from the slopes to the bottom indicating a clear temperature gradient between them. Air humidity showed an opposite pattern with the highest values (MDAH: 79%; MNtAH: 96%; MDtAH: 62%) in the bottom of the dune slack and the lowest values (MDAH: 64%; MNtAH: 81%; MDtAH: 42%) on the upper slopes. The 24-hour pattern of air temperature and air humidity also differed markedly between the upper dune slopes and the bottom of the dune slack (*Figs. 7–8*).

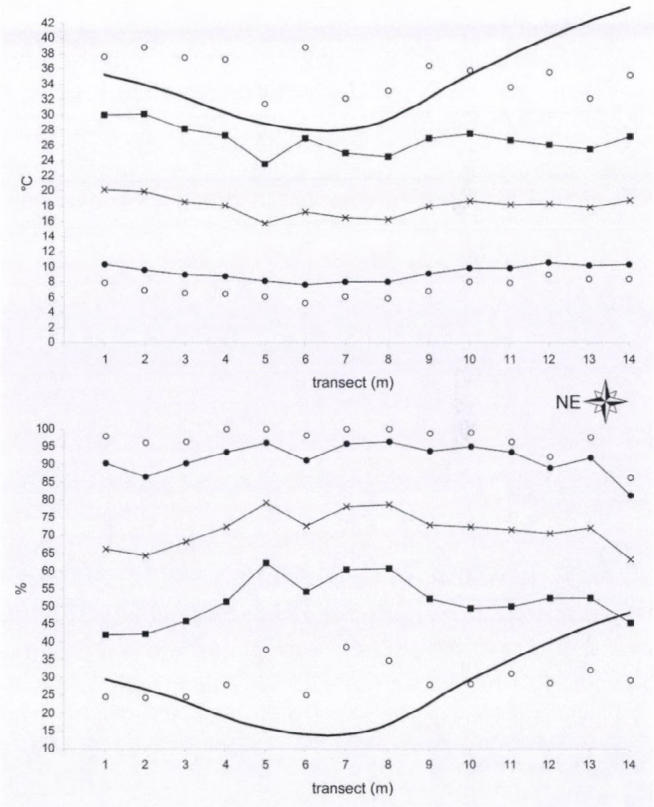

Fig. 6. Air temperature and air humidity values along the transect of the dune slack of Bugac (September 25–26, 2012). Notations: ○: minimum and maximum air temperature (DMinAT, DMaxAT) and air humidity (DMinAH, DmaxAH) values; ■: mean daytime air temperature (MDtAT) and air humidity (MDtAH) values; ×: mean daily air temperature (MDAT) and air humidity (MDAH) values; ●: mean nighttime air temperature (MNtAT) and air humidity (MNtAH) values.

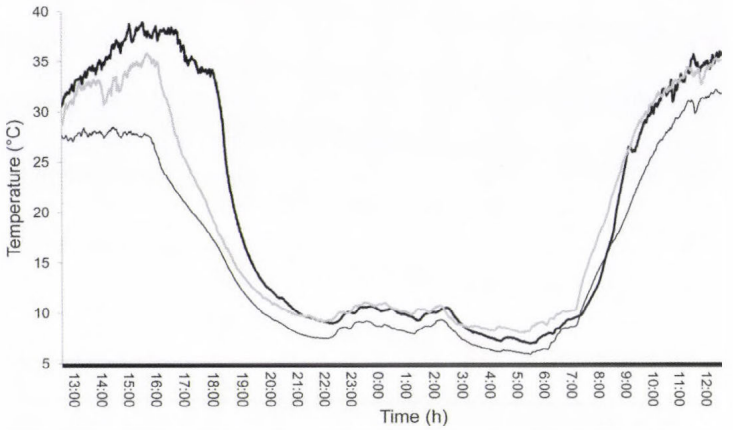

Fig. 7. Air temperature values in three plots along the transect (southwest-facing dune slope: thick black line; bottom of the dune slack: thin line; northeast-facing dune slope: thick grey line) of the dune slack of Bugac, measured over a 24-hour period (September 25–26, 2012).

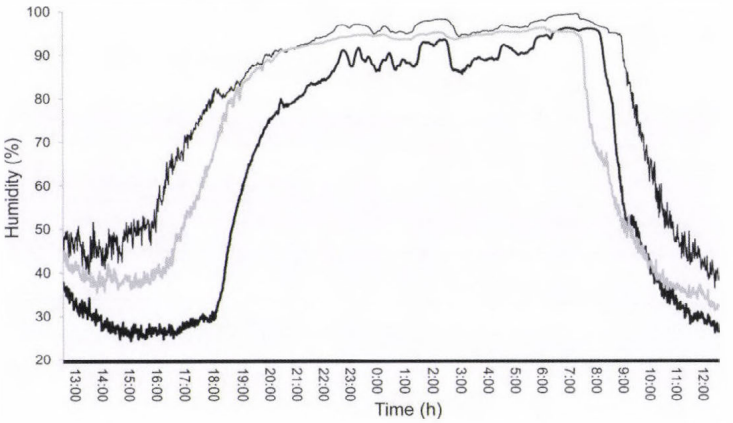

Fig. 8. Air humidity values in three plots along the transect (southwest-facing dune slope: thick black line; bottom of the dune slack: thin line; northeast-facing dune slope: thick grey line) of the dune slack of Bugac, measured over a 24-hour period (September 25–26, 2012).

Eryngium campestre L., *Festuca pseudovina* Hack., *Galium verum* L., *Stipa borysthenica* Klokov ex Prokudin, and *Thymus pannonicus* All. were the most frequent (>80%) species on the upper dune slopes, and *Carex liparicarpos* Gaudin, *Galium verum*, *Potentilla arenaria* Borkh., *Stipa borysthenica*, and

Thymus pannonicus in the bottom of the dune slack. Species that occurred only on the bottom of the dune slack include *Elymus repens* (L.) Gould, *Hieracium umbellatum* L., *Poa angustifolia* L., *Scirpoides holoschoenus* (L.) Soják, *Silene conica* L., *Salix rosmarinifolia* L. and *Trinia ramosissima* (Fisch.) W.D.J. Koch. According to the ANOVA, species number of the upper slopes and the dune slack did not differ significantly (P=0.245). Species of open sandy grasslands and closed sandy grasslands dominate all parts of the transect. However, fen species were only detected in the bottom of the dune slack with a proportion of 1.3% (*Fig. 9*).

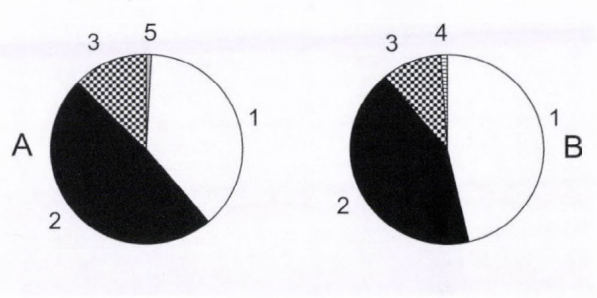

Fig. 9. Proportions of the different species groups of the dune slopes (A) and of the bottom of the dune slack (B). 1: species of closed sandy grasslands; 2: species of open sandy grasslands; 3: indifferent species; 4: fen species; 5: weed species.

3.3. Results of the multivariate analyses

The DCA-ordinations of the samples show a strong gradient along axis 1 with a very high species turnover in the sinkhole (eigenvalue: 0.63, gradient length: 4.4 S.D. units) and lower species turnover along the slopes of the dune slack (eigenvalue: 0.36, gradient length: 2.7 S.D. units).

The explanatory power of climatic variables in the 'one-predictor' db-RDA models is shown in *Table 1*. In Bugac, all of the 6 variables were significant, since they had P values under 0.001, 0.005, or 0.05, even though their F values varied considerably. In the Mecsek Mountains, there were minor differences among the variables in the explained variation, and all of them were found highly significant (<0.001). Both in Bugac and the Mecsek Mountains, MNtAT explained more variation of the vegetation than the daytime measurements, although the difference was negligible in the case of the Mecsek Mountains. MDAT had higher F values than MDtAT or MNtAT. Regarding air humidity, MDAH explained the most variation in both sites.

The 'two-predictor' models included MDAT and MDAH (*Figs. 10–11*). These models explained significant variation in both sites (*Table 2*).

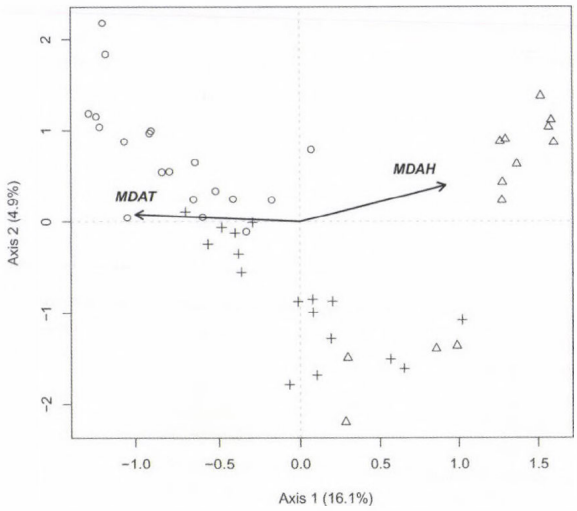

Fig. 10. Distance-based redundancy analysis diagram with 50 plots (○: plots of the south-facing sinkhole slope, +: plots of the north-facing sinkhole slope, △: plots of the sinkhole bottom) and environmental variables (MDAT: mean daily air temperature, MDAH: mean daily air humidity) of the Mecsek Mountains.

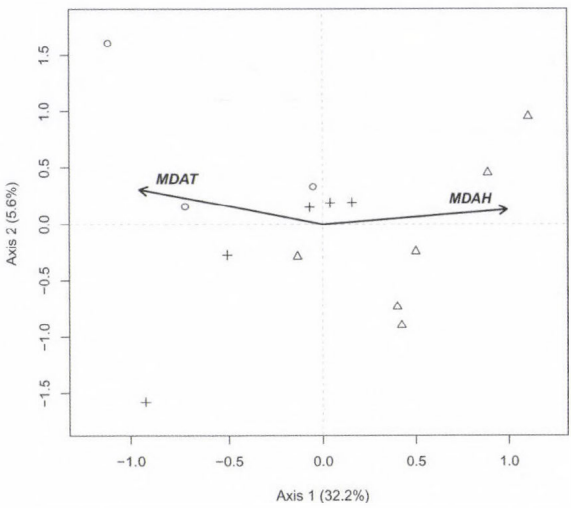

Fig. 11. Distance-based redundancy analysis diagram with 14 plots (○: plots of the southwest-facing dune slope, +: plots of the northeast-facing dune slope, △: plots of the bottom of the dune slack) and environmental variables (MDAT: mean daily air temperature, MDAH: mean daily air humidity) of Bugac.

4. Discussion

We studied the relationship between the spatial pattern of microclimatic parameters and the vegetation of natural habitat islands in Hungary. Our study yielded three main results. Firstly, the investigated habitat islands can be recognized as refugia for many species adapted to various climatic conditions. Secondly, the different elements of microclimate differently influenced the distribution of plant species. Thirdly, forest cover has a strong mitigating effect not only on air temperature but also on air humidity.

Previous studies showed that karst sinkholes may considerably affect the flora and vegetation of the karst surfaces (*Antonić et al.*, 2001; *Bátori et al.*, 2013; *Geiger*, 1950). As semi-isolated enclaves, lower sinkhole slopes and sinkhole bottoms are very important from a nature conservation point of view (*Bacsó* and *Zólyomi*, 1934; *Bátori et al.*, 2011; *Beck-Mannagetta*, 1906). Since they often harbor species that are very rare or missing from the surrounding habitats, they can be considered habitat islands (*Bátori et al.*, 2012b). We also found remarkable floristic differences between the bottom and the higher slopes of the investigated sinkhole. Many plants, in particular cool-adapted species, are restricted to the bottom of the sinkhole, where appropriate microclimatic conditions exist. The mean daily, daytime, and nighttime air temperature and air humidity values explained almost the same variation of species composition along the vegetation gradient. This is due to the mitigating effect of the forest, which reduces the differences between daytime and nighttime air temperatures and between daytime and nighttime air humidities at the same altitude (*Lehmann*, 1970; *Antonić et al.*, 1997). The extreme temperature value of the sinkhole bottom (DMaxAT: 32.1 °C) can be explained with the rate of canopy closure. Here, similarly to the ravine forests of deep valleys, frequent mass soil movements on the steep and wet slopes uproot trees allowing increased insolation through the sparse canopy. However, after this short high temperature period, the temperature of the sinkhole bottom decreased significantly, while the upper slopes remained warmer. Since karst surfaces are sensitive to climatic changes (*Loáiciga et al.*, 2000), sinkholes may play an essential role in reducing extinction rate of plant species, as they did in earlier geological times as well. The literature offers many excellent examples where sinkholes are mentioned as key habitats for cold-stage relicts and high mountain species (*Bátori et al.*, 2006; *Horvat*, 1953; *Lazarević et al.*, 2009). If we accept that the beech production optimum will shift in the future toward the pole and from lower elevation to higher elevation, and beech mortality risk will increase in its lower distribution range (*Hlásny et al.*, 2011; *Peñuelas et al.*, 2007; *Sykes* and *Prentice*, 1996), we can conclude that the beech forests of the Mecsek Mountains have a high chance of surviving in deep sinkholes for longer periods. In contrast, oak production and mortality seems almost insensitive to climate change in Central Europe, and in addition, the increasing oak production in elevations above 400 m a.s.l.

suggests a potential upward expansion of oak forests in the future (*Hlásny et al.*, 2011). This also means that the vegetation zones of sinkholes may shift toward the deeper sinkhole parts. This, in the worst scenario, would mean that vegetation types of the lowest parts (unable to shift even more downwards) may disappear from the sinkholes. A study by *Gargano et al.* (2010) on snow-bed vegetation of sinkholes has also showed that climate change would favor the replacement of snow-adapted species with the mesic ones occurring in surrounding habitats. In forest landscapes, climate-induced species replacement may be more striking if the forests are actively managed. Therefore, forest management should focus on maintaining forests not only in sinkholes but also in surrounding areas in order to moderate the potential impacts of climate change on karst surfaces.

Sand-dune slacks of the Kiskunság Sand Ridge play a similar role in preserving plant species as the karst sinkholes of mountain areas. Remnant patches of dune slacks have a high conservation value, since they support ancient steppe and fen vegetation with characteristic species such as *Carex flacca* Schreb., *Carex humilis* Leyss., *Chrysopogon gryllus* (L.) Trin., *Molinia caerulea* (L.) Moench, *Salix rosmarinifolia*, *Scirpoides holoschoenus*, *Schoenus nigricans* L., and *Thalictrum simplex* L. (*Borhidi*, 2012; *Molnár*, 2003). As our results revealed, microclimate is an important factor in structuring dune slack communities, although impacts of the nighttime and daytime air humidity and temperature values differ significantly (*Körmöczi et al.*, 1981). Although the investigated dune slack is much shallower than the karst sinkhole, its air humidity and temperature regimes are more extreme due to the large diurnal temperature variation, which can be explained by the different vegetation physiognomy. In the different parts of the world, several factors have been shown to contribute to the species composition changes of dune vegetation. The most important factors are the climate change- and human-induced drought (*Körmöczi*, 1991; *Muhs* and *Holliday*, 1995). Since the effect of precipitation and its spatial and temporal distribution are of great importance in xeric habitats (*Margóczi et al.*, 2007; *Thomas et al.*, 2005; *Yizhaq et al.*, 2009), the potential impact of precipitation decline on dune slack vegetation must be taken into consideration. For example, between 1981 and 1993, the average annual precipitation decreased by 16.7% on the Kiskunság Sand Ridge, causing a regional groundwater table decline (*Molnár et al.*, 2003). Apart from the climate change-induced drought, local human activities (e.g., afforestation, artesian and groundwater extraction, draining, hydrocarbon extraction, and intensive farming) also have had a strong negative influence on the groundwater table. A long-term vegetation study by *Tölgyesi* and *Körmöczi* (2012) revealed that both the wetter and drier sections of the dune fields of the Kiskunság are influenced by the water table decline, though most of the shifts were more prominent in the wet section (i.e., dune slack). The vegetation of the dune slack was getting more thermophilous, and its continental character was getting more pronounced. Since

climate change scenarios predict a significant temperature increase and a significant decrease in precipitation in summer for the Kiskunság Sand Ridge (*Bartholy et al.*, 2007), climate change could make the area even more vulnerable to drought and fire (*Blanka et al.*, 2013). Hence, conservation biologists must work on presenting arguments for policy makers and water management authorities in order to reduce the potential impact of drought on natural habitats of the Kiskunság.

As a summary, we have demonstrated the current and potential role of natural habitat islands in preserving different groups of plant species. According to our findings, the current vegetation of habitat islands is highly determined by the elements of microclimate, indicating the different importance of the daily, daytime, and nighttime humidity and temperature regimes. Presumably, these habitat islands will play an important role in mitigating species loss under future climate change. Probably the most important question in relation to the vegetation of natural habitat islands is how we can moderate and delay the impacts of climate change on species loss and vegetation replacement.

Acknowledgement—This research was supported by the TÁMOP-4.2.2/08/1/2008-0008 program of the Hungarian National Development Agency.

References

Allen, C.B., and *Burton, P.J.*, 1993: Distinction of soil thermal regimes under various experimental vegetation covers. *Can J Soil Sci 73*, 411–420.

Antonić, O., Hatic, D., and *Pernar, R.*, 2001: DEM-based depth in sink as an environmental estimator. *Ecol Model 138*, 247–254.

Antonić, O., Kušan, V., and *Hrašovec, B.*, 1997: Microclimatic and topoclimatic differences between the phytocoenoses in the Viljska Ponikva Sinkhole, Mt. Risnjak, Croatia. *Hrvatski Meteorološki Časopis 32*, 37–49.

Aude, E. and *Lawesson, J.E.*, 1998: Vegetation in Danish beech forests: the importance of soil, microclimate and management factors, evaluated by variation partitioning. *Plant Ecol 134*, 53–65.

Bacsó, N. and *Zólyomi, B.*, 1934: Mikroklíma és növényzet a Bükk-fennsíkon. *Időjárás 38*, 177–196. (in Hungarian)

Bartholy, J., Pongrácz, R., and *Gelybó, Gy.*, 2007: Regional climate change expected in Hungary for 2071-2100. *Appl Ecol Env Res 5*, 1–17.

Bátori, Z., Baráth, K., and *Csiky, J.*, 2006: *Dryopteris affinis* (Löwe) Fras.-Jenk. in the Mecsek Mountains. *Flora Pannonica 4*, 3–8. (in Hungarian)

Bátori, Z., Csiky, J., Erdős, L., Morschhauser, T., Török, P., and *Körmöczi, L.*, 2009: Vegetation of the dolines in Mecsek Mountains (South Hungary) in relation to the local plant communities. *Acta Carsologica 38*, 237–252.

Bátori, Z., Csiky, J., Farkas, T., Vojtkó, E. A., Erdős, L., Kovács, D., Wirth, T., Körmöczi, L., and *Vojtkó, A.*, 2013: The conservation value of karst dolines for vascular plants in woodland habitats of Hungary: refugia and climate change. *Int J Speleol 43*, 15–26.

Bátori, Z., Gallé, R., Erdős, L., and *Körmöczi, L.*, 2011: Ecological conditions, flora and vegetation of a large doline in the Mecsek Mountains (South Hungary). *Acta Bot Croat* 70, 147–155.

Bátori, Z., Erdős, L., and *Somlyay, L.*, 2012a: *Euphorbia prostrata* (*Euphorbiaceae*), a new alien in the Carpathian Basin. *Acta Bota Hung 54*, 235–243.

Bátori, Z., Körmöczi, L., Erdős, L., Zalatnai, M., and *Csiky, J.,* 2012b: Importance of karst sinkholes in preserving relict, mountain and wet woodland plant species under sub-Mediterranean climate: a case study from southern Hungary. *J Cave Karst Stud 74*, 127–144.

Beck-Mannagetta, G., 1906: Die Umkehrung der Pflanzenregionen in den Dolinen des Karstes. *Sitzungsberichte der Kaiserliche Akademie der Wissenschaften in Wien 65*, 3–4.

Begon, M., Townsend, C. R., and *Harper, J. L.,* 2006: Ecology: From Individuals to Ecosystems. Blackwell, Oxford.

Blanka, V., Mezősi, G., and *Meyer, B.,* 2013: Projected changes in the drought hazard in Hungary due to climate change. *Időjárás 117*, 219–237.

Borhidi. A., Kevey, B., and *Lendvai, G.,* 2012: Plant communities of Hungary. Akadémiai Kiadó, Budapest.

Dobrowski, S.Z., 2011: A climatic basis for microrefugia: the influence of terrain on climate. *Glob Change Biol 17*, 1022–1035.

Easterling, D.R., Meehl, G.A., Parmesan, C., Changnon, S.A., Karl, T.R., and *Mearns, L.O,* 2000: Climate extremes: Observations, modeling, and impacts. *Science 289*, 2068–2074.

Erdős, L., Gallé, R., Körmöczi, L., and *Bátori, Z.,* 2013: Species composition and diversity of natural forest edges: edge responses and local edge species. *Community Ecol 14*, 48–58.

Fetcher, N., Oberbauer, S.F., and *Strain, B.R.,* 1985: Vegetation effects on microclimate in lowland tropical forest in Costa Rica. *Int J Biometeor 29*, 145–155.

Forseth, I.N., and *Teramura, A.H.,* 1987: Field photosynthesis, microclimate and water relations of an exotic temperate liana, *Pueraria lobata*, kudzu. *Oecologia 71*, 262–267.

Gargano, D., Vecchio, G., and *Bernardo, L.,* 2010: Plant-soil relationships in fragments of Mediterranean snow-beds: ecological and conservation implications. *Plant Ecol 207*, 175–189.

Geiger, R., 1950: Das Klima der bodennahen Luftschicht: Ein Lehrbuch der Mikroklimatologie. Die Wissenschaft, 4. Verlag F. Vieweg and Sohn, Braunschweig. (in Deutsch)

Geiger, R. 1965: The climate near the ground. Harvard University Press, Cambridge.

Hammer, Ř., Harper, D. A. T., and *Ryan, P. D.,* 2001: PAST: Paleontological Statistics Software Package for Education and Data Analysis. Palaeontol Electron, http://palaeo-electronica.org/2001_1/past/issue1_01.htm.

Hampe, A. and *Jump, A.S.,* 2011: Climate relicts: Past, present, future. *Annu Rev Ecol Evol Syst 42*, 313–333.

Herrera, C.M., 1995: Microclimate and individual variation in pollinators: flowering plants are more than their flowers. *Ecology 76*, 1516–1524.

Hill, M. O., and *Gauch, H. G.,* 1980: Detrended correspondence analysis: an improved ordination technique. *Vegetatio 42*, 47–58.

Hlásny, T., Barcza, Z., Fabrika, M., Balázs, B., Churkina, G., Pajtík, J., Sedmák, R., and *Turčáni, M.,* 2011: Climate change impacts on growth and carbon balance of forests in Central Europe. *Clim Res 47*, 219–236.

Holl, K.D., 1999: Factors limiting tropical rain forest regeneration in abandoned pasture: seed rain, seed germination, microclimate, and soil. *Biotropica 31*, 229–242.

Horvat, I., 1953: Vegetacija ponikava. *Geografski Glasnik 14/15*, 1–25. (in Croatian)

Király., G., (Ed.) 2009: Új magyar füvészkönyv. Aggteleki Nemzeti Park Igazgatóság, Jósvafő. (in Hungarian)

Körmöczi, L., 1991: Drought-induced changes in a sandy grassland complex in the Great Hungarian Plain. *Acta Biol Szeged 37*, 63–74.

Körmöczi, L., and *Balogh, A.,* 1990: The analysis of pattern change in a Hungarian sandy grassland. In (*Krahulec, F., Agnew, A.D.Q., Agnew, S.,* and *Willems, H.J.* (Eds.)). Spatial processes in plant communities. Proceedings of the Workshop held in Liblice, 49–58.

Körmöczi, L., Bodrogközy, Gy., and *Horváth, I.,* 1981: Investigation of biological production and bioclimate of sandy grasslands in Bugac (Great Hungarian Plain between Danube and Tisza). *Acta Biol Szeged 27*, 55–69.

Lazarević, P., Lazarević, M., Krivošej, Z., and *Stevanović, V.,* 2009: On the distribution of *Dracocephalum ruyschiana* (Lamiaceae) in the Balkan Peninsula. *Phytologia Balcanica 15*, 175–179.

Legendre, P., and *Anderson, M.J.*, 1999: Distance-based redundancy analysis: testing multispecies responses in multifactorial ecological experiments. *Ecol Monogr 69*, 1–24.
Legendre, P., and *Legendre, L.*, 1998: Numerical Ecology. 2nd English edition. Elsevrier, Amsterdam.
Lehmann, A., 1970: Tarvágás által okozott ökológiai változások az abaligeti karszton. *Pécsi Műszaki Szemle 25*, 15–21. (in Hungarian)
Liu, X., Yin, Z.Y., Shao, X., and *Qin, N.*, 2006. Temporal trends and variability of daily maximum and minimum, extreme temperature events, and growing season length over the eastern and central Tibetan Plateau during 1961–2003. *J Geophys Res*: 111D19109.
Loáiciga, H.A., Maidment, D.R., and *Valdes, J.B.*, 2000: Climate-change impacts in a regional karst aquifer, Texas, USA. *Journal Hydrol 227*, 173–194.
Mantilla-Contreras, J., Schirmel, J., and *Zerbe, S.*, 2011: Influence of soil and microclimate on species composition and grass encroachment in heath succession. *J Plant Ecol-UK 5*, 249–259.
Margóczi, K., Szanyi, J., Aradi, E., and *Busa-Fekete, B.*, 2007: Hydrological background of the dune slack vegetation in the Kiskunság. *Ann Warsaw Univ of Life Sci – SGGW 38*, 105–113.
Marlatt, W. E., 1961: The interactions of microclimate, plant cover and soil moisture content affecting evapotranspiration rates. Atmospheric Science Technology Paper 23, Colorado State University, Fort Collins, Colorado.
Mohammed, A. R., and *Tarpley, L.*, 2009: High nighttime temperatures affect rice productivity through altered pollen germination and spikelet fertility. *Agr Forest Meteorol 149*, 999–1008.
Molnár, A., Tökölyi, J., Végvári, Zs., Sramkó, G., Sulyok, J., and *Barta, Z.*, 2012: Pollination mode predicts phenological response to climate change in terrestrial orchids: a case study from central Europe. *J Ecol 100*, 1141–1152.
Molnár, Zs., (Ed.) 2003: A Kiskunság száraz homoki növényzete. TermészetBÚVÁR Alapítvány Kiadó, Budapest. (in Hungarian)
Muhs, D. R., and *Holliday, V. T.*, 1995: Evidence of active dune sand on the Great Plains in the 19th century from accounts of early explorers. *Quaternary Res 43*, 198–208.
Müller, S.W., Rusterholz, H.P., and *Baur, B.*, 2006: Effects of forestry practices on relict plant species on limestone cliffs in the northern Swiss Jura mountains. *Forest Ecol Manag 237*, 227–236.
Oksanen, J., Kindt, R., Legendre, P., O'Hara, B., Simpson, G. L., Solymos, P., Stevens, M.H.M., and *Wagner, H.*, 2009: Stats Package and vegan: Community Ecology Package. R package version 2.10–1.
Oliver, S.A., Oliver, H.R., Wallace, J.S., Roberts, and *A.M.*, 1987: Soli heat flux and temperature variation with vegetation, soil type and climate. *Agr Forest Meteorol 39*, 257–269.
Parmesan, C., Root, T.L., and *Willig, M.R.*, 2000: Impacts of extreme weather and climate on terrestrial biota. *B Am Meteorol Soc 81*, 443–450.
Peñuelas, J., Ogaya, R., and *Boada, M.*, 2007: Migration, invasion and decline: changes in recruitment and forest structure in a warming-linked shift of European beech forest in Catalonia (NE Spain). *Ecography 30*, 830–838.
Pinke, Gy., Karácsony, P., Czúcz, B., Botta-Dukát, Z., and *Lengyel, A.*, 2012: The influence on environment, management and site context on species composition of summer arable weed vegetation in Hungary. *Appl Veg Sci 15*, 136–144.
R Development Core Team, 2009: R: A language and environment for statistical computing. R Foundation for Statistical Computing, Vienna, Austria. ISBN 3-900051-07-0, URL http://www.R-project.org.
Rasztovits, E., Móricz, N., Berki, I., Pötzelsberger, E., and *Mátyás, Cs.*, 2012: Evaluating the performance of stochastic distribution models for European beech at low-elevation xeric limits. *Időjárás 116*, 173–194.
Rich, P. M., and *Weiss, S. B.*, 1991: Spatial models of microclimate and habitat suitability: lessons from threatened species. Proceedings of the Eleventh Annual ESRI User Conference, Readlands: ESRI, 59–99.
Rijnsdorp, A.D., Peck, M.A., Engelhard, G. H., Möllmann, C., and *Pinnegar, J.K.*, 2009: Resolving the effect of climate change on fish populations. *ICES J Mar Sci 66*, 1570–1583.
Schwartz, M.W., Iverson, L.R., Prasad, A.M., Matthewa, S.N., and *O'Connorm, R.J.*, 2006: Predicting extinctions as a result of climate change. *Ecology 87*, 1611–1615.

Schimel, D.S., and *Parton, W.J.*, 1986: Microclimatic controls of nitrogen mineralization and nitrification in shortgrass steppe soils. *Plant Soil 93*, 347–357.

Shiu, C.J., Liu, S. C., and *Chen, J.P.*, 2009: Diurnally asymmetric trends of temperature, humidity, and precipitation in Taiwan. *J Climate 22*, 5635–5649.

Simon, T., (Ed.) 1991: Baktérium-, alga-, gomba-, zuzmó- és mohahatározó. Tankönyvkiadó, Budapest. (in Hungarian)

Simon, T., 2000. A magyarországi edényes flóra határozója. Nemzeti Tankönyvkiadó, Budapest. (in Hungarian)

Skyes, M.T., and *Prentice, I.C.*, 1996: Climate change, tree species distributions and forest dynamics: A case study in the mixed conifer/northern hardwoods zone of northern Europe. *Climatic Change 34*, 161–177.

Soó, R., 1980: A magyar flóra és vegetáció rendszertani-növényföldrajzi kézikönyve VI. Akadémiai Kiadó, Budapest. (in Hungarian)

Thomas, C.D., Cameron, A., Green, R.E., Bakkenes, M., Beaumont, L.J., Collingham, Y.C., Erasmus, B.F.N., de Siqueira, M.F., Grainger, A., Hannah, L., Hughes, L., Huntley, B., van Jaarsveld, A. S., Midgley, G.F., Miles, L., Ortega-Huerta, M.A., Peterson, A.T., Phillips, O.L., and *Williams, S.E.*, 2004: Extinction risk from climate change. *Nature 427*, 145–148.

Thomas, D.S.G., Knight, M., and *Wiggs, G.F.S.*, 2005: Remobilization of southern African desert dune systems ba twenty-first century global warming. *Nature 435*, 1218–1221.

Tichý, L., 2002: JUICE, software for vegetation classification. *J Veg Sci 13*, 451–453.

Tölgyesi, Cs. and *Körmöczi, L.*, 2012: Structural changes of a Pannonian grassland plant community in relation to the decrease of water availability. *Acta Bot Hung 54*, 413–431.

Turlure, C., Choutt, J., Baguette, M., and *van Dyck, H.*, 2010: Microclimatic buffering and resource-based habitat in a glacial relict butterfly: significance for conservation under climate change. *Glob Change Biol 16*, 1883–1893.

Unger, J., 1999: Comparisons of urban and rural bioclimatological conditions in the case of a Central-European city. *Int J Biometeorol 43*, 139–144.

Walther, G., Post, E., and *Convey, P.* 2002: Ecological responses to recent climate change. *Nature 416*, 389–437.

Whiteman, C.D., Haiden, T., Pospichal, B., Eisenbach, S., and *Steinacker, R.* 2004: Minimum temperatures, diurnal temperature ranges, and temperature inversion in limestone sinkholes of different sizes and shapes. *J Appl Meteorol 43*, 1224–1236.

Xu, M., Qi, Y., Chen, J., and *Song, B.*, 2004: Scale-dependent relationship between landscape structure and microclimate. *Plant Ecol 173*, 39–57.

Yizhaq, H., Ashkenazy, Y., and *Tsoar, H.*, 2009: Sand dune dynamics and climate change: A modeling approach. *J Geophys Res 114*: F01023.

Appendix

Table A1. Species composition (presence/absence data) of the plots along the sinkhole transect of the Mecsek Mountains

Part.1.

Plots	**1**	**2**	**3**	**4**	**5**	**6**	**7**	**8**	**9**	**10**	**11**	**12**	**13**	**14**	**15**	**16**	**17**	**18**	**19**
Species / Sinkhole	**South-facing rim and slope**																		
Acer campestre						1													
Acer platanoides											1								
Acer pseudoplatanus								1											1
Aconitum vulparia																			
Ajuga reptans							1											1	
Alliaria petiolata												1				1			
Arabis turrita																			
Asarum europaeum						1	1	1								1	1	1	1
Athyrium filix-femina																			
Atropa belladonna																			
Brachypodium sylvaticum		1	1																
Bromus ramosus agg.			1				1		1										
Campanula rapunculoides	1	1				1													
Cardamine impatiens																			
Carex pilosa	1	1	1	1	1	1	1	1	1	1	1	1	1			1	1	1	
Carex sylvatica																			
Carpinus betulus		1				1	1	1	1			1	1	1	1	1		1	1
Circaea lutetiana																			
Clematis vitalba																			1
Clinopodium vulgare							1												
Convallaria majalis			1																
Crataegus laevigata																			
Dactylis polygama	1	1	1	1	1	1	1	1	1			1							1
Dryopteris filix-mas																			
Eupatorium cannabinum																			
Euphorbia amygdaloides	1		1	1		1	1		1										
Fagus sylvatica														1	1			1	1
Fallopia dumetorum		1																	1
Festuca drymeja				1		1	1			1	1	1	1	1	1	1			
Fraxinus excelsior				1		1	1	1	1	1	1	1	1	1	1	1	1	1	1
Fraxinus ornus	1	1	1	1	1	1	1	1	1		1		1	1	1				
Galeobdolon luteum s.l.																		1	
Galium aparine					1										1	1			
Galium odoratum																		1	
Galium schultesii	1																		
Geranium robertianum																			
Geum urbanum																			
Glechoma hirsuta					1														
Hedera helix	1			1	1	1	1	1	1		1						1	1	
Helleborus odorus	1		1																1
Hepatica nobilis			1																
Lathyrus venetus											1						1	1	

Plots	1	2	3	4	5	6	7	8	9	10	11	12	13	14	15	16	17	18	19
Species / Sinkhole	**South-facing rim and slope**																		
Lathyrus vernus		1															1	1	
Ligustrum vulgare		1		1	1		1												
Luzula forsteri														1					
Melica uniflora	1	1	1	1	1	1	1	1	1	1	1	1	1		1	1	1	1	1
Mercurialis perennis																			1
Milium effusum																			
Moehringia trinervia																			
Mycelis muralis																			
Paris quadrifolia																			
Polygonatum multiflorum	1			1												1	1	1	
Polystichum aculeatum																			
Polystichum setiferum																			
Primula vulgaris																		1	
Pyrus pyraster																			
Quercus cerris				1		1													
Quercus petraea agg.					1	1				1	1	1							1
Rosa arvensis	1	1	1	1															
Rubus fruticosus agg.																			
Rubus hirtus																			
Rumex sanguineus																			1
Ruscus hypoglossum																			
Sambucus nigra																			1
Solanum dulcamara																			
Sorbus torminalis					1														
Stachys sylvatica																			
Stellaria holostea	1	1	1	1		1	1	1	1	1	1					1	1	1	1
Symphytum tuberosum	1																		
Tilia tomentosa						1	1	1	1	1	1	1	1	1	1	1	1		
Urtica dioica																			
Veronica montana																			
Viola alba							1												
Viola reichenbachiana							1												

Table A1. (cont.)

Part. 2.

Plots	20	21	22	23	24	25	26	27	28	29	30	31	32	33	34	35	36	37	38	39	40	41	42	43	44	45	46	47	48	49	50
Species / Sinkhole	**Bottom**													**North-facing rim and slope**																	
Acer campestre			1																										1		
Acer platanoides																										1	1	1			
Acer pseudoplatanus	1		1			1	1	1	1	1					1	1															
Aconitum vulparia		1																													
Ajuga reptans																															
Alliaria petiolata		1								1	1			1		1							1			1	1	1	1	1	1

Plots	20	21	22	23	24	25	26	27	28	29	30	31	32	33	34	35	36	37	38	39	40	41	42	43	44	45	46	47	48	49	50
Species / Sinkhole	**Bottom**													**North-facing rim and slope**																	
Arabis turrita																										1					
Asarum europaeum		1	1			1	1			1	1				1	1										1	1	1	1	1	
Athyrium filix-femina			1			1	1	1	1	1																					
Atropa belladonna	1					1	1	1																							
Brachypodium sylvaticum			1		1																										
Bromus ramosus agg.						1																						1	1		
Campanula rapunculoides																															
Cardamine impatiens			1																								1	1			1
Carex pilosa																										1	1	1	1	1	1
Carex sylvatica							1																								
Carpinus betulus			1			1	1																								
Circaea lutetiana	1			1	1		1	1		1																					
Clematis vitalba	1					1																									
Clinopodium vulgare																															
Convallaria majalis																															
Crataegus laevigata																															1
Dactylis polygama																											1				
Dryopteris filix-mas			1		1			1	1	1	1																				
Eupatorium cannabinum	1						1	1	1																						
Euphorbia amygdaloides																										1					
Fagus sylvatica																	1														
Fallopia dumetorum																										1					1
Festuca drymeja																															
Fraxinus excelsior	1	1	1	1	1	1	1	1	1		1	1		1	1	1	1		1	1	1		1	1	1	1	1	1	1	1	1
Fraxinus ornus														1					1	1	1	1	1	1	1	1	1	1	1	1	1
Galeobdolon luteum s.l.	1	1	1	1	1	1	1	1	1	1	1	1	1	1	1		1			1	1		1	1	1	1	1		1	1	1
Galium aparine	1			1																											
Galium odoratum										1					1																
Galium schultesii																												1			
Geranium robertianum										1																1		1			
Geum urbanum																															1
Glechoma hirsuta																															
Hedera helix											1	1	1				1						1				1	1	1		
Helleborus odorus		1	1										1			1									1						
Hepatica nobilis																															1
Lathyrus venetus																															
Lathyrus vernus																											1		1		
Ligustrum vulgare																										1			1	1	1
Luzula forsteri																															
Melica uniflora																										1	1	1	1	1	1
Mercurialis perennis	1		1	1	1	1									1	1	1	1				1				1	1	1	1	1	1
Milium effusum																													1		
Moehringia trinervia						1																						1	1		
Mycelis muralis																										1					
Paris quadrifolia				1																											
Polygonatum multiflorum																															
Polystichum aculeatum						1	1																								
Polystichum setiferum			1																												
Primula vulgaris																															

Plots	20	21	22	23	24	25	26	27	28	29	30	31	32	33	34	35	36	37	38	39	40	41	42	43	44	45	46	47	48	49	50
Species / Sinkhole	**Bottom**													**North-facing rim and slope**																	
Pyrus pyraster	1																														
Quercus cerris																															
Quercus petraea agg.																									1						
Rosa arvensis																										1					
Rubus fruticosus agg.	1							1																							
Rubus hirtus						1	1		1																	1					
Rumex sanguineus	1	1																													
Ruscus hypoglossum												1				1	1						1								
Sambucus nigra					1	1																									
Solanum dulcamara								1	1																						
Sorbus torminalis																															
Stachys sylvatica			1	1	1		1		1																						
Stellaria holostea																												1	1	1	1
Symphytum tuberosum																															
Tilia tomentosa	1											1				1										1					
Urtica dioica	1	1	1	1	1	1	1	1	1	1																					
Veronica montana			1			1																									
Viola alba																															
Viola reichenbachiana																1													1		

Table A2. Species composition (presence/absence data) of the plots along the dune slack transect of Bugac

Plots	1	2	3	4	5	6	7	8	9	10	11	12	13	14
Species / Dune slack	**Southwest-facing slope**			**Bottom**						**Northeast-facing slope**				
Achillea pannonica			1	1			1	1	1	1	1	1	1	
Calamagrostis epigeios							1	1		1	1			
Carex liparicarpos			1	1	1	1	1	1	1	1	1	1	1	
Cladonia convoluta	1	1												
Cladonia furcata	1	1	1	1						1	1	1	1	1
Cladonia magyarica		1	1	1					1	1	1	1	1	1
Crepis rhoeadifolia											1		1	
Crepis setosa													1	
Cynodon dactylon	1	1										1		1
Dianthus pontederae		1	1		1			1		1	1		1	
Elymus repens								1						
Eryngium campestre	1	1	1	1						1	1	1	1	1
Erysimum diffusum										1				
Euphorbia cyparissias						1	1	1	1	1	1		1	
Euphorbia seguieriana							1	1					1	
Falcaria vulgaris												1	1	1
Festuca pseudovina	1	1	1	1		1		1	1	1	1	1	1	1
Festuca vaginata										1		1	1	1
Galium verum		1	1	1	1	1	1	1	1	1	1	1	1	1
Hieracium umbellatum								1	1					

Plots	1	2	3	4	5	6	7	8	9	10	11	12	13	14
Species / Dune slack	**Southwest-facing slope**			**Bottom**						**Northeast-facing slope**				
Kochia laniflora	1													
Koeleria glauca		1				1				1	1	1	1	1
Odontites rubra						1					1			
Phleum phleoides												1		
Poa angustifolia						1	1							
Potentilla arenaria		1	1	1	1	1	1	1	1	1	1	1	1	
Salix rosmarinifolia						1								
Scabiosa ochroleuca						1						1		1
Scirpoides holoschoenus						1	1							
Silene conica						1								
Silene otites			1	1	1			1			1			1
Stipa borysthenica	1	1	1	1	1	1	1	1	1	1	1	1	1	1
Stipa capillata				1	1			1	1	1				1
Thymus pannonicus	1	1	1		1	1	1	1	1	1	1	1	1	
Tortula ruralis	1	1	1	1	1									
Tragopogon dubius			1				1	1			1			
Trinia ramosissima				1				1	1					
Verbascum lychnitis		1	1	1	1				1					1

IDŐJÁRÁS

Quarterly Journal of the Hungarian Meteorological Service
Vol. 118, No. 3, July – September, 2014, pp. 283–291

Impacts of extreme weather in supply chains

Zoltán Kovács and **Beáta Sz. G. Pató***

University of Pannonia, Department of Supply Chain Management
Veszprém, Egyetem u. 10, H-8200, Hungary

**Corresponding author E-mail: patog@vnet.hu*

(Manuscript received in final form March 10, 2014)

Abstract—There are many phenomena which confirm the fact of climate change. Two kinds of responses are mentioned often to this fact: 1. Actions by which this process can be interrupted or slowed down. 2. Accepting the fact of changes and finding adaptive strategies.

Authors present a research which aimed to increase the responsiveness of supply chains for the climate change – especially extreme weather. Secondary and primary investigation were carried out, and the nominal group technique was used to discover, group and assess the potential threats.

Results so far pointed out that both physical and control processes are involved in extreme whether consequences. Findings give good bases for a substantial risk analysis for any disaster coming from the climate change or other reasons.

The research is supported by the Government of Hungary.

Key-words: Climate change, disaster management in supply chains, extreme weather.

1. Introduction

Extreme weather event might cause wide range of problems in everyday life. While there is a debate on the fact of climate change (*Nordhaus*, 2013) and its possible source, there is no doubt that being ready for unexpected weather evens is not a bad decision. There are studies which deal with the source and implications of extreme weather.

Stott et al. (2004), in their pioneering study, concluded that human influence more than doubled the likelihood of the heat wave occurring. An

OECD study (*Agrawala et al.*, 2011) discovered that while companies are generally aware of the physical implications of climate change, few include it into their risk management system.

From this point of view, there are two possible strategies:

1. To reduce the climate change effects – mostly emission – in order to slow down or to turn back the negative trend. We have to be aware that outcomes of corrective and preventive actions will show up in middle or long time horizon.

2. To learn to live with climate change at least on middle range and to do our best to adapt to the situation.

Weather sensitive sectors such as agriculture, horticulture, food industries are involved mostly. *Thorpe* and *Fennel* (2012) present three case studies from coffee, cotton, and sesame oil business. Since supply is vital in wide area of society and life, it is important to examine the implications of climate change. The effects can have influence in direct and indirect ways.

Present youngsters are the most involved in the consequences of climate change. In the State of the Union speech, President Obama urged Congress "to get together, pursue a bipartisan, market-based solution to climate change, like the one John McCain and Joe Lieberman worked on together a few years ago." In his second inauguration speech (January, 2013), the president said: "We will respond to the threat of climate change, knowing that failure to do so would betray our children and future generations. Some may still deny the overwhelming judgment of science, but none can avoid the devastating impact of raging fires, and crippling drought, and more powerful storms."

The topic is especially relevant in Hungary, since we faced some extreme weather events recently, such as extreme temperature, excessive rainfall, flooding, and spring snowstorms.

Recognizing this and the fact that certain aspects of climate change issues are inevitable, University of Pannonia defined a project to carry out research on consequences of climate change, especially weather phenomena issues. Economics, agriculture, engineering, and social science researchers work in the project supported by the EU and the Hungarian government.

Inside economics, the main analyzed areas are: macroeconomics, regional development, tourism, health sector, and supply chains. Part of the research is a literature review, such as we introduced above. The other part is primary research, in first stage mostly forecast.

First we tried to discover a wide set of implications. The method we have used is the nominal group technique.

In our research we asked master level students – who are in supply chain related programs – about their judgments on the possible consequences of climate change, especially extreme weather.

2. *Literature review*

The main research question was to learn the opinion of next generation about weather change implications in supply chains.

According to *International Energy Agency* (2013), it is possible that global warming will be more than two degrees Celsius. Above this limit the climate could become unstable. This will affect production and transport processes as well. *Carey* (2011) suggests that extreme weather events have become more common in recent years.

Czifra, et al. (2013) argue that climate change affects competitiveness.

According to IPCC's annual report (*Trenberth*, 1999), Hungary is acutely vulnerable. Based on this forecast climate change will turn the weather towards extreme events. The temperature will be higher than it is now, and we can expect stormy winters with more fall (*Czifra, et al.*, 2013).

In Hungary one of the main supply related implications will be the deterioration of transport infrastructure. Extreme weather phenomena such as storm, flooding, high temperature, lots of fall will cause damages in transport infrastructure. *Hunyadi* (2010) gives examples for possible damages of road infrastructure. *Gáspár* (2003, 2004) has set up road durability requirements. He suggests that the requirement pyramid (*Fig. 1*) will change in the future as a respond to climate change.

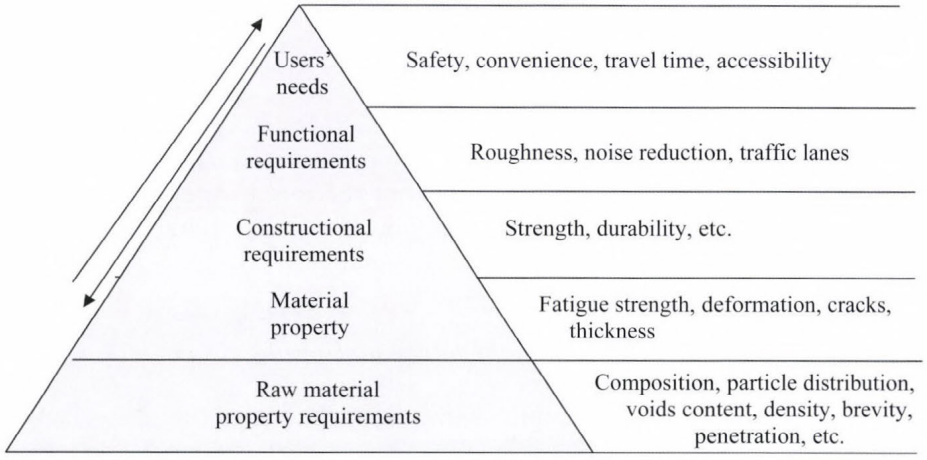

Fig. 1. Surface performance requirement related pyramid of requirements (*Gáspár*, 2003)

Hunyadi (2010) argues planting vegetation near the roads which have larger tolerance limits, in order to take consideration the effects of climate change in advance. *Gáspár* (2003) suggests life cycle design:"life cycle design includes both design methods and their phases which take into consideration economic issues, cultural integration and ecological aspects".

In addition to the environmental impacts on supply chains, there is an other important factor: restructuring of customer needs. Production infrastructure and distribution networks have to adjust to them (*Czifra et al*, 2013).

Caldwell et al. (2013) and others (*Thrope* and *Fennel*, 2012) examined the potential impacts of climate change to freight transport. *Table 1* summarizes the direct and indirect effects of meteorological factors on terrestial traffic safety.

Jüttner et al. (2003) give an overview of the potential research areas.

Table 1. Effects of weather on surface traffic safety (*Vissy* and *Bátyi*, 1998)

Surface conditions (road, rail)	**Direct effects**		**Indirect effects**	
	Visibility	**Loading**	**Biometeorological effects (front effects)**	
Snowing	Fog	Wind	Accident prevention	Health and safety
Snowdrift	Heavy rainfall	Heavy rainfall		
Temperature				

There are relatively small number of researches on the opinion of the future generation, however, *Revesz* and *Shahabian* (2010) evaluate opportunities for intergenerational discounting, which are often conflated in the literature. They have found that the existing justifications do not support the prevalent approach of discounting benefits to future generations at the rate of return in financial markets and, more generally, that discounting cannot substitute for a moral theory setting forth our obligations to future generations.

3. Research methodology and results

As previous studies from literature show, implications of climate changes include wide areas of supply chains. We can say that the whole society is involved in the climate change, partly due to the effects in supply chains. There are different ways to discover opinions on the topic.

Zaltman et al. (1982) and *Yin* (1994) used discovery oriented, practitioner-based approach, with semi-structured interviews.

The nominal group technique (NGT) is a group-based problem solving or decision making method (*Delbecq* and *VandeVen*, 1971, 1975; *VandeVen* and *Delbecq*, 1974). It combines the amenities of the un/low structured brainstorming and formal voting. We have followed the next steps:

1. Introduction and explanation: We welcomed the participants, who were master students in logistics, management, MBA and industrial engineering. We provided the question in written form on the top of an A4 format page: *What are the impacts of extreme weather to the operation of supply chains?* We have raised participants' attention to the importance of the question.

2. Silent generation of ideas: We asked participants to put down possible answers to the paper. Since any interaction is prohibited, in this phase we asked them not to consult or discuss their ideas with others. This stage lasted 10 minutes. In this stage, we repressed not only negative but useful positive interactions also. We allowed them in next steps.

3. Sharing ideas: We invited participants to read their ideas they have written on the paper. If they ran out of idea, they could 'pass'. If they have new idea – generated by others – they can join again. They can further develop others' ideas. We recorded each idea into a spreadsheet using the same words as participants formulated their ideas. (They were asked to use not more than 3 words to compose their idea.)

   The round robin process continued until all ideas have been presented. Since this phase supports only positive interaction, they could hear each other but were not allowed to comment others' ideas.

4. Discussion: Participants were invited to seek verbal explanation or further details about any of the ideas that others have produced that may not be clear to them. Anybody could ask, comment, interpret, explain any ideas on the screen. New ideas were generated, others were combined, extended or deleted (when they are proved to be equal with others: they called duplicates). There are two dangers in this stage (based on our more than 30 years NGT experiences):

   — Drawing together ideas might result so-called 'super idea' which will get lots of votes but is not concrete at all, thus, it can not be made real. Sometimes 'super idea' and some of its parts exist simultaneously.

   — There will be similar good ideas, which will compete again each other and share votes. In this way, each of them gets little weight and will drop out.

   It is important for the facilitator to keep good balance in the weight of ideas. Such aspects are complexity, extent, related hierarchy level of ideas. In this stage, we have received the list of possible effects in *Table 2*.

Table 2. List of potential effects after group discussion

1	Product damage
2	Communication problems in the EDI
3	Damage of factories
4	Routes are cancelled
5	Extreme work conditions
6	Other modal transport are forced
7	Cost, time, and resource losses
8	Low water-sailing ban
9	Increased preparations in the case of FMCG products
10	Huge storm - closed airports
11	Increased transport (supply) uncertainty
12	Additional storage costs
13	Appreciation of reliability models due to increased uncertainty
14	Increased number of risk factors
15	Increased costs of mining, excavating raw materials
16	Increased transport time requirement
17	Companies that fall out of the supply chains
18	Electric grid dropouts complicate storing
19	Necessity of work reorganization
20	Increased mental and physical load of labour
21	Higher vulnerability of electronic products, lower humidity during winter
22	Loss of goodwill due to delays and damages
23	Lack of agricultural products
24	Physical delivery becomes impossible
25	Difficult traffic conditions due to flooding
26	Development of resistant packaging
27	Railway comes to the fore
28	Coming out supply chain issues
29	Profile change is necessary (products)
30	Maintaining higher inventory
31	Accidents
32	Maintaining crisis staff
33	Alternative supply seeking
34	Further company social responsibilities
35	More pressure on co-operation, collaboration
36	Earthquake abyss engulfes the company
37	Daily 8-hour work period may be fragmented
38	Increasing number of non-forecasted transport errors
39	Closer relocation of supply chain players
40	Introduction of stricter limitations
41	Establishing specialized warehouses
42	Conflicts between partners
43	Consumer needs can not be satisfied
44	Material flow slows
45	More dense distribution points, necessity for warehouses
46	Shutdown due to state of emergency
47	Appreciation of taking out insurance
48	Good condition tires can not be calculated
49	Market rankings change
50	Development of vehicles
51	Needs assessment difficulties
52	IT equipment damage
53	Stress
54	Longer delivery lead times
55	Shipments over Arctic can not be solved
56	Decentralized inventory management
57	Necessity of rationalization
58	Increased energy consumption
59	Appreciation of meteorological information
60	Weakening of political stability
61	Growing importance of forecasts
62	Obstruction in mining
63	Rails freezing
64	Shifted seasonality
65	Appreciation of products with longer warranty period
66	Chain problems accumulate
67	Increasing weight of security/safety technology
68	Need for special storage conditions
69	Changes in priorities within the company
70	Co-operation with the army
71	Importance of loading and fastening technology
72	Rail deformation

5. Ranking: In this session there were little, spontaneous and informal interaction between participants. They were busy with their voting papers and selecting the most preferred ideas.
First they were asked to select the 5 most important effects from the list of 72. Then they ranked them. The ranking order was: 1 – 5 – 2 – 4 – 3 where 5 was the grade of the most important, 1 is the grade of least important one.
Finally, the grade points were summarized for all effects in the list of 72 ideas. *Table 3* shows the final ranks of the effects.
Then we summarized the grade points.

Table 3. The final ranks

Rank	Potential effects	Score
1.	Increased transport (supply) uncertainty	22
2.	Cost, time and resource losses	21
3.	Routes are cancelled	15
4.	Damage of factories	12
5.	Accidents	11
6-7.	Appreciation of reliability models due to increased uncertainty	10
6-7.	Maintaining crisis staff	10

4. Conclusions

Looking at the list we can conclude, that students have a realistic judgment on possible consequences of climate change, especially effects of extreme weather. It is especially important in Hungary where the frequency of extreme weather events is increasing, however, to put it cynically, they are tending to become not extreme ones.

We did not asked the participants about the 'to do's, it will be the part of further research. Based on their case studies *Thorpe* and *Fennel* (2012), using an EOCD study, suggest five possible actions:

1. Raise awareness and understanding of adaptation within the business: companies need to make more effort to understand and evaluate the potential physical impacts.

2. Ask producers about current climate trends and impacts: talking to producers directly, risks must be assessed.

3. Build longer-term and more stable relationships with suppliers: where markets are more stable, producers are empowered to invest for the future.

4. Support community development and environmental sustainability: climate resilient products, technologies, new forms of organizations and co-operations, managing social issues, new markets need to be supported.

5. Work through existing institutions, including governments.

Our other researches on modeling the implications (*Kovács et al.*, 2014) confirm this complex approach.

We are planning to get further information from the national disaster management system. This research will include the evaluation of extreme weather related cases such as snowstorm and flooding.

Acknowledgment–This paper presents the results of the projects TÁMOP-4.2.2/A-11/1-2012-0064.This project is supported by the European Union and co-financed by the European Social Fund.

References

Agrawala, S., Carraro, M., Kingsmill, N., Lanzi, E., Mullan, M., and *Prudent-Richard, G.* 2011: Private Sector Engagement in Adaptation to Climate Change: Approaches to Managing Climate Risks. *OECD Environment Working Papers 39,* http://dx.doi.org/10.1787/5kg221jkf1g7-en.

Caldwell, H., Quinn, H.K., Menuier, J., Subrier, J., and *Grenzeback, L.,* 2013: Potential Impacts of Climate Change on Freight Transport. http://climate.dot.gov/documents/workshop1002/caldwell.pdf.

Carey, J., 2011: Storm warnings: extreme weather is a product of climate change. Scientific American. http://www.scientificamerican.com/article/extreme-weather-caused-by-climate-change/

Czifra, T., Dobozi, E., Selmeczi, P., Kohán, Z., Rideg, A., and *Schneller, K.,* 2013: A területfejlesztés 4 éves szakmai programja a klímaváltozás hatásainak mérséklésére (2010–2013). http://www.vati.hu/files/sharedUploads/docs/ttei/A_teruletfejlesztes_klimaprogramja_2010-2013_1.pdf. In Hungarian)

Delbecq, A.L. and. *VandeVen, A.H.,* 1971: A Group Process Model for Problem Identification and Program Planning. *J. Appl. Behav. Sci. VII* (July/August, 1971), 466–491.

Delbecq, A.L., VandeVen, A.H., and *Gustafson, D.H.,* 1975: Group Techniques for Program Planners. Glenview, Illinois: Scott Foresman and Company.

Gáspár, L., 2003: Az élettartam mérnöki tudomány. *Közlekedéstudomány 53,* 81–129. (In Hungarian)

Gáspár, L., 2004: Az útburkolatok teljesítőképessége, *Közúti mélyépítési szemle 54 (11),* 7–12. (In Hungarian)

Hunyadi, D., 2010: A klímaváltozás hatása a közlekedési infrastruktúrára. *Közúti mélyépítési szemle 60 (3),* 35–40. (In Hungarian)

International Energy Agency, 2013: Redrawing the Energy Climate MapWorld Energy Outlook Special Report - released on 10 June 2013.

Jüttner, U., Peck, H. and *Christopher, M.,* 2003: Supply chain risk management: outlining an agenda for future research. *Int. J. Logistics: Res. Appl. 6,* 197–210.

Kovács Z., Pató Gáborné Szűcs B., and *Szabó L.,* 2014: Logisztika a klímaváltozás körülményei között. *Logisztikai Híradó. 2014/1,* 39–42. (In Hungarian)

Nordhaus, W.D., 2013: Why the Global Warming Skeptics Are Wrong? http://www.nybooks.com/articles/archives/2012/mar/22/why-global-warming-skeptics-are-wrong/?pagination=false.

Revesz, L.R. and *Shahabian, M.R.,* 2010: Climate Change and Future Generations. *Southern California Law Review 84,* 1099–1164.

Stott, P.A., Stone, D.A., and *Allen, M.R.,* 2004: Human contribution to the European heatwave of 2003. *Nature 432,* 610–614.

Thorpe, J. and *Fennel, S.,* 2012: Climate Change Risks and Supply Chain Responsibility: How should companies respond when extreme weather affects small-scale producers in their supply chain?" *Oxfam Discussion Papers, June 2012.*, www.oxfam.org.

Trenberth, K. E. 1999: Short-term Climate Variations. Recent accomplishments and issues for future progress. (Eds: *R. Pielke Sr* and *R. Pielke Jr*) Storms Vol 1. Routledge Press. London. 126–141.

United Nations Conference on Trade and Development (UNCTAD), 2011: Assuring Food Security in Developing Countries under the Challenges of Climate Change: Key Trade and Development Issues of a Fundamental Transformation of Agriculture. *Discussion Paper 2011(2).*

VandeVen, A.H. and *Delbecq, A.L.,* 1974: The effectiveness of nominal, Delphi, and interacting group decision making processes. *Acad. Manage J.* 605–621.

Vissy, K. and *Bátyi, F.,* 1998: A földfelszíni közlekedés meteorológiája. *Természet Világa, 129. I. különszám,* 75–78. (In Hungarian)

Yin, R. 1994: Case study research: design and methods. Thousand Oaks, CA, Sage.

Zaltman, G., Lemasters, K., and *Heffring, K.* 1982: Theory construction in marketing: some thoughts on thinking. New York, Wiley.

INSTRUCTIONS TO AUTHORS OF *IDŐJÁRÁS*

The purpose of the journal is to publish papers in any field of meteorology and atmosphere related scientific areas. These may be

- research papers on new results of scientific investigations,
- critical review articles summarizing the current state of art of a certain topic,
- short contributions dealing with a particular question.

Some issues contain "News" and "Book review", therefore, such contributions are also welcome. The papers must be in American English and should be checked by a native speaker if necessary.

Authors are requested to send their manuscripts to

Editor-in Chief of IDŐJÁRÁS
P.O. Box 38, H-1525 Budapest, Hungary
E-mail: journal.idojaras@met.hu

including all illustrations. MS Word format is preferred in electronic submission. Papers will then be reviewed normally by two independent referees, who remain unidentified for the author(s). The Editor-in-Chief will inform the author(s) whether or not the paper is acceptable for publication, and what modifications, if any, are necessary.

Please, follow the order given below when typing manuscripts.

Title page: should consist of the title, the name(s) of the author(s), their affiliation(s) including full postal and e-mail address(es). In case of more than one author, the corresponding author must be identified.

Abstract: should contain the purpose, the applied data and methods as well as the basic conclusion(s) of the paper.

Key-words: must be included (from 5 to 10) to help to classify the topic.

Text: has to be typed in single spacing on an A4 size paper using 14 pt Times New Roman font if possible. Use of S.I. units are expected, and the use of negative exponent is preferred to fractional sign. Mathematical formulae are expected to be as simple as possible and numbered in parentheses at the right margin.

All publications cited in the text should be presented in the *list of references*, arranged in alphabetical order. For an article: name(s) of author(s) in Italics, year, title of article, name of journal, volume, number (the latter two in Italics) and pages. E.g., *Nathan, K.K.,* 1986: A note on the relationship between photo-synthetically active radiation and cloud amount. *Időjárás 90,* 10-13. For a book: name(s) of author(s), year, title of the book (all in Italics except the year), publisher and place of publication. E.g., *Junge, C.E.,* 1963: *Air Chemistry and Radioactivity.* Academic Press, New York and London. Reference in the text should contain the name(s) of the author(s) in Italics and year of publication. E.g., in the case of one author: *Miller* (1989); in the case of two authors: *Gamov* and *Cleveland* (1973); and if there are more than two authors: *Smith et al.* (1990). If the name of the author cannot be fitted into the text: *(Miller,* 1989); etc. When referring papers published in the same year by the same author, letters a, b, c, etc. should follow the year of publication.

Tables should be marked by Arabic numbers and printed in separate sheets with their numbers and legends given below them. Avoid too lengthy or complicated tables, or tables duplicating results given in other form in the manuscript (e.g., graphs).

Figures should also be marked with Arabic numbers and printed in black and white or color (under special arrangement) in separate sheets with their numbers and captions given below them. JPG, TIF, GIF, BMP or PNG formats should be used for electronic artwork submission.

Reprints: authors receive 30 reprints free of charge. Additional reprints may be ordered at the authors' expense when sending back the proofs to the Editorial Office.

More information for authors is available: journal.idojaras@met.hu

Published by the Hungarian Meteorological Service

Budapest, Hungary

INDEX 26 361

HU ISSN 0324-6329